VIBROACOUSTIC BEHAVIOR AND NOISE CONTROL STUDIES OF ADVANCED COMPOSITE STRUCTURES

by

Deyu Li

BS, Wuhan University of Hydraulic and Electric Engineering, PR China, 1986

MS, Tsinghua University, PR China, 1992

Submitted to the Graduate Faculty of

the School of Engineering in partial fulfillment

of the requirements for the degree of

Doctor of Philosophy

University of Pittsburgh

2003

UNIVERSITY OF PITTSBURGH

SCHOOL OF ENGINEERING

This dissertation was presented

by

Deyu Li

It was defended on

July 16, 2003

and approved by

Dr. William W. Clark, Associate Professor, Department of Mechanical Engineering

Dr. Steven A. Lane, Senior Aerospace Research Engineer, Air Force Research Laboratory

Dr. Dipo Onipede Jr., Assistant Professor, Department of Mechanical Engineering

Dr. Marwan A. Simaan, Professor, Department of Electrical Engineering

Dr. Qing-Ming Wang, Assistant Professor, Department of Mechanical Engineering

Dissertation Director: Dr. Jeffrey S. Vipperman, Assistant Professor,
Department of Mechanical Engineering

ii

VIBROACOUSTIC BEHAVIOR AND NOISE CONTROL STUDIES OF
ADVANCED COMPOSITE STRUCTURES

Deyu Li, PhD

University of Pittsburgh, 2003

The research presented in this thesis is devoted to the problems of sound transmission and noise transmission control for advanced composite payload fairings. There are two advanced composite fairings under study. The first is a tapered, cylindrical advanced grid-stiffened composite fairing, and the second is a cylindrical ChamberCore composite fairing. A fully coupled mathematical model for characterizing noise transmission into a finite elastic cylindrical structure with application to the ChamberCore fairing is developed. It combines advantages of wave radiation principles and structural-acoustic modal interaction, and provides an ideal noise transmission model that can be extended to other finite cylindrical structures. Structural-acoustic dynamic parameters of the two fairings are obtained using a combination of numerical, analytical, and experimental approaches. An *in-situ* method for experimentally characterizing sound transmission into the fairings called noise reduction spectrum (NRS) is developed based on noise reduction. The regions of interest in the NRS curves are identified and verified during a passive control investigation, where various fill materials are added into wall-chambers of the ChamberCore fairing. Both Helmholtz resonators (HRs) and long T-shaped acoustic resonators (ARs) are also used to successfully control noise transmission into the ChamberCore fairing. In the process, an accurate model for the resonant frequency calculation and design of cylindrical HRs is derived. Further, a novel and more general model for the design of multi-modal, long, T-shaped ARs is developed, including three new end-correction equations that are validated experimentally.

The control results show that noise attenuation is significant in the controlled modes, and the control is also observed in some modes that are not targeted, due to acoustic modal coupling via the structure. Helmholtz resonators are found to produce between 2.0 and 7.7 dB increase in NRS in the targeted cavity modes while ARs produced 4.7 to 5.3 dB of control. Relative positioning between the matched resonators is heuristically optimized experimentally, and

demonstrates that spacing should be maximized for best performance. Once the feasibility and optimization of resonator control were established, six integral acoustic resonators are fabricated directly into the wall-chambers of the ChamberCore structure. Performance is found to be as well as for the non-integrated resonators.

ACKNOWLEDGMENTS

TABLE OF CONTENTS

LIST OF TABLES

LIST OF FIGURES

1.0 INTRODUCTION

At the end of the 20th century, remarkable progress had been made in design, analysis, and fabrication of advanced composite structures. Several novel composite structures, such as advanced grid-stiffened structures (AGS) [1-5] and chamber core structures (ChamberCore) [32, 33], have been designed, fabricated, and investigated for both civil and military applications. Both the AGS and ChamberCore structures offer higher strength and stiffness, less weight, and easier, cheaper fabrication than aluminum structures. These improvements in weight (61% decrease), strength (300% increase), and stiffness (1,000% increase along the hoop direction) [2] are accompanied by an increase of the sound transmission into the structures [6-12], which is governed by the geometry and physical structural acoustic properties. The fewer mechanical connections in the advanced composite structures relative to a metallic counterpart also lead to a decrease of structural damping, such that the structural vibration in the low frequency range could increase. The severe vibration and acoustic environment resulting during launch can seriously effect or even damage payloads. Thus, mitigating launch noise for composite structural vehicles is currently an important research topic. One alternative is to over-design the payload to withstand higher noise levels. The increased cost, however, offsets the weight savings afforded by the lightweight composite structures. The potential candidates for successful sound transmission control considered in this work are implementing active, passive or hybrid approaches and acoustic resonant absorbers.

1.1   Passive Noise and Vibration Control

The primary design of an expensive launch vehicle is based on the ability to satisfy the structural requirements. When an additional requirement of a specific level of structural-acoustic vibration is given, the simplest and most time effective treatment employed for the system is passive structural-acoustic vibration control approaches, which are used to significantly increase structural-acoustic vibration energy dissipation in order to meet the new sound transmission

requirements. Some passive control strategies have been investigated and proposed for the sound transmission improvement in rocket fairings. Griffin *et al*. [6], added the secondary structure in the payload fairing to create a characteristic impedance mismatch; Hughes and McNelis [8, 9] used free layer damping, and Crane and Santiago [12] used constrained layer damping to tune the system's dynamic response; Crane and Santiago [12] also changed the structure's geometric parameters to increase the acoustic impedance, and used double layer shell structure to achieve a reduction of the sound transmission between the inner surface and the outer surface.

Acoustic blankets were successfully used in the Titan IV payload fairing for the Cassini spacecraft [8-11]. Acoustic blankets are effective at high frequency, but are not practical for the low frequency range, because a much thicker and heavier blanket is required [8]. Actively imposing a characteristic impedance mismatch approach [6] is a good compensation for this limitation. The characteristic impedance mismatch is achieved by imposing a vacuum or near vacuum condition in the gap of a double partition container. Results from an experiment show at least a 19 dB sound pressure level (SPL) reduction of interior acoustics in the range from 0-200 Hz [6]. However, this approach is difficult to implement.

Crane and Santiago [12] investigated passive design methods through increasing the damping of composite cylindrical structures. The primary aim of their research was to develop cylindrical sections that were capable of dissipating vibration energy. They designed, analyzed and fabricated several monolithic composite cylinders with varying structural cross sections and internal damping treatments, and several variations of a double hollow-core configuration. They used modal testing to characterize the damping loss factors corresponding to acoustic transmission loss. Their research showed that the utilization of damping treatments in the form of a constrained layer significantly increases the damping loss factor of the cylinder, particularly in the low frequency range. The effect of the free damping layer configuration, however, was limited at the higher frequencies (above 2 kHz). The reduction of vibration amplitude from inner to outer skins of the double hollow core configuration was not significant.

1.2   Active Structure-Borne Noise Control

Now, more than ever before, vehicle manufacturers see increased demands for larger and heavier payloads as well as lower hardware costs. This requires using lighter, stronger, stiffer, and more spacious advance composite structures for the new generation launch vehicles. For a given size, weight, and strength, the passive sound transmission loss treatments in payload fairings are subject to fundamental physical limitations, especially in the low frequency range (below 200 Hz) where heavier passive materials or damping treatments are needed. Those treatments will significantly increase weight and reduce space, so active noise and structural-acoustic control approaches have been sought as alternatives [24-31].

In terms of noise control, there are active noise control (ANC) and active structural acoustic control (ASAC). The principle of ANC is based upon destructive interference of sound [18-22]. The basic idea is to create a copy of the disturbance, delay-invert it, and use it to cancel the original disturbance. The first prototype of an ANC system can be dated back to the early 20th century which was developed by a Germen inventor, Paul Lueg [23] in 1936, as shown in Figure 1.1. It is a classical example of active noise cancellation, and researchers use it to better understand the concept of active feedforward acoustic control. Here, an acoustic sensor, a microphone, is placed "up-stream" in a duct to detect the primary acoustic field at a point. A reference signal is captured and passed through a controller. The adjusted output signal from the controller is used to drive an actuator, a loudspeaker, to create the secondary acoustic field that is intended to result in destructive interference with the primary or noise source in the "down-stream" duct. Later, the first prototype of a feedback acoustic control system was proposed by Oslon and May in 1953 [13]. The ANC and analog electronic techniques, however, were not sufficient for implementing a real-world ANC product until significant steps were taken in the following aspects in the 1970's and 1980's. The first is progress in digital active acoustic control [14, 15], in which adaptive filters were used in ANC [16, 17]. The second breakthrough is the rapid development of cost-effective digital signal processing (DSP) chips.

The concept of ASAC can be explained as using force actuators, such as piezoelectric patches that are either surface-bonded or embedded in the host structure, to control and minimize the structural response which transmits more energy to reduce radiation efficiency. The principle of ASAC is systematically described and proposed in a book by Fuller *et al*. [18]. The

implementation of ASAC can eliminate the requirement for speakers, and save space and system weight. Most of the ASAC research has implemented adaptive feedforward control schemes [**68**].
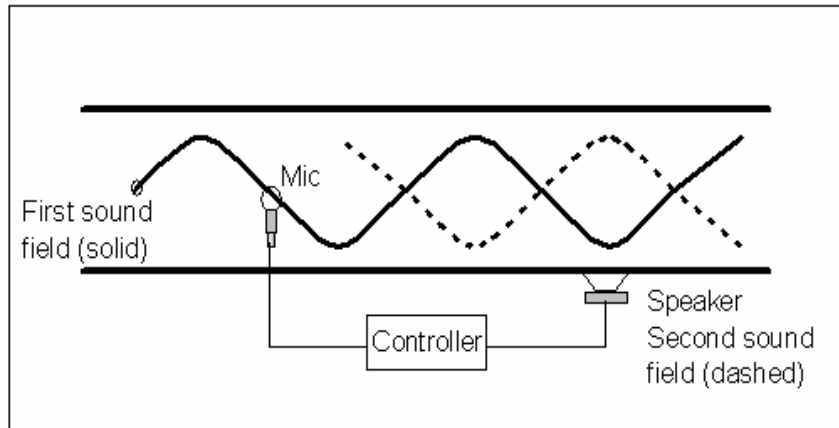
Figure 1.1 Schematic of Active Noise Control

Clark *et al*. [69], implemented the first adaptive structure for ASAC, in which structure-based sensing was used to eliminate the need for microphones to measure the pressure field. Feedback ASAC has also been studied [71-73], but requires an accurate model of the plant being controlled, including the coupling between the structural and acoustic modes. The structural modes responsible for the highest acoustic radiation are often weighted more heavily in the performance metric in order to achieve better acoustic control [70, 71]. This effect can also be achieved by frequency-weighting the performance cost-functions through H_2 and H_∞ control synthesis techniques [72]. The adaptive structure and optimal control strategies were used to implement a feedback ASAC system by Vipperman [73].

1.3   Scope of Contribution

Two different composite structures supplied by the Air Force Research Laboratory, Space Vehicles Directorate (AFRL/VS) are being investigated in this study. One is a mock-scale AGS tapered cylindrical fairing, and the other is a mock-scale ChamberCore right cylindrical fairing. The AGS composite structure has been used in launch vehicles. Its mechanical properties, design methods, and fabrication methods can be found in references [1-5]. There are a couple of vibroacoustic studies about the AGS composite structure. General studies on improving the sound transmission loss into fairings have been conducted for Minotaur-size launch vehicles, where passive [6] and feedback active structural-acoustic controls [24, 26] were numerically evaluated. Two earlier experimental studies focused on specific types of noise control for the AGS mock-scale prototype, including evaluating the effectiveness of hybrid structural-acoustic control inputs as well as positive position feedback (PPF) controllers [25], which do not require overly-complicated system models. Initial studies about the ChamberCore composite structures have focused primarily on structural static strength and stability analysis, damage mechanisms, optimal design and fabrication methods, and rudimentary dynamic behavior [32, 33].

The scope of contribution of this study is listed as follows:

1.   A fully coupled mathematical model of noise reduction spectrum for a finite uniform thin cylindrical shell is developed. The formulas for calculating effective thickness and effective density of the ChamberCore fairing are derived based upon a box-beam model. The sound transmission behavior of the ChamberCore cylindrical fairing is analytically investigated.

2.   The vibroacoustic behavior of the AGS tapered composite fairing and the ChamberCore composite fairing is numerically/analytically studied. A new modal parameter extraction method based on state-space realization is developed, and the structural and acoustic modal parameters are also experimentally identified.

3.   An *in-situ* method to experimentally characterize sound transmission into a cylindrical structure is developed. Thorough characterization of the sound transmission behavior of the two fairings is experimentally finished.

4.   The passive control with passive fills for the ChamberCore cylindrical fairing is experimentally investigated.

5. An accurate and general cylindrical Helmholtz resonator model for resonant frequency calculation and resonator design is developed. The effects on the noise attenuation of two closely spaced resonators are experimentally studied, and the optimal positions of the Helmholtz resonators are also discussed. The feasibility of the noise transmission control using Helmholtz resonators is investigated by using cylindrical Helmholtz resonators.

6. A novel and general model for the calculation of resonant frequencies of the long T-shaped acoustic resonators is developed. A new equation for the design of long T-shaped acoustic resonators is derived. Three new end correction models based upon the consideration of acoustics are proposed and experimentally validated. Twelve long T-shaped acoustic resonators, including six resonators designed with the wall-chambers of the ChamberCore structure, are constructed and used to control noise transmission into the ChamberCore fairing. The noise transmission control using long T-shaped acoustic resonators and long chamber-based, T-shaped acoustic resonators are conducted.

The author will begin with an overview of passive structural acoustic vibration control, active structure-borne noise control, and the scope of the contribution. In Chapter 2, the noise transmission through a flat panel is presented. Chapter 3 covers the noise transmission into a finite elastic cylinder, including a mathematical noise reduction spectrum model and numerical investigation for the ChamberCore cylindrical fairing. Chapter 4 contains the numerical, analytical and experimental part necessary to understand the vibroacoustic properties and characterize the noise transmission behavior for the two advanced composite fairings. A new mode shape extraction method is developed here, and an *in-situ* method for experimentally characterizing noise reduction spectrum is also presented in this chapter. Chapter 5 introduces the noise transmission control for ChamberCore cylindrical fairing through using passive materials. Chapter 6 is the noise transmission control for the ChamberCore cylindrical fairing by using acoustic resonators, including several new models and new design equations and noise transmission controls. Concluding remarks along with scaling all new models and algorithms for the full size payload fairings, and with recommendations for future work follow in Chapter 7.

2.0 SOUND TRANSMISSION LOSS THROUGH FLAT PANELS

Sound waves are reflected and transmitted through the interaction of medium interfaces. A commonly used quantity in transmission problems is the transmission loss. It is the decibel expression of the sound power transmission coefficient, which is defined as the ratio of the transmitted power to the incident power. The definition of transmission loss is based on the sound power transmission through an infinite flat panel in fluid medium, where the transmitted sound is assumed to be totally absorbed, so that only inward-propagating waves exist. In this chapter, the sound transmission and sound transmission loss through an infinite flat panel is studied, which provides an insight into the sound transmission behavior in the mass, stiffness, and mechanical damping controlled zones, and is viewed as the first step toward understanding the basic physical parameters governing the sound transmission into cylindrical structures.

Although sound radiation is the result of a vibrating flat panel disturbing its surrounding medium, the vibration behavior of a flat panel *in-vacuo* and the sound radiation from a vibrating panel are first investigated individually. Then, the coupled vibration of the flat panel with the fluid medium is discussed. Before defining the sound transmission loss, several important physical quantities (mechanical impedance, radiation impedance, and critical frequency) will be introduced.

2.1   Mechanical Impedance of an *in-vacuo* Infinite Flat Panel

Consider a plate with thickness h and infinite length and width. The density, modulus, and Poisson's ratio are r_p, E, and m, respectively. Then, the bending modulus, the speed of sound propagating in the plate material, and the surface density of the plate are $B = Eh^3/12(1-m^2)$, $c_p = \sqrt{E/r_p(1-m^2)}$, and $m_s = r_p h$, respectively. Assume the plate is located in the x, y plane

(at $z = 0$) as shown in Figure 2.1. The 2-D equation of motion (EOM) of the *in-vacuo* plate is [45, 46]:
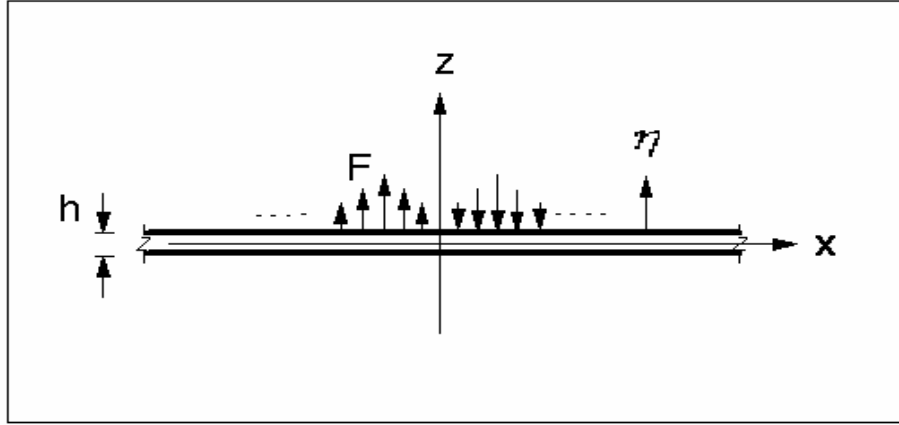
Figure 2.1 Infinite Flat Panel *in-vacuo*

$$B\left(\frac{\partial^4 \boldsymbol{h}}{\partial x^4} + 2\frac{\partial^4 \boldsymbol{h}}{\partial x^2 \partial y^2} + \frac{\partial^4 \boldsymbol{h}}{\partial y^4}\right) + m_s \frac{\partial^2 \boldsymbol{h}}{\partial t^2} = F(x, y, t) , \qquad (2.1)$$

where B is the bending modulus, $\boldsymbol{h}(x, y, t)$ is the displacement in z-direction, m_s is the surface density, and $F(x, y, t)$ is the force per unit area. If the force distribution does not change with y, and only the solutions in the x direction are considered, Eq. (2.1) is simplified into a 1-D equation of motion:

$$B\frac{\partial^4 \boldsymbol{h}}{\partial x^4} + m_s \frac{\partial^2 \boldsymbol{h}}{\partial t^2} = F(x, t) . \qquad (2.2)$$

Assume there are harmonic solutions in both time and space domain. The displacement can be described as

$$\boldsymbol{h}(k_x, \boldsymbol{w}) = Ae^{j(wt - k_x x)} , \qquad (2.3)$$

8

where A is the amplitude of displacement, $\boldsymbol{w}$ and k_x are the frequency and wavenumber of the forcing function, respectively, and $k_x = \boldsymbol{w}/c$. In the frequency and wavenumber domain, using Eq. (2.3), Eq. (2.2) can be represented as

$$(Bk_x^4 - \boldsymbol{w}^2 m_s)\boldsymbol{h}(k_x, \boldsymbol{w}) = F(k_x, \boldsymbol{w}).\tag{2.4}$$

Note that $\dot{\boldsymbol{h}}(k_x, \boldsymbol{w}) = j\boldsymbol{w}\boldsymbol{h}(k_x, \boldsymbol{w})$. Eq. (2.4) can be rewritten as

$$jm_s\boldsymbol{w}\left(1 - \frac{Bk_x^4}{m_s\boldsymbol{w}^2}\right)\dot{\boldsymbol{h}}(k_x, \boldsymbol{w}) = F(k_x, \boldsymbol{w}).\tag{2.5}$$

The representation in terms of impedance is

$$Z_B\dot{\boldsymbol{h}}(k_x, \boldsymbol{w}) = F(k_x, \boldsymbol{w}),\tag{2.6}$$

where Z_B is called the mechanical impedance or *in-vacuo* bending impedance of the plate, and represented by:

$$Z_B = jm_s\boldsymbol{w}\left(1 - \frac{Bk_x^4}{m_s\boldsymbol{w}^2}\right).\tag{2.7}$$

We defined "free" bending wavenumber of the plate as

$$k_B = \left(\frac{m_s\boldsymbol{w}^2}{B}\right)^{\frac{1}{4}}.\tag{2.8}$$

Then, Eq. (2.7) can be rewritten as

$$Z_B = jm_s\boldsymbol{w}\left[1 - \left(\frac{k_x}{k_B}\right)^4\right].\tag{2.9}$$

When considering the material damping of the plate, the bending modulus can be expressed as:

$$B^* = B(1 - jd),$$ (2.10)

where $(d \leq 1)$ is the damping term. Substituting Eq. (2.10) into Eq. (2.7), the mechanical impedance becomes

$$Z_B^* = jm_s w \left[1 - \left(\frac{k_x}{k_B} \right)^4 \right] - d m_s w \left(\frac{k_x}{k_B} \right)^4.$$ (2.11)

The equation of motion with damping has the same form as Eq. (2.6) without damping, but the mechanical impedance Z_B is replaced by Z_B^* as:

$$Z_B^* h(k_x, w) = F(k_x, w).$$ (2.12)

Discussion:

(1)   When $k_x = k_B$:

The forcing function wavenumber, k_x, equals the free bending wavenumber, k_B. From Eqs. (2.11) and (2.12) it is known that the mechanical impedance (Z_B^*) has a minima, and the velocity $h(k_x, w) = F(k_x, w)/Z_B^*$ has a maxim. A spatial resonance occurs. It is called the coincidence phenomenon. If there is no damping, i.e. $d = 0$, the amplitude of the vibration velocity becomes infinity. Therefore, the vicinity of the free bending wavenumber (k_B) is also called the damping-controlled zone.

(2)   When $k_x < k_B$:

Eq. (2.12) can be simplified to:

$$F(k_x, w) \approx m_s h(k_x, w).$$ (2.13)

In this case the system looks like a mass, and thus it is referred to as the mass- controlled region.

(3)   When $k_x > k_B$:

Eq. (2.12) can be approximated as:

$$F(k_x, \boldsymbol{w}) \approx -m_s \boldsymbol{w}^2 \left(\frac{k_x}{k_B} \right)^4 (1 + j\boldsymbol{d})\boldsymbol{h}(k_x, \boldsymbol{w}) .$$

(2.14)

In this case the variation of the stiffness term $(k_x/k_B)^4$ will dominate the mechanical

impedance, and it is referred to as the stiffness-controlled region.

2.2 Sound Radiation from a Vibrating Infinite Flat Panel

Assume the plate as shown in Figure 2.2 is freely vibrating with a one-dimensional harmonic velocity:

$$\boldsymbol{h} = V_0 e^{j(\boldsymbol{w}t - k_B x)} .$$

(2.15)

If the losses are ignored, the radiated pressure field and normal particle velocity induced by the vibrating plate can be described as:

$$p = P_0 e^{j(\boldsymbol{w}t - k_x x - k_z z)} ,$$

(2.16)

$$u_z = U_0 e^{j(\boldsymbol{w}t - k_x x - k_z z)} ,$$

(2.17)

where k_x is called the trace wavenumber, which is the longitudinal component of the wavenumber. Note that the sound source is the vibration of the panel, so $k_x = k_B$. The radiated sound wavenumber is $k = \boldsymbol{w}/c$, therefore, the normal component of the radiated sound wave number (k_z) and the radiation angle ($\boldsymbol{q}$) can be computed from:
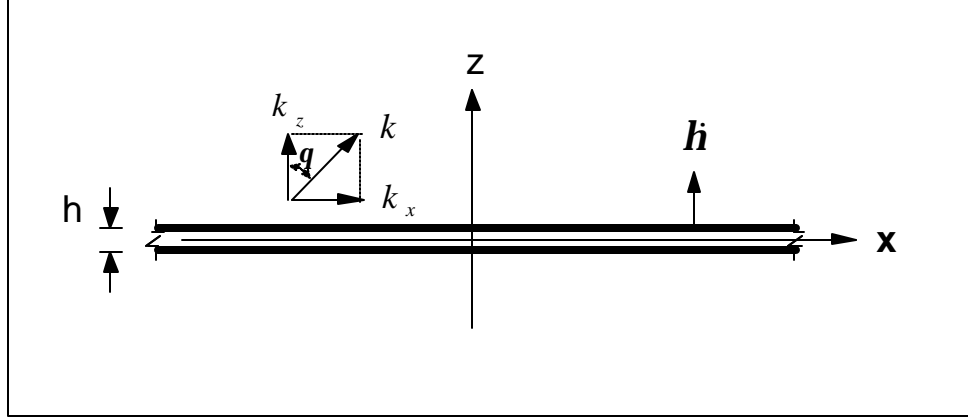
Figure 2.2 Vibrating Infinite Flat Panel in Fluid

$$k_z = \pm\sqrt{k^2 - k_B^2} \, , \qquad\qquad (2.18)$$

$$\boldsymbol{q} = \sin^{-1}\left(\frac{k_B}{k}\right), \qquad\qquad (2.19)$$

From the boundary condition $u_z \mid_{z=0} = \hbar$, U_0 can be solved as

$$U_0 = V_0. \qquad\qquad (2.20)$$

So, the normal particle velocity (see Eq. (2.17)) can be rewritten as:

$$u_z = V_0 e^{j(\boldsymbol{w}t - k_x x - k_z z)}. \qquad\qquad (2.21)$$

Substituting Eqs. (2.16) and (2.21) into the momentum equation [46]

$$\frac{\partial p}{\partial z} = -\boldsymbol{r}\frac{\partial u_z}{\partial t}. \qquad\qquad (2.22)$$

The amplitude of pressure can be solved as:

$$P_0 = \frac{rw}{k_z} V_0 . \tag{2.23}$$

Generally, radiated impedance of a vibrating surface is used as a measure of the reaction of the acoustic medium against the surface motion. It is defined as:

$$Z_r = \left(\frac{p}{u_z} \right)_{z=0} . \tag{2.24}$$

Using Eqs. (2.16), (2.21), and (2.23), the radiated impedance can be computed from

$$Z_r = \frac{P_0}{V_0} = \frac{rw}{k_z} = \frac{rc}{\cos q} , \tag{2.25}$$

where rc is called the characteristic impedance of the fluid medium. The radiation pressure from a vibrating infinite flat panel is expressed in terms of radiation impedance as:

$$p = Z_r u_z . \tag{2.26}$$

Another quantity known as the radiation efficiency is also typically used to describe the acoustic radiation. Physically, the radiation efficiency is the ratio of the sound power radiated by the particular sound source of surface area S, to the power which would be carried in one direction by a plane wave of area S [20].

Discussion:

(1)   When $k_B > k$:

In this case, $k_z = -\sqrt{k^2 - k_B^2}$ is purely an imaginary [46]. The normal radiation pressure $p_z = P_0 e^{-jk_z z}$ will rapidly die out as z increases. This wave is called an evanescent wave.

(2)   When $k_B = k$:

In this case, $k_z = 0$, $l_z \to \infty$, and $q = p / 2$. The wavelength of radiation is theoretically infinite, and the radiation is parallel to the panel.

(3)   When $k_B \to 0$:

In this case, $l_B \to \infty$, and $q = 0$. The panel vibrates like a rigid panel, and the radiation is normal to the plate surface.

(4)   When $k_B < k$:

The radiation angle is $q \in (0, p/2)$. This is the most general case.

2.3   Sound Transmission through an Infinite Flat Panel

Incident sound waves on a plate force it to vibrate and radiate sound from both sides as shown in Figure 2.3, where p_i, p_r, and p_t are the incident wave, reflected wave and transmitted wave, respectively. q_1 and q_2 are the incident angle and transmitted angle, respectively. c_1, r_1 and c_2, r_2 are the speed of sound and density of fluid medium. The subscript 1 and 2 stand for two fluid mediums.
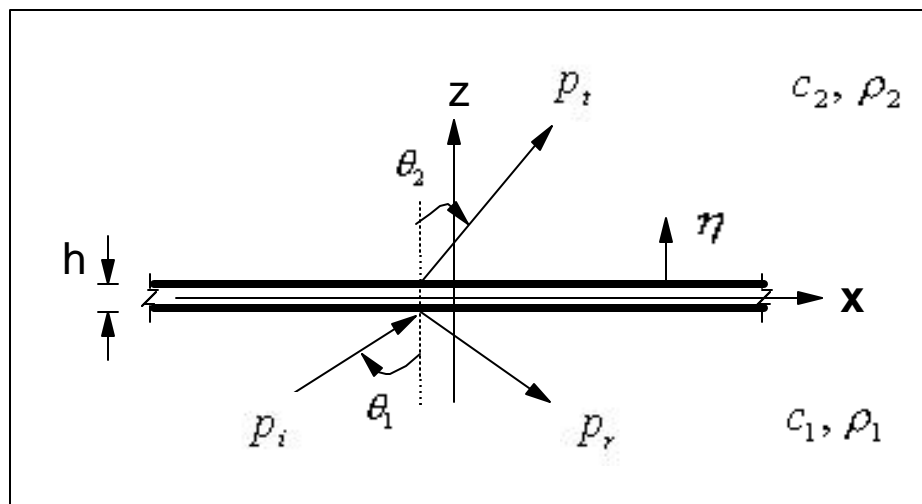
Figure 2.3 Infinite Flat Panel in Fluid Medium

Assume the incident sound wave is plane wave, and ignore losses. The pressure field can be described as [46]:

$$p_i = P_i e^{j(wt - k_{1x}x - k_{1z}z)},$$ (2.27)

$$p_r = P_r e^{j(wt - k_{1x}x + k_{1z}z)},$$ (2.28)

$$p_t = P_t e^{j(wt - k_{2x}x - k_{2z}z)},$$ (2.29)

where k_{1x}, k_{1z} are the trace wavenumbers and normal components of wavenumbers in medium 1, respectively, and k_{2x}, k_{2z} are the trace wavenumbers and normal components of wavenumbers in medium 2, respectively, and $k_{2x} = k_{1x} = k_x$. The resultant pressure in medium 1 and medium 2 respectively is p_1 and p_2.

$$p_1 = p_i + p_r,$$ (2.30)

$$p_2 = p_t.$$ (2.31)

Substituting Eq.(2.30) and (2.31) into Eq. (2.22), the normal particle velocity at $z = 0$ can be solved as:

$$u_z^+ |_{z=0} = \frac{k_{1z}}{wr_1}(P_i - P_r)e^{j(wt - k_x x)},$$ (2.32)

$$u_z^- |_{z=0} = \frac{k_{2z}}{wr_2} P_t e^{j(wt - k_x x)},$$ (2.33)

where u_z^+ is the normal particle velocity on the side ($z > 0$), and u_z^- is the normal particle velocity on the side ($z < 0$). Assume the vibration velocity of the plate is

$$\dot{h} = V_0 e^{j(wt - k_x x)},$$ (2.34)

where V_0 is the velocity amplitude of the plate, and will be determined by the boundary conditions

15

$$\boldsymbol{h} = u_z^+ \mid_{z=0}, \tag{2.35}$$

and

$$\boldsymbol{h} = u_z^- \mid_{z=0}. \tag{2.36}$$

Substituting Eqs. (2.32) and (2.34) into Eq. (2.35), one obtains

$$V_0 = \frac{P_i - P_r}{Z_1}, \tag{2.37}$$

where Z_1 is the radiation impedance in medium 1, and is computed from

$$Z_1 = \frac{\boldsymbol{r}_1 \boldsymbol{w}}{k_{1z}} = \frac{\boldsymbol{r}_1 c_1}{\cos \boldsymbol{q}_1}. \tag{2.38}$$

Substituting Eqs. (2.33) and (2.34) into Eq.(2.36), obtains

$$V_0 = \frac{P_t}{Z_2}, \tag{2.39}$$

where Z_2 is the radiation impedance in medium 2, and is computed from

$$Z_2 = \frac{\boldsymbol{r}_2 \boldsymbol{w}}{k_{2z}} = \frac{\boldsymbol{r}_2 c_2}{\cos \boldsymbol{q}_2}. \tag{2.40}$$

From Eqs. (2.37) and (2.39), the amplitude of the reflected and transmitted pressure can be respectively solved as

$$P_r = P_i + V_0 Z_1, \tag{2.41}$$

$$P_t = V_0 Z_2. \tag{2.42}$$

Using Eq. (2.12), the equation of motion of the plate is:

$$Z_B^* \boldsymbol{h} = \left[p_t - (p_i + p_r) \right] \big|_{z=0}. \tag{2.43}$$

where $\boldsymbol{h}$ is the vibration velocity of the plate, and given by Eq.(2.34). Substituting Eqs. (2.27), (2.28), (2.29) and (2.34) into Eq. (2.43), yields

$$Z_B^* V_0 = P_t - (P_i + P_r). \tag{2.44}$$

Substituting Eqs. (2.41) and (2.42) into Eq.(2.44), V_0 can be solved as:

$$V_0 = \frac{2P_i}{Z_B^* + Z_1 + Z_2}. \tag{2.45}$$

Substituting Eq. (2.45) into Eqs. (2.41) and (2.42), the amplitude of reflected and transmitted pressures are solved as

$$P_r = \frac{Z_B^* - Z_1 + Z_2}{Z_B^* + Z_1 + Z_2} P_i, \tag{2.46}$$

$$P_t = \frac{2Z_2}{Z_B^* + Z_1 + Z_2} P_i. \tag{2.47}$$

Substituting Eqs. (2.46) and (2.47) into Eq. (2.44), yields

$$-\frac{1}{2}(Z_B^* + Z_1 + Z_2)V_0 = P_i. \tag{2.48}$$

Setting

$$Z = -\frac{1}{2}(Z_B^* + Z_1 + Z_2), \tag{2.49}$$

where Z is the coupled impedance of the structural and acoustic systems. Eq. (2.48) can be simplified as

$$ZV_0 = P_i, \tag{2.50}$$

or

$$Z\dot{h}\big|_{z=0} = p_i\big|_{z=0}. \tag{2.51}$$

Note that Eq. (2.51) describes the motion of an infinite flat panel in fluid medium and under the action of oblique incident pressure p_i, reflected pressure p_r, and transmitted pressure p_t. This equation has the same form as Eq. (2.12) which describes the motion of a forced *in-vacuo* panel. Therefore, they should share some properties, such as the mass-, stiffness-, and damping-

controlled zones, and the coincidence phenomenon. Substituting Eqs. (2.11), (2.38), and (2.40) into Eq. (2.49), the result is

$$Z = -\frac{1}{2}\left\{ jm_s\mathbf{w}\left[1-\left(\frac{k_x}{k_B}\right)^4\right] - \mathbf{d}m_s\mathbf{w}\left(\frac{k_x}{k_B}\right)^4 + \frac{\mathbf{r}_1c_1}{\cos\mathbf{q}_1} + \frac{\mathbf{r}_2c_2}{\cos\mathbf{q}_2}\right\}.$$ (2.52)

When the fluid medium is the same on both sides of the panel, the impedance can be simplified to:

$$Z = -\frac{1}{2}\left\{ jm_s\mathbf{w}\left[1-\left(\frac{k_x}{k_B}\right)^4\right] - \mathbf{d}m_s\mathbf{w}\left(\frac{k_x}{k_B}\right)^4 + \frac{2\mathbf{r}c}{\cos\mathbf{q}}\right\}.$$ (2.53)

Based on Eq. (2.47), the pressure transmission coefficient (T) is defined as the ratio of the magnitude of the transmitted pressure to the magnitude of the incident pressure ($0 \leq T \leq 1$):

$$T = \left|\frac{P_t}{P_i}\right| = \left|\frac{Z_2}{Z}\right|.$$ (2.54)

The sound power transmission coefficient is defined as the ratio of transmitted power to the incident power, and can be computed from [46]:

$$\mathbf{t} = |T|^2 \frac{Z_1}{Z_2}.$$ (2.55)

If the fluid medium is the same on both sides of the panel, the sound power transmission coefficient is simplified to

$$\mathbf{t} = |T|^2 = \left|\frac{Z_2}{Z}\right|^2.$$ (2.56)

Substituting Eqs. (2.40) and (2.53) into Eq. (2.56), the sound power transmission coefficient can be expressed as:

18

$$t = \frac{|\,2\boldsymbol{r}c\sec\boldsymbol{q}\,|^2}{|\,jm_s\boldsymbol{w}[1-(k_x/k_B)^4]-[m_s\boldsymbol{w}\boldsymbol{d}(k_x/k_B)^4 + 2\boldsymbol{r}c\sec\boldsymbol{q}]\,|^2}\,. \tag{2.57}$$

The transmission loss is defined as:

$$TL = -10\log_{10}(t) \quad \text{(dB)}. \tag{2.58}$$

"Critical frequency" plays an important role in characterizing sound transmission through a flat panel, which is defined as the smallest coincidence frequency. The critical frequency is also defined as the frequency at which the speed of plate-bending wave equals the speed of sound in the fluid medium. It can be found by:

$$\boldsymbol{w}_c = c^2\sqrt{\frac{m_s}{B}}\,, \tag{2.59}$$

where c is the speed of sound, m_s is the surface density of the flat panel, and B is the bending modulus and is computed from $B = Eh^3/12(1-\boldsymbol{m}^2)$.

Discussion:

(1)   When $\boldsymbol{w} < \boldsymbol{w}_c$:

The relationship between wavenumbers can be described as:

$$\frac{k_x}{k_B} = \frac{k\sin\boldsymbol{q}}{k_B} = \left(\frac{\boldsymbol{w}}{\boldsymbol{w}_c}\right)^{\frac{1}{2}}\sin\boldsymbol{q} = \left(\frac{\boldsymbol{w}}{\boldsymbol{w}_{co}}\right)^{\frac{1}{2}}. \tag{2.60}$$

Therefore, $k_x < k_B$. In this circumstance, the stiffness and damping terms are much less than the mass term. In the extreme case, i.e. $k_x \to 0$, the wavelength grows to infinity, i.e. $\boldsymbol{l}_x \to \infty$, and the vibration of panel is much like a rigid plate. The dominant property is the mass.

For easy analysis, t is re-written as:

$$t = \frac{(2\rho c / m_s w)^2 \sec^2 q}{[1 - (k_x / k_B)^4]^2 + [d(k_x / k_B)^4 + (2\rho c / m_s w)\sec q]^2} \,. \tag{2.61}$$

Because $k_x < k_B$, the terms $(k_x / k_B)^4$ and $d(k_x / k_B)^4 << 1$. Note $d \leq 1$, such that t may be approximated as follows:

$$t = \frac{1}{1 + (m_s w \cos q / 2\rho c)^2} \,. \tag{2.62}$$

The transmission loss is therefore approximately

$$TL \approx 10 \log 10 \left[1 + \left(\frac{m_s w \cos q}{2\rho c} \right)^2 \right]. \tag{2.63}$$

For "high frequencies" (i.e. $m_s w \cos q / 2\rho c >> 1$) the corresponding sound transmission loss is approximated by:

$$TL \approx 20 \log 10 \left(\frac{m_s w \cos q}{2\rho c} \right), \qquad (w = w_c). \tag{2.64}$$

This represents the mass law behavior of sound barriers for oblique incidence sound wave.

(2)   When $w = w_c$, i.e. $k_x = k_B$, and $q = p / 2$, coincidence occurs.

In this case, a maximum occurs for the transmission coefficient, and an undesirable dip occurs in the transmission loss curve. Eq. (2.57) can be simplified as:

$$t = \frac{1}{1 + d(m_s w \cos q / 2\rho c)^2} \,. \tag{2.65}$$

If $d > 2\rho c / m_s w_c \cos q$, sound transmission loss in the vicinity of coincidence is controlled by mechanical damping.

(3)   When $w > w_c$, i.e. $k_x > k_B$:

Ignoring damping effects (i.e. $d = 0$), Eq. (2.57) may be approximated as:

$$t \approx \frac{1}{1+(Bk_x^4 \cos q / 2rcw)^2}, \qquad (w \ ? \ w_c).$$

(2.66)

In this case, the transmission loss curve rebounds from the minima in the coincidence frequency, the mass-law and mechanical damping control zones are exceeded, and the panel motion becomes stiffness-controlled.

3.0 SOUND TRANSMISSION INTO A FINITE CYLINDRICAL STRUCTURE

The physics of the problems under studying are as follows: (1) the incident sound wave impinging upon the surface of the cylindrical structure causes vibration of the cylindrical shell, (2) the shell vibration induces sound pressure fluctuations including scattering, radiation and transmission pressures, (3) the transmitted pressures excite the acoustic cavity inside the cylinder, and (4) the noise of the interior cavity interacts with the structure to affect the cylindrical structural vibration and create the coupled vibration. The sound transmission through infinite, homogeneous, isotropic thin cylindrical shells has been investigated in some detail by several researchers [36-38]. The problems of sound transmission through an infinite cylindrical sandwich shell with honeycomb core were studied by Tang *et al*., [42, 43]. The simplified analysis of sound transmission through a finite, closed cylindrical shell was first proposed by White [38]. The sound radiation into the acoustic cavity enclosed by a finite plated-ended cylindrical shell was studied by Cheng [39]. Tso and Hansen derived a coupling loss factor for a cylindrical/plate structure using static energy analysis (SEA) [40]. However, their method could not show the effects on sound transmission of the cavity resonances. Koval first presented a mathematical noise reduction model to count for the effects of cavity resonances on sound transmission into a thin cylindrical shell [41]. In his model, the longitudinal modes of the cylindrical cavity are neglected, because both infinite cylindrical shell and infinite acoustic cavity are considered. The newest experimental results for the noise transmission behavior into finite elastic cylindrical structures show that not only are the circumferential modes and the radial modes of the cavity important, but the longitudinal modes of the cavity also have significant effects on the sound transmission into the cylinders (see Section 4.4.3). Therefore, in this chapter a new model is proposed to analytically investigate the noise transmission for a finite elastic cylindrical structure.

This chapter is a theoretical study of the sound transmission into a finite ChamberCore cylinder, which is based on the research of sound transmission into a uniform, thin cylindrical shell immersed in a fluid medium. Particular attention of this study is focused on evaluating a

"noise reduction spectrum" for the closed finite ChamberCore cylinder which is an extension of the noise reduction (NR) proposed by L. R. Koval [41].

This Chapter is arranged as the following. In Section 3.1 the ChamberCore sandwich-type structure is modeled to a uniform cylindrical shell. In Section 3.2 several important frequencies that are generally used to characterize sound transmission into cylindrical structures are introduced. In Section 3.3 the exterior sound field for an infinite cylindrical structure is derived using sound propagation and radiation principles. In Section 3.4 the internal sound field are solved using structural and acoustic modal interaction method. In Section 3.5 the noise reduction spectrum (NRS) is defined and a mathematical model for the calculation of NRS is derived. In Section 3.6 the ChamberCore cylindrical fairing is analytically investigated using the mathematical model. Some conclusions are given in Section 3.7.

3.1   Beam-Box Model of the ChamberCore Composite Cylindrical Structure

The ChamberCore composite cylindrical structure is a sandwich-type structure. In order to simplify analysis of sound transmission into the cylinder, the sandwich cylindrical shell is modeled as an isotropic uniform cylindrical shell. The uniform shell can be obtained based on the thin-wall box-beam model, which was used by George *et al.* [33] for optimizing the wall thickness of the ChamberCore composite cylindrical structure. The effective thickness and effective density of the uniform shell are used instead of the practical ones. The geometric dimensions including effective thickness, h_{eff}, are defined in Figure 3.1.

It is assumed that the outer and inner skins have the same thickness, t_1, the two sidewalls of each chamber have the same thickness, t_2. If the thickness of the two skins is much less than the distance between their surface, $t_1 << d$, the bending stiffness of the box-beam can be approximated as [74]:

$$EI_{yy} \approx 2A_1 b \left(\frac{d}{2} \right)^2 + A_2 d \frac{d^2}{6},$$ (3.1)

where $b=(w_1+w_2)/2$ is the average widths of the wedge-box-beam, and w_1 and w_2 are the width of the top and bottom sides of the wedge-box-beam (see Figure 3.1-B), respectively. E is Young's modulus, I_{yy} is the moment of inertia around y-axis. The two coefficients A_1 and A_2 are calculated by following equations:

$$A_1 = \frac{Et_1}{1-m^2},$$

(3.2)

$$A_2 = \frac{Et_2}{1-m^2},$$

(3.3)

where m is Poisson's ratio.
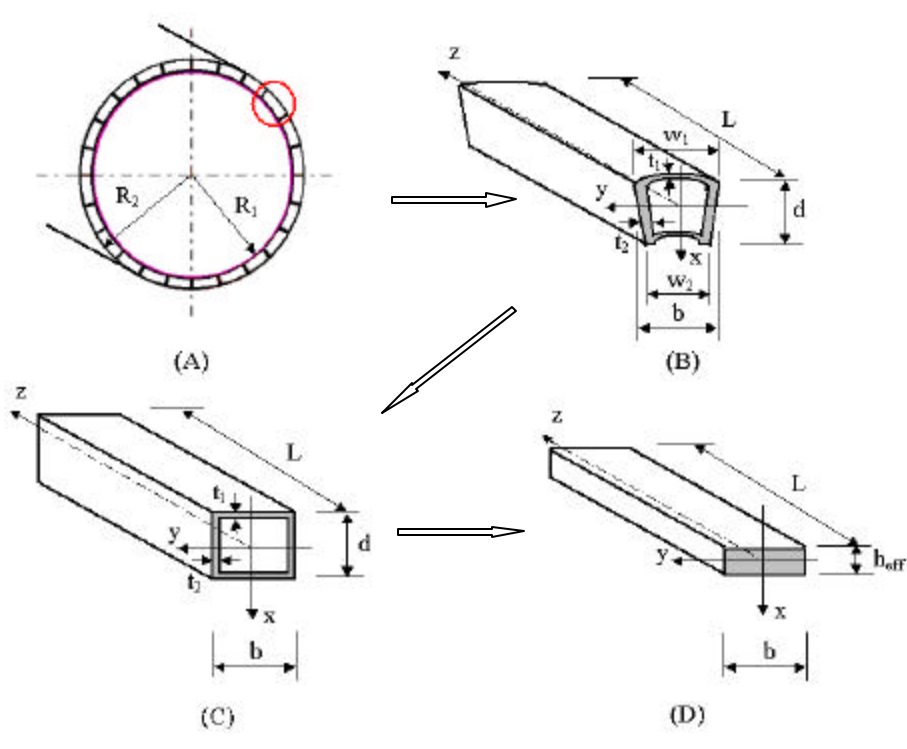
Figure 3.1 Box-Beam Geometry

where figure (A) is the geometry of the ChamberCore structure, figure (B) is one chamber of the cylinder, figure (C) is the box-beam simplification, and figure (D) is the plain beam approximation.

24

The effective thickness, h_{eff}, is calculated when the bending stiffness of the uniform beam ($EI_{yyuniform} = Ebh_{eff}^3 / 12$) is the same as that of the box-beam given by Eq. (3.1).

$$h_{eff} \approx d \sqrt[3]{\frac{1}{1-m^2}\left(\frac{6t_1}{d}+\frac{2t_2}{b}\right)}.$$

(3.4)

The effective density, r_{eff}, can be obtained by equivalent mass per unit length of the uniform beam and the box-beam:

$$r_{eff} = \frac{2(t_1 b + t_2 d - 2t_1 t_2)r_{shell} + (w_1 + w_2 - 4t_2)(d - 2t_1)r_{fill}/2}{bh_{eff}},$$

(3.5)

where r_{shell} and r_{fill} are respectively the density of the cylindrical shell and any fill media in the chambers. Fills can be added to the wall chambers for passive control studies. The material properties and geometric parameters are shown in Table 3.1. The effective thickness and effective density are also shown in the last column of Table 3.1.

Table 3.1 Physical and Geormitric Parameters of the ChamberCore Cylindrical Fairing

Material parameter	Geometric parameter (mm)	Effective parameter
$E_{average}$ = 60 Gpa $m_{average}$ = 0.3 ρ_{shell} = 1494 kg/m^3 ρ_{air} = 1.21 kg/m^3 c = 346 m/s	R_1 = 255 R_2 = 275 L = 775 b = 69.3 d = 25.8 t_1 = 1.7 t_2 = 1.3	h_{eff} = 20.1 mm ρ_{eff} = 315 kg/m^3

3.2   Ring Frequency, Critical Frequency and Cutoff Frequency

Before studying noise transmission into the cylindrical shell, let's quickly introduce several important frequencies, i.e. ring frequency, cutoff frequency, and critical frequency first,

which are always of interest to describe the sound transmission behavior of a cylindrical shell [44].

Ring frequency is used to characterize the sound radiation behavior from the cylindrical structures. The physical significance of the ring frequency, f_R, is that it is the lowest frequency at which a structural breathing mode resonance can occur [14]. It is calculated by

$$f_R = \frac{c_p}{2\boldsymbol{p}a} \text{ (Hz)},\tag{3.6}$$

where $c_p = \sqrt{E/\boldsymbol{r}_p(1-\boldsymbol{m}^2)}$ is the speed of sound in a flat panel of the same thickness and material as the cylindrical shell with radius a, E is the Young's modulus of the cylindrical shell material, $\boldsymbol{m}$ is the Poisson's ratio, and $\boldsymbol{r}_p$ is the density of the material. The ring frequency sets a threshold for the stiffness effects of the cylindrical curvature. Below the ring frequency, the stiffness effects of the cylindrical curvature are large, and the motion around the circumference is constrained by the extensional stiffness about the circumference. Above the ring frequency the stiffness effects of the curvature are small, and the flexural motion of the cylindrical shell is much like that of a flat panel.

Cutoff frequency is use to characterize sound propagation through the cavity inside the cylindrical shell. It is defined as the acoustic cavity resonance frequency below which a particular cavity mode cannot propagate freely and carry energy along axis direction [14]. Although this effect is not important for a short cylinder, the lowest cutoff frequency, f_{Cut}, can be used to characterize the coupled vibration of the cylindrical shell and the interior acoustic cavity. The lowest cutoff frequency is given by [14]

$$f_{Cut} = 1.84\frac{c}{2\boldsymbol{p}a} \text{ (Hz)},\tag{3.7}$$

where c is the speed of sound propagating in the cavity medium, and a is the radius of the cylindrical cavity.

Another important frequency for characterizing the coupled vibration of the structure and acoustics is the critical frequency, which is the lowest coincidence frequency. The strongest modal radiation occurs at or above the critical frequency [14]. For a cylindrical shell, there are an

internal coincidence and an external coincidence. The external coincidence happens when the external acoustic wavenumber equals the bending wavenumber of the cylindrical shell. The internal coincidence occurs when the internal acoustic and structural axial wave numbers are equal for a given circumferential mode. The internal critical frequency is equal to the cutoff frequency, and the external critical frequency corresponds to the critical frequency for a flat panel with the same material and thickness. They are calculated with the following respective formulas:

$$f_{Cr\_int} = f_{Cut} \, , \tag{3.8}$$

$$f_{Cr\_ext} = \frac{c^2}{2p} \sqrt{\frac{m}{B}} \, , \tag{3.9}$$

where $m = h\, r$ is the surface area density of the shell, and $B = Eh^3/12(1 - m^2)$ is the bending stiffness of the plate of the same material and thickness. At the coincidence frequencies spatial resonances occur, and the radiation or transmission of noise through the cylindrical shell is more efficient.

The material properties of the AGS fairing are as follows: the average isotropic Young's modulus, which was obtained from a parametric FEA study in reference [34, 35] is $E = 60$ GPa, and the Poisson's ratio was selected as $m = 0.3$, and the density of the skin material was measured as $r = 1500$ kg/m^3. The speed of sound in air at 75° F is $c = 346$ m/s. The geometric dimensions of the AGS tapered cylindrical shell are as follows: the radius of the small end, $R_1 = 190$ mm, the radius of the big end, $R_2 = 305$ mm, the height of the cylinder, $H = 560$ mm, and the effective skin thickness of the shell, $h = 10$ mm, which was obtained from parametric FEA [34, 35]. The material physical parameters and geometric dimensions of the ChamberCore cylindrical fairing are given in Table 3.1.

The ring frequency, cutoff frequency and internal and external critical frequencies of both the AGS and the ChamberCore fairings are calculated in the end of this section, which will be used in characterizing noise transmission into the two fairings later.

Table 3.2 Ring, Cutoff, Critical Frequencies for the AGS and ChamberCore Fairings

	AGS fairing	ChamberCore fairing
Ring frequency (Hz), $a=R_1$	5300	8689
Cut off frequency (Hz)	989	397
Internal critical frequency (Hz)	989	397
External critical frequency (Hz)	336	227

3.3 Exterior Pressure of an Infinite Elastic Cylindrical Shell

The theoretical model of noise reduction spectrum consists of a plane sound wave obliquely impinging upon the flexible cylindrical shell, the scattering wave of the cylindrical shell, and the cylindrical cavity acoustics. The sum of incident and scattered pressure forms the exterior pressure field of the cylindrical shell, and can be written as

$$p_{ext} = p_i + p_{se}, \tag{3.10}$$

where p_{ext} is the exterior pressure, p_i the incident pressure, p_{se} the scattered pressure by the elastic shell, which is calculated from

$$p_{se} = p_{s\infty} + p_{re}, \tag{3.11}$$

where $p_{s\infty}$ is the scattered pressure by a rigid-cylinder with infinite acoustic impedance, and p_{re} is the radiated pressure by an elastic cylindrical shell.

The calculation of exterior pressure over the outside shell is a near-field problem, which is difficult to analytically solve for a finite elastic cylindrical shell [47]. In this study, the near-field pressure of an infinite elastic cylindrical shell is used to approximate p_{se} for the finite one. The internal pressure is derived using modal-interaction model [45, 75, 76], and the solved approximated external pressure is used as its input. In order to simplify analysis it is assumed that all time dependant variables are time harmonic.

3.3.1   Oblique Incident Plane Sound Wave

The specific problem studied is shown in Figure 3.2. Consider an oblique plane wave impinging upon an infinite thin cylindrical shell approaching from the radial plane ($f = p$). The density of the fluid and the speeds of sound are r_1, c_1 and r_2, c_2, in the external and internal media, respectively. In the analysis of exterior pressure field, all waves will be assumed to have the same dependence on the axial co-ordinate z.
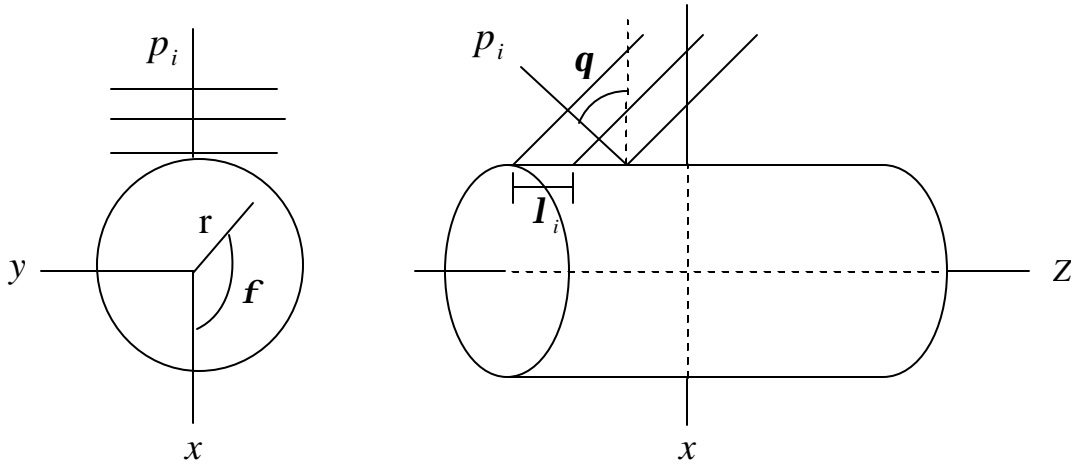
Figure 3.2 Geometry and Incident Wave of a Cylindrical Shell

The incident sound wave can be represented as

$$p_i(x, z, t) = P_i e^{j(w - k_{1x}x - k_{1z}z)},$$

(3.12)

where P_i is the amplitude of incident sound pressure, k_{1x} and k_{1z} are the x-component and z-component of the wavenumber, respectively, and computed from

$$k_{1x} = k_1 \cos q, \qquad k_{1z} = k_1 \sin q, \qquad (3.13)$$

wher $k_1 = w/c_1$ is the wavenumber in the external fluid medium, q is the incident angle. Substituting $x = r\cos f$ into Eq. (3.12), p_i can be re-written as

$$p_i(x, z, t) = P_i e^{j(wt - k_{1z}z)} e^{-jk_{1r}r\cos f}, \qquad (3.14)$$

where $k_{1r} = k_{1x}$ is the radial component of the wavenumber. Expanding the term $e^{-jk_{1r}r\cos f}$ in Eq. (3.14) with Bessel function [41, 47, 92] gives

$$p_i(x, z, t) = P_i e^{j(wt - k_{1z}z)} \sum_{m=0}^{\infty} e_m (-j)^m J_m(k_{1r}r)\cos mf, \qquad (3.15)$$

where e_m is the Neumann factor given by

$$e_m = \begin{cases} 1 & (m = 0) \\ 2 & (m \geq 1) \end{cases}, \qquad (3.16)$$

and J_m is the Bessel function of the first kind of integer order m^{th}.

3.3.2   Radiation of a Vibrating Cylindrical Shell

Inspecting Eqs. (3.10) and (3.11), the external pressure consists of not only the incident pressure but also the scattered pressure of the rigid-cylinder and the radiated pressure by the elastic cylindrical shell. The latter two kinds of pressure are determined from the solution of sound radiation. Assuming that the shell is vibrating with a surface-harmonic acceleration distribution $\ddot{w}(r = a, f, z, t)$, it can be expanded into a Fourier series as

$$\ddot{w}(r = a, f, z, t) = e^{-jk_{1z}z} \sum_{m=0}^{\infty} \ddot{W}_m(t)\cos(mf), \qquad (3.17)$$

where a is the radius of the midsurface, k_{1z} is the z-components of the wavenumber given by Eq. (3.13). Only is the configuration in even f considered in Eq. (3.17). If the f axis cannot be

oriented to make this configuration, a sine series is required. Because the corresponding development parallels the procedure presented here for even configuration, the odd configuration is not specifically included.

In order to solve the radiation pressure from the vibrating shell, let's consider a differential volume element of length dx, cross-section area S, and mass r_1Sdx located in a compressible fluid medium of density r_1. The forces acting on the two faces perpendicular to the x axis are shown in Figure 3.3. They are considered positive in the positive x direction.
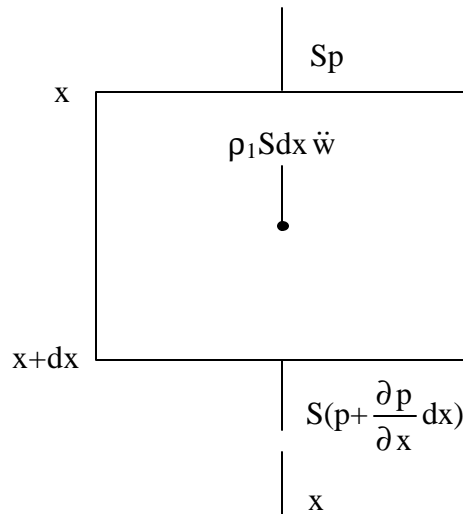
Figure 3.3 Forces Acting on a Fluid Volume Element

Through balancing the forces in Figure 3.3 and rearranging the equation, the following equation can be obtained

$$\frac{\partial p}{\partial x} = -r_1 \frac{\partial^2 w}{\partial t^2}. \tag{3.18}$$

This equation is referred as Euler's equation. The boundary condition which is held by the fluid is

$$\frac{\partial p(r,\boldsymbol{f},z,t)}{\partial r}\bigg|_{r=a} = -\boldsymbol{r}_1 \ddot{w}(r=a,\boldsymbol{f},z,t) , \qquad (3.19)$$

where $\ddot{w}(r=a,\boldsymbol{f},z,t)$ is the fluid particle acceleration in the boundary which is equated with the acceleration of the vibrating shell. In order to satisfy the boundary condition, the radiation pressure field is therefore expressible as the series [41, 47]

$$p_r(r,\boldsymbol{f},z,t) = e^{-jk_{1z}z} \sum_{m=0}^{\infty} P_m(t) H_m^{(2)}(k_{1r}r)\cos(m\boldsymbol{f}), \qquad (3.20)$$

where $H_m^{(2)}$ is the Hankel function of the second kind of integer order m^{th}. $P_m(t)$ will be determined by Euler's equation and the boundary condition.

Substituting Eq. (3.20) into (3.19), and using Eq. (3.17), the coefficients $P_m(t)$ can be solved as

$$P_m(t) = -\frac{\boldsymbol{r}_1 \ddot{W}_m(t)}{k_{1r} H_m^{(2)\prime}(k_{1r}a)} , \qquad (3.21)$$

where is $H_m^{(2)\prime}$ the derivative of the second kind Hankel function. The radiation pressure field is thus found to be

$$p_r(r,\boldsymbol{f},z,t) = -e^{-jk_{1z}z} \frac{\boldsymbol{r}_1}{k_{1r}} \sum_{m=0}^{\infty} \frac{\ddot{W}_m(t)}{H_m^{(2)\prime}(k_{1r}a)} H_m^{(2)}(k_{1r}r)\cos(m\boldsymbol{f}) . \qquad (3.22)$$

Because $W_m(t)$ is time harmonic, the surface pressure obtained from Eq. (3.22) can be written in terms of modal specific acoustic impedances z_m as

$$p_r(r=a,\boldsymbol{f},z,t) = e^{-jk_{1z}z} \sum_{m=0}^{\infty} \dot{W}_m(t) z_m \cos(m\boldsymbol{f}), \qquad (3.23)$$

where

$$\ddot{W}_m(t) = j\boldsymbol{w}\dot{W}_m(t), \qquad (3.24)$$

$$z_m = -\frac{j\boldsymbol{r}_1\boldsymbol{w}H_m^{(2)}(k_{1r}a)}{k_{1r}H_m^{(2)'}(k_{1r}a)}. \tag{3.25}$$

3.3.3   Scattering from an Infinite Rigid Cylindrical Shell

The incident sound wave is the same as that in Section 3.3. Because the boundary is rigid, the resultant particle acceleration in the boundary must have a zero component along the normal direction to boundary:

$$\ddot{w}_{s\infty}(r=a,\boldsymbol{f},z,t)+\ddot{w}_i(r=a,\boldsymbol{f},z,t)=0, \tag{3.26}$$

where $\ddot{w}_{s\infty}$ is the normal rigid surface acceleration, and $\ddot{w}_i$ is the normal incident fluid particle acceleration. This acceleration is given by Euler's equation (3.18) or boundary condition Eq. (3.19)

$$\ddot{w}_i(r=a,\boldsymbol{f},z,t)=-\frac{1}{\boldsymbol{r}_1}\frac{\partial p_i(r,\boldsymbol{f},z,t)}{\partial r}\bigg|_{r=a}. \tag{3.27}$$

Combining Eqs. (3.15), (3.26) and (3.27), the rigid surface acceleration can be obtained as

$$\ddot{w}_{s\infty}(r=a,\boldsymbol{f},z,t)=P_i(t)e^{-jk_{1z}z}\frac{k_{1r}}{\boldsymbol{r}_1}\sum_{m=0}^{\infty}\boldsymbol{e}_m(-j)^m J_m{}'(k_{1r}a)\cos m\boldsymbol{f}, \tag{3.28}$$

where $\boldsymbol{e}_m$ is the Neumann factor given by Eq. (3.16), and $J_m{}'$ is the derivative of first kind Bessel function. Therefore, the coefficients in Eq. (3.17) can be expressed as

$$\ddot{W}_m(t)=P_i(t)\frac{k_{1r}}{\boldsymbol{r}_1}\boldsymbol{e}_m(-j)^m J_m{}'(k_{1r}a). \tag{3.29}$$

Substituting Eq. (3.29) into Eq. (3.22), the scattered pressure from an infinite rigid cylindrical shell is obtained

33

$$p_{s\infty}(r, \pmb{f}, z, t) = P_i(t)e^{-jk_{1z}z} \sum_{m=0}^{\infty} \pmb{e}_m(-j)^m A_m H_m^{(2)}(k_{1r}r)\cos(m\pmb{f}),\qquad(3.30)$$

where

$$A_m = -\frac{J_m^{'}(k_{1r}a)}{H_m^{(2)'}(k_{1r}a)}.\qquad(3.31)$$

A_m can be represented as a complex number like:

$$A_m = A_m^R + jA_m^I,\qquad(3.32)$$

where A^R and A^I are the real part and imaginary part, respectively, and computed from

$$A_m^R = -\frac{J_m^{'2}(k_{1r}a)}{J_m^{'2}(k_{1r}a) + Y_m^{'2}(k_{1r}a)},\qquad(3.33)$$

$$A_m^I = -\frac{J_m^{'}(k_{1r}a)Y_m^{'}(k_{1r}a)}{J_m^{'2}(k_{1r}a) + Y_m^{'2}(k_{1r}a)},\qquad(3.34)$$

where J_m is the Bessel function of the first kind of integer order m^{th}, and Y_m is the Bessel function of the second kind of integer order m^{th}.

The resultant pressure on the cylindrical surface from the sum of the incident wave and the scattered wave of the rigid cylinder is required by analyzing the scattering action of elastic cylindrical shells, which is calculated from

$$p(r = a, \pmb{f}, z, t) = P_i(t)e^{-jk_{1z}z} \sum_{m=0}^{\infty} \pmb{e}_m(-j)^m \left[J_m(k_{1r}a) - \frac{J_m^{'}(k_{1r}a)H_m^{(2)}(k_{1r}a)}{H_m^{(2)'}(k_{1r}a)} \right]\cos(m\pmb{f}).\quad(3.35)$$

Considering the following relationship

$$J_m(x)H_m^{(2)'}(x) - J_m^{'}(x)H_m^{(2)}(x) = -j\frac{2}{\pmb{p}x},\qquad(3.36)$$

Eq. (3.35) is simplified as

34

$$p(r = a, \boldsymbol{f}, z, t) = \frac{2P_i(t)}{\boldsymbol{p} a k_{1r}} e^{-jk_{1z}z} \sum_{m=0}^{\infty} \boldsymbol{e}_m (-j)^{m+1} \frac{1}{H_m^{(2)\prime}(k_{1r}a)} \cos(m\boldsymbol{f}) . \qquad (3.37)$$

3.3.4 Scattering from an Infinite Elastic Cylindrical Shell

The incident sound wave is the same as that in Section 3.3. The normal response of the elastic cylindrical shell under $(p = p_i + p_s)$ can be expressed in terms of modal mechanical and acoustic impedance as [47]

$$\dot{w}(r = a, \boldsymbol{f}, z, t) = e^{-jk_{1z}z} \sum_{m=0}^{\infty} \frac{P_m(t)}{z_m + Z_m} \cos(m\boldsymbol{f}) , \qquad (3.38)$$

where z_m is the modal specific acoustic impedance, and can be obtained from Eq. (3.25), Z_m is the modal mechanical impedance, and can be determined from Donnell's equations under the absence of the pressure inside of the cylinder, which leads to the expression for the modal mechanical impedance in the form [47]

$$Z_m = j \frac{c_p \boldsymbol{r}_s h}{a} \frac{\left[\Omega^2 - (\Omega_m^{(1)})^2 \right] \left[\Omega^2 - (\Omega_m^{(2)})^2 \right]}{\Omega(\Omega^2 - m^2)} , \qquad (3.39)$$

where $\boldsymbol{r}_s$ is the volume density of the shell material, $c_p = \sqrt{E / \boldsymbol{r}_p (1 - \boldsymbol{m}^2)}$ is the speed of sound propagating in the shell, a is the radius of midsurface, h is the thickness of the shell. Ω is a dimensionless frequency parameter, $\Omega_m^{(1)}$, and $\Omega_m^{(2)}$ are the resonance frequencies of a planar vibrating thin cylindrical shell, and they are defined as

$$\Omega = \frac{wa}{c_p} , \qquad (3.40)$$

$$\Omega_m^{(1)} = \frac{1}{2} \left[1 + m^2 + \boldsymbol{b}m^4 - \sqrt{\left(1 + m^2 + \boldsymbol{b}m^4\right)^2 - 4\boldsymbol{b}m^6} \right] , \qquad (3.41)$$

$$\Omega_m^{(2)} = \frac{1}{2}\left[1 + m^2 + \pmb{b}m^4 + \sqrt{\left(1 + m^2 + \pmb{b}m^4\right)^2 - 4\pmb{b}m^6}\right],$$ (3.42)

where

$$\pmb{b} = \frac{h^2}{12a^2}.$$ (3.43)

$P_m(t)$ can be obtained from Eq. (3.37) as

$$P_m(t) = \frac{2P_i(t)}{\pmb{p}ak_{1r}H_m^{(2)\prime}(k_{1r}a)}\pmb{e}_m(-j)^{m+1}.$$ (3.44)

Using Eq. (3.38), the coefficients of the surface-harmonic acceleration distribution is

$$\ddot{W}_m(t) = j\pmb{w}\dot{W}_m(t) = \frac{j\pmb{w}P_m(t)}{z_m + Z_m}.$$ (3.45)

Substitute Eqs. (3.45) into Eq. (3.22), using Eq. (3.44), the radiation pressure from the infinite elastic cylindrical shell is

$$p_{re}(r,\pmb{f},z,t) = P_i(t)e^{-jk_{1z}z}\sum_{m=0}^{\infty}\pmb{e}_m(-j)^m B_m H_m^{(2)}(k_{1r}r)\cos(m\pmb{f}),$$ (3.46)

where

$$B_m = -\frac{2\pmb{r}_1\pmb{w}}{\pmb{p}ak_{1r}^2(z_m + Z_m)\left[H_m^{(2)\prime}(k_{1r}a)\right]^2}.$$ (3.47)

$(z_m + Z_m)$ can be represented by a complex number as:

$$z_m + Z_m = Z_m^R + jZ_m^I,$$ (3.48)

where Z^R and Z^I are computed by

$$Z_m^R = \frac{\boldsymbol{r}_1\boldsymbol{w}\left[J_m(k_{1r}a)Y_m{}'(k_{1r}a) - J_m{}'(k_{1r}a)Y_m(k_{1r}a)\right]}{k_{1r}\left[J_m{}'^2(k_{1r}a) + Y_m{}'^2(k_{1r}a)\right]}, \tag{3.49}$$

$$Z_m^I = \frac{c_p \boldsymbol{r}_s h}{a}\frac{\left[\Omega^2 - \left(\Omega_m^{(1)}\right)^2\right]\left[\Omega^2 - \left(\Omega_m^{(2)}\right)^2\right]}{\Omega\left(\Omega^2 - m^2\right)} - \frac{\boldsymbol{r}_1\boldsymbol{w}\left[J_m(k_{1r}a)J_m{}'(k_{1r}a) + Y_m(k_{1r}a)Y_m{}'(k_{1r}a)\right]}{k_{1r}\left[J_m{}'^2(k_{1r}a) + Y_m{}'^2(k_{1r}a)\right]}, \tag{3.50}$$

where J_m is the Bessel function of the first kind of integer order m^{th}, and Y_m is the Bessel function of the second kind of integer order m^{th}. B_m can also be represented as a complex number like:

$$B_m = B_m^R + jB_m^I, \tag{3.51}$$

where B^R and B^I are the real part and imaginary part, respectively, and computed from

$$B_m^R = \frac{-\dfrac{2\boldsymbol{r}_1\boldsymbol{w}}{\boldsymbol{p}ak_{1r}^2}\left\{Z_m^R\left[J_m{}'^2(k_{1r}a) - Y_m{}'^2(k_{1r}a)\right] + 2Z_m^I J_m{}'(k_{1r}a)Y_m{}'(k_{1r}a)\right\}}{\left\{Z_m^R\left[J_m{}'^2(k_{1r}a) - Y_m{}'^2(k_{1r}a)\right] + 2Z_m^I J_m{}'(k_{1r}a)Y_m{}'(k_{1r}a)\right\}^2 + \left\{Z_m^I\left[J_m{}'^2(k_{1r}a) - Y_m{}'^2(k_{1r}a)\right] - 2Z_m^R J_m{}'(k_{1r}a)Y_m{}'(k_{1r}a)\right\}^2}, \tag{3.52}$$

$$B_m^I = \frac{\dfrac{2\boldsymbol{r}_1\boldsymbol{w}}{\boldsymbol{p}ak_{1r}^2}\left\{Z_m^I\left[J_m{}'^2(k_{1r}a) - Y_m{}'^2(k_{1r}a)\right] - 2Z_m^R J_m{}'(k_{1r}a)Y_m{}'(k_{1r}a)\right\}}{\left\{Z_m^R\left[J_m{}'^2(k_{1r}a) - Y_m{}'^2(k_{1r}a)\right] + 2Z_m^I J_m{}'(k_{1r}a)Y_m{}'(k_{1r}a)\right\}^2 + \left\{Z_m^I\left[J_m{}'^2(k_{1r}a) - Y_m{}'^2(k_{1r}a)\right] - 2Z_m^R J_m{}'(k_{1r}a)Y_m{}'(k_{1r}a)\right\}^2}. \tag{3.53}$$

The external pressure of the infinite elastic cylindrical shell is computed from

$$p_{ext}(r,\boldsymbol{f},t) = p_i(r,\boldsymbol{f},t) + p_{s\infty}(r,\boldsymbol{f},t) + p_{re}(r,\boldsymbol{f},t). \tag{3.54}$$

Substituting Eqs. (3.15), (3.30) and (3.46) into Eq. (3.54), yields

$$p_{ext}(r,\boldsymbol{f},z,t) = P_i(t)e^{-jk_{1z}z}\sum_{m=0}^{\infty}\boldsymbol{e}_m(-j)^m\left[J_m(k_{1r}r) + C_m H_m^{(2)}(k_{1r}r)\right]\cos(m\boldsymbol{f}), \tag{3.55}$$

where

$$C_m = A_m + B_m. \tag{3.56}$$

A_m is given by Eq. (3.31), and B_m is given by Eq. (3.47). C_m can be represented as a sum of a real part C_m^R and imaginary part C_m^I like

$$C_m = C_m^R + jC_m^I, \tag{3.57}$$

where

$$C_m^R = A_m^R + B_m^R, \tag{3.58}$$

$$C_m^I = A_m^I + B_m^I, \tag{3.59}$$

and A^R, A^I, B^R, and B^I are computed from Eqs. (3.33), (3.34), (3.52), and (3.53), respectively.

Because the incident pressure is time harmonic, i.e. $P_i(t) = P_i e^{jwt}$, the external pressure field for the infinite flexible cylindrical shell is

$$p_{ext}(r = a, \boldsymbol{f}, z, t) = P_i e^{jwt - jk_{1z}z} \sum_{m=0}^{\infty} \boldsymbol{e}_m (-j)^m \left[J_m(k_{1r}a) + C_m H_m^{(2)}(k_{1r}a) \right] \cos(m\boldsymbol{f}), \tag{3.60}$$

where P_i is the magnitude of incident pressure, J_m is the Bessel function of the first kind of integer order m^{th}, coefficient C_m is given by Eq. (3.56), and $H_m^{(2)}$ is the Hankel function of the second kind of integer order m^{th}.

3.4   Interior Pressure of a Finite Elastic Cylindrical Shell

It is assumed that the end caps of the finite cylindrical structure are rigid, so that only the radial motion of the curved surface of the cylindrical structure excites the acoustic cavity. The modal-interaction principle [45] is used to calculate the sound pressure inside the cavity under the excitation of external pressure which is approximated by the one obtained from the infinite cylindrical shell (see Eq. (3.60)). The structural vibration and acoustic field are expressed

directly in terms of their uncoupled modes (structural modes under "*in-vacuo*" condition, and acoustic cavity modes with the "*rigid-wall*" condition). Only the normal motion of the cylindrical shell is considered to excite the cavity acoustics, and also only the even f configuration is considered. Choosing either odd ($\sin(mf)$ modes) or even ($\cos(mf)$ modes) is arbitrary, since $f=0°$ can be changed. The odd f configuration parallels the procedure for the even configuration proposed here, the odd configuration is thus not specifically studied here. For a simply supported cylindrical shell the harmonic radial displacement of the shell, subject to external pressure excitation, can be described as a linear combination of modes as

$$w(r = a, f, z, t) = \sum_{o=0}^{\infty} \sum_{q=1}^{\infty} W_{oq}(t)\Phi_{oq}(f, z),$$ (3.61)

where $o=0,1,2,3…$ is the number of circumferential waves in structural mode shapes, and $q=1,2,3…$ is the number of longitudinal half-waves in structural mode shapes. The structural normal mode shapes *in-vacuo* can be written as

$$\Phi_{oq}(f, z) = \cos(of)\sin(q\frac{p}{L}z),$$ (3.62)

where L is the length of the finite cylindrical shell. The natural frequencies of a simply supported cylindrical shell without axial constraint can be calculated from [48].

$$w_{oq}^{s} = \frac{l_{oq}c_{p}}{a},$$ (3.63)

where the superscript s in w_{oq}^{s} means "structure."

For simply supported long cylindrical shells without axial constraint, if the modes are pure radial modes, l_{oq} is

$$l_{oq} = 1, \qquad o=0 \text{ and } q=1,2,3…$$ (3.64)

If the modes are bending modes, l_{oq} is

$$l_{oq} = \left(\frac{qpa}{L}\right)^2 \sqrt{\frac{1-m^2}{2}} , \quad o=1 \text{ and } q=1,2,3\ldots \tag{3.65}$$

If the modes are radial-axial modes, l_{oq} is

$$l_{oq} = \frac{1}{\left(\frac{qpa}{L}\right)^2 + o^2} \sqrt{(1-m^2)\left(\frac{qpa}{L}\right)^4 + \frac{h^2}{12a^2}\left[o^2 + \left(\frac{qpa}{L}\right)^2\right]^4} , \quad o=2,3,4,\ldots \text{ and } q=1,2,3\ldots \tag{3.66}$$

Because the structural torsional modes and axial modes do not induce the volume change, they are neglected here.

The modal equation of the structure can then be derived by taking advantages of the orthogonal properties of the mode shapes in the form of [45]

$$\ddot{W}_{oq}(t) + 2x_{oq}^s w_{oq}^s \dot{W}_{oq}(t) + (w_{oq}^s)^2 W_{oq}(t) = \frac{S}{M_{oq}} \sum_{l,m,n=0}^{\infty} P_{lmn}(t) D_{oqlmn} + \frac{p_{oq}(t)}{M_{oq}} . \tag{3.67}$$

In the right hand part of Eq. (3.67), the first term is the cavity fluid loading, and the second term is the external distribution input, where M_{oq} is modal mass of the structure, $D_{oq,lmn}$ is the dimensionless structural-acoustic coupling coefficient, $p_{oq}(t)$ is the modal force, $P_{lmn}(t)$ is the time-dependent part of the interior pressure, o, q are the number of circumferential waves and longitudinal half-waves in structure mode shapes, respectively, l, m and n are the number of radial nodes, diametric nodes and longitudinal nodes in acoustic cavity mode shapes, respectively, and $S=2paL$ is the area of the shell surface. M_{oq}, $D_{oq,lmn}$, and $p_{oq}(t)$ are given by the following equations, respectively.

$$M_{oq} = \int_S m_s \Phi_{oq}^2(f,z)dS , \tag{3.68}$$

$$D_{oqlmn} = \frac{1}{S}\int_S \Phi_{oq}(f,z)\Psi_{lmn}(r=a,f,z)\,dS , \tag{3.69}$$

$$p_{oq}(t) = \int_S p_{ext}(r = a, \mathbf{f}, z, t)\Phi_{oq}(\mathbf{f}, z)\, dS = P_i e^{jwt} E_{oq} \,, \tag{3.70}$$

where the structure modes Φ_{oq} is given by Eq. (3.62), the acoustic modes Ψ_{lmn} is given by Eq. (3.83), and the pressure p_{ext} is given by Eq. (3.60), which is an approximation for the finite one. For the uniform cylindrical shell with surface density m_s, coefficients M_{oq}, $D_{oq,lmn}$, and E_{op} are computed from the following equations:

$$M_{oq} = \frac{1}{2} v_o m_s L a \mathbf{p} \,, \tag{3.71}$$

where v_o is a constant factor defined as

$$v_o = \begin{cases} 2, & o = 0 \\ 1, & o > 0 \end{cases} \tag{3.72}$$

and

$$D_{oqlmn} = \begin{cases} \dfrac{aL}{S}\left[\dfrac{1-\cos(q+n)\,\mathbf{p}}{q+n}+\dfrac{1-\cos(q-n)\mathbf{p}}{q-n}\right], & (l = m = o = 0 \text{ and } q \neq n) \\[3mm] \dfrac{aL}{2S} v_m J_m(k_{lm}a)\left[\dfrac{1-\cos(q+n)\,\mathbf{p}}{q+n}+\dfrac{1-\cos(q-n)\mathbf{p}}{q-n}\right], & (l \in [0,\infty], m \in [1,\infty], n \in [0,\infty] \\[1mm] \qquad\qquad\qquad \text{or } l \in [1,\infty], m \in [0,\infty], n \in [0,\infty]) \text{ and } (o = m \text{ and } q \neq n) \\[2mm] 0, & \text{others} \end{cases} \tag{3.73}$$

where v_m is given by Eq. (3.72), and

$$E_{oq} = \int_S e^{-jk_{1z}z}\sum_{m=0}^{\infty} \mathbf{e}_m (-j)^m \left[J_m(k_{1r}a) + C_m H_m^{(2)}(k_{1r}a)\right]\cos(m\mathbf{f})\cos(o\mathbf{f})\sin(q\frac{\mathbf{p}}{L}z)\,dS \,. \tag{3.74}$$

Integrating Eq. (3.74) over the cylindrical surface, obtains

41

$$E_{oq} = \begin{cases} (-j)^{o+1} aL\boldsymbol{p}\left[J_o(k_{1r}a) + C_o H_o^{(2)}(k_{1r}a) \right], & \left(k_{1z} = q\dfrac{\boldsymbol{p}}{L} \right) \\[4mm] (-j)^o aL\boldsymbol{p}\left[J_o(k_{1r}a) + C_o H_o^{(2)}(k_{1r}a) \right] \left\{ \left[\dfrac{-\cos(k_{1z}L + q\boldsymbol{p}) + 1}{k_{1z}L + q\boldsymbol{p}} + \dfrac{\cos(k_{1z}L - q\boldsymbol{p}) - 1}{k_{1z}L - q\boldsymbol{p}} \right] + j\left[\dfrac{\sin(k_{1z}L + q\boldsymbol{p})}{k_{1z}L + q\boldsymbol{p}} - \dfrac{\sin(k_{1z}L - q\boldsymbol{p})}{k_{1z}L - q\boldsymbol{p}} \right] \right\}, \\[4mm] & \left(k_{1z} \neq q\dfrac{\boldsymbol{p}}{L} \right) \end{cases} \quad (3.75)$$

E_{oq} can be rewritten as the following expression:

$$E_{oq} = (-j)^o (V_{oq}^R + jV_{oq}^I), \qquad (3.76)$$

where

$$V_{oq}^R = \begin{cases} aL\boldsymbol{p}\left[C_o^I J_o(k_{1r}a) - C_o^R Y_o(k_{1r}a) \right], & \left(k_{1z} = q\dfrac{\boldsymbol{p}}{L} \right) \\[4mm] aL\boldsymbol{p}\left[\left(C_o^R + 1\right) J_o(k_{1r}a) + C_o^I Y_o(k_{1r}a) \right]\left[\dfrac{-\cos(k_{1z}L + q\boldsymbol{p}) + 1}{k_{1z}L + q\boldsymbol{p}} + \dfrac{\cos(k_{1z}L - q\boldsymbol{p}) - 1}{k_{1z}L - q\boldsymbol{p}} \right] \\[4mm] -aL\boldsymbol{p}\left[C_o^I J_o(k_{1r}a) - C_o^R Y_o(k_{1r}a) \right]\left[\dfrac{\sin(k_{1z}L + q\boldsymbol{p})}{k_{1z}L + q\boldsymbol{p}} - \dfrac{\sin(k_{1z}L - q\boldsymbol{p})}{k_{1z}L - q\boldsymbol{p}} \right], & \left(k_{1z} \neq q\dfrac{\boldsymbol{p}}{L} \right) \end{cases} , \quad (3.77)$$

$$V_{oq}^I = \begin{cases} aL\boldsymbol{p}\left[\left(C_o^R + 1\right) J_o(k_{1r}a) + C_o^I Y_o(k_{1r}a) \right], & \left(k_{1z} = q\dfrac{\boldsymbol{p}}{L} \right) \\[4mm] aL\boldsymbol{p}\left[C_o^I J_o(k_{1r}a) - C_o^R Y_o(k_{1r}a) \right]\left[\dfrac{-\cos(k_{1z}L + q\boldsymbol{p}) + 1}{k_{1z}L + q\boldsymbol{p}} + \dfrac{\cos(k_{1z}L - q\boldsymbol{p}) - 1}{k_{1z}L - q\boldsymbol{p}} \right] \\[4mm] +aL\boldsymbol{p}\left[\left(C_o^R + 1\right) J_o(k_{1r}a) + C_o^I Y_o(k_{1r}a) \right]\left[\dfrac{\sin(k_{1z}L + q\boldsymbol{p})}{k_{1z}L + q\boldsymbol{p}} - \dfrac{\sin(k_{1z}L - q\boldsymbol{p})}{k_{1z}L - q\boldsymbol{p}} \right], & \left(k_{1z} \neq q\dfrac{\boldsymbol{p}}{L} \right) \end{cases} , \quad (3.78)$$

where J_o is the Bessel function of the first kind of integer order o^{th}, and Y_o is the Bessel function of the second kind of integer order o^{th}, k_{1z} is the z-component of the wavenumber in external fluid medium given by Eq. (3.13).

The interior sound field of the cylindrical shell is governed by the inhomogeneous wave equation [45]

$$\Delta^2 p - \frac{1}{c_2^2}\frac{\partial^2 p}{\partial t^2} = -\boldsymbol{r}_2 \frac{\partial s}{\partial t}, \tag{3.79}$$

where c_2 is the speed of sound in fluid medium of the cylindrical cavity, $\boldsymbol{r}_2$ is the density of the fluid medium in the cavity, s is the distribution of source volume velocity per unit volume. The small piece of shell located at $(r=a, \boldsymbol{f}_0, z_0)$ is a sound source of the sound field with a volume velocity distribution per unit volume of [45]

$$s(r = a, \boldsymbol{f}, z, t) = -2\frac{\partial w(r = a, \boldsymbol{f}, z, t)}{\partial t}\boldsymbol{d}(\boldsymbol{f}-\boldsymbol{f}_0, z-z_0) . \tag{3.80}$$

Substituting Eq. (3.80) into Eq. (3.79), yields

$$\nabla^2 p - \frac{1}{c_2^2}\frac{\partial^2 p}{\partial t^2} = 2\boldsymbol{r}_2 \frac{\partial^2 w(r = a, \boldsymbol{f}, t)}{\partial t^2}\boldsymbol{d}(\boldsymbol{f}-\boldsymbol{f}_0, z-z_0) . \tag{3.81}$$

The acoustic pressure in the cavity is expressed as a linear combination of the acoustic cavity modes with rigid boundaries:

$$p(r, \boldsymbol{f}, z, t) = \sum_{l,m\ n=0}^{\infty} P_{lmn}(t)\Psi_{lmn}(r, \boldsymbol{f}, z) . \tag{3.82}$$

The cylindrical acoustic cavity mode shapes and corresponding angular frequency are

$$\Psi_{lmn}(r, \boldsymbol{f}, z) = \begin{cases} \cos(n\dfrac{\boldsymbol{p}}{L}z), & l, m = 0, n \in [1, \infty] \\ J_m(k_{lm}r)\cos(m\boldsymbol{f})\cos(n\dfrac{\boldsymbol{p}}{L}z), & l \in [0, \infty], m \in [1, \infty], n \in [0, \infty] , \\ & \text{or } l \in [1, \infty], m \in [0, \infty], n \in [0, \infty] \end{cases} \tag{3.83}$$

$$\boldsymbol{w}_{lmn}^{f} = c_2\sqrt{k_{lm}^2 + (n\frac{\boldsymbol{p}}{L})^2} , \tag{3.84}$$

where l, m and n are the number of radial nodes, diametric nodes and longitudinal nodes in acoustic cavity mode shapes, respectively, and w^f is the acoustic natural frequency. Note that l, m, and n cannot be zero at the same time, because the $(0,0,0)$ mode is not considered in this study. k_{lm} can be solved from

$$J_m{}'(k_{lm}r)\Big|_{r=a}=0 . \tag{3.85}$$

In Eq. (3.83), the upper term is the pure longitudinal modes, and the lower term is other else modes.

Using the orthogonal properties of modal shapes and considering the damping term, the modal equation for the acoustic system is written as [45]

$$\ddot{P}_{lmn}(t)+2\boldsymbol{x}_{lmn}^f\boldsymbol{w}_{lmn}^f\dot{P}_{lmn}(t)+(\boldsymbol{w}_{lmn}^f)^2 P_{lmn}(t)=-\frac{\boldsymbol{r}_2 c_2^2 S}{\Lambda_{lmn}}\sum_{o=0,q=1}^{\infty}\ddot{W}_{oq}(t)D_{oqlmn}, \tag{3.86}$$

where the superscript f in Eq. (3.86) means "fluid", and

$$\Lambda_{lmn}=\int_V \Psi_{lmn}^2(r,\boldsymbol{f},z)dV . \tag{3.87}$$

For a cylindrical cavity with length L and midsurface radius a, it can be computed from

$$\Lambda_{lmn}=\begin{cases}\dfrac{1}{2}\boldsymbol{p}a^2 L, & l=m=0, n\in[1,\infty] \\[2mm] \dfrac{1}{4}\boldsymbol{p}a^2 Lv_m v_n\left\{\left[J_m{}'(k_{lm}a)\right]^2+\left[1-\left(\dfrac{m}{k_{lm}a}\right)^2\right]\left[J_m\left(k_{lm}a\right)\right]^2\right\}, \\[2mm] \quad (l\in[0,\infty], m\in[1,\infty], n\in[0,\infty] \text{ or } l\in[1,\infty], m\in[0,\infty], n\in[0,\infty])\end{cases} \tag{3.88}$$

where v_m and v_n are defined in Eq. (3.72).

If the cavity fluid loading is neglected, Eq. (3.67) becomes

$$\ddot{W}_{oq}(t) + 2\boldsymbol{x}_{oq}^s \boldsymbol{w}_{oq}^s \dot{W}_{oq}(t) + (\boldsymbol{w}_{oq}^s)^2 W_{oq}(t) = \frac{p_{oq}(t)}{\mathrm{M}_{oq}} . \tag{3.89}$$

Because all time dependent variables are assumed to be time harmonic, we have

$$W_{oq}(t) = e^{j\boldsymbol{w}t} W_{oq} , \tag{3.90}$$

$$P_{lmn}(t) = e^{j\boldsymbol{w}t} P_{lmn} . \tag{3.91}$$

Considering Eqs. (3.90) and (3.91), and solving Eqs. (3.86) and (3.89) for the modal pressure distribution $P_{lmn}(t)$, and using Eq. (3.70), yields

$$P_{lmn}(t) = P_i e^{j\boldsymbol{w}t} \frac{F_{lmn}(\boldsymbol{w})}{\left[-\boldsymbol{w}^2 + j2\boldsymbol{x}_{lmn}^f \boldsymbol{w}_{lmn}^f \boldsymbol{w} + (\boldsymbol{w}_{lmn}^f)^2\right]\Lambda_{lmn}} , \tag{3.92}$$

where

$$F_{lmn}(\boldsymbol{w}) = \boldsymbol{r}_2 c_2^2 S \sum_{o=0,q=1}^{\infty} \frac{E_{oq} D_{oqlmn}}{\left\{\left[\left(\frac{\boldsymbol{w}_{oq}^s}{\boldsymbol{w}}\right)^2 - 1\right] + j2\boldsymbol{x}_{oq}^s \frac{\boldsymbol{w}_{oq}^s}{\boldsymbol{w}}\right\}\mathrm{M}_{oq}} . \tag{3.93}$$

Using Eq. (3.76), Eq. (3.93) can be re-written as

$$F_{lmn}(\boldsymbol{w}) = \sum_{o=0,q=1}^{\infty} (-j)^o \Pi_{oqlmn}\left(Q_{oq}^R + jQ_{oq}^I\right), \tag{3.94}$$

where

$$\Pi_{oqlmn} = \frac{\boldsymbol{r}_2 c_2^2 S D_{oqlmn}}{\left\{\left[\left(\frac{\boldsymbol{w}_{oq}^s}{\boldsymbol{w}}\right)^2 - 1\right]^2 + \left(2\boldsymbol{x}_{oq}^s \frac{\boldsymbol{w}_{oq}^s}{\boldsymbol{w}}\right)^2\right\}\mathrm{M}_{oq}} , \tag{3.95}$$

$$Q_{oq}^R = \left[\left(\frac{\boldsymbol{w}_{oq}^s}{\boldsymbol{w}}\right)^2 - 1\right]V_{oq}^R + 2\boldsymbol{x}_{oq}^s \frac{\boldsymbol{w}_{oq}^s}{\boldsymbol{w}}V_{oq}^I , \tag{3.96}$$

45

$$Q_{oq}^I = \left[\left(\frac{w_{oq}^s}{w} \right)^2 - 1 \right] V_{oq}^I - 2x_{oq}^s \frac{w_{oq}^s}{w} V_{oq}^R, \tag{3.97}$$

where V^R and V^I are obtained from Eqs. (3.77) and (3.78). F_{lmn} is divided into a real part F_{lmn}^R and an imaginary part F_{lmn}^I like

$$F_{lmn}(w) = F_{lmn}^R(w) + jF_{lmn}^I(w), \tag{3.98}$$

where

$$F_{lmn}^R(w) = \sum_{o=0,q=1}^{\infty} (-1)^o \left[\Pi_{(2o)q,lmn} Q_{(2o)q}^R + \Pi_{(2o+1)q\,lmn} Q_{(2o+1)q}^I \right], \tag{3.99}$$

$$F_{lmn}^I(w) = \sum_{o=0,q=1}^{\infty} (-1)^o \left[\Pi_{(2o)q,lmn} Q_{(2o)q}^I - \Pi_{(2o+1)q\,lmn} Q_{(2o+1)q}^R \right]. \tag{3.100}$$

Therefore, substituting Eq. (3.98) into Eq. (3.92), and re-arranging, yields

$$p_{lmn}(t) = P_i e^{jwt} \left[G_{lmn}^R + jG_{lmn}^I \right], \tag{3.101}$$

where

$$G_{lmn}^R = \frac{F_{lmn}^R \left[\left(w_{lmn}^f \right)^2 - w^2 \right] + F_{lmn}^I \left(2x_{lmn}^f w_{lmn}^f w \right)}{\left\{ \left[\left(w_{lmn}^f \right)^2 - w^2 \right]^2 + \left(2x_{lmn}^f w_{lmn}^f w \right)^2 \right\} \Lambda_{lmn}}, \tag{3.102}$$

$$G_{lmn}^I = \frac{F_{lmn}^I \left[\left(w_{lmn}^f \right)^2 - w^2 \right] - F_{lmn}^R \left(2x_{lmn}^f w_{lmn}^f w \right)}{\left\{ \left[\left(w_{lmn}^f \right)^2 - w^2 \right]^2 + \left(2x_{lmn}^f w_{lmn}^f w \right)^2 \right\} \Lambda_{lmn}}. \tag{3.103}$$

Substituting Eq. (3.92) into Eq. (3.82), the internal pressure field is

$$p_{int}(r,\boldsymbol{f},z,t) = P_i e^{jwt} \sum_{l,m\;n=0}^{\infty} \frac{F_{lmn}(\boldsymbol{w})}{\left[-\boldsymbol{w}^2 + j2\boldsymbol{x}_{lmn}^f \boldsymbol{w}_{lmn}^f \boldsymbol{w} + (\boldsymbol{w}_{lmn}^f)^2\right]\Lambda_{lmn}} \Psi_{lmn}(r,\boldsymbol{f},z), \qquad (3.104)$$

where again l, m, n, cannot be equal to zero at the same time because the $(0,0,0)$ mode is not considered. The structural damping $\boldsymbol{x}^s$ and fluid medium damping $\boldsymbol{x}^f$ can be determined by experimental modal identification. Using Eq. (3.101), Eq. (3.104) is also re-written as

$$p_{int}(r,\boldsymbol{f},z,t) = P_i e^{jwt} \sum_{l,m\;n=0}^{\infty} \left[G_{lmn}^R + jG_{lmn}^I\right]\Psi_{lmn}(r,\boldsymbol{f},z). \qquad (3.105)$$

Eqs. (3.60) and (3.105) are used in the calculation of noise reduction spectrum in the next section.

3.5   Noise Reduction Spectrum

The definition of transmission loss for an infinite flat panel assumed that the transmitted sound was totally absorbed, and only inward-propagating waves existed. However, the problems under consideration differ from an infinite flat panel, not only because of its finite dimension, but also because of the internal cavity resonances in the closed cylindrical shell. It is not possible to define a transmission loss like is done for flat panels. For measurement of the sound transmission through cylindrical shells, Holmer and Heymann [67] defined the sound power transmission coefficient to be equal to the ratio of power radiated per unit surface area of the shell to the power passing axially through a unit area of cross section. In other references [18-22, 41], researchers suggested using the noise reduction (NR) instead of calculating transmission loss, which was based on the ratio of inner and outer time- and space-averaged mean-square pressures. In this study, a theoretical method to characterize broadband sound transmission into a finite cylindrical structure is defined based on NR. It is called noise reduction spectrum (NRS), which is computed from

$$NRS = -10\log_{10} \frac{< p_{int}^2 >}{< p_{ext}^2 >},\tag{3.106}$$

where $< p_{ext}^2(\boldsymbol{w}) >$ is the mean-square external pressure averaged over the outside shell surface S and time length T. It is

$$\left\langle p_{ext}^2 \right\rangle = P_i^2 \sum_{m=0}^{\infty} \boldsymbol{e}_m \left| J_m(k_{1r}a) + C_m H_m^{(2)}(k_{1r}a) \right|^2.\tag{3.107}$$

$< p_{int}^2 >$ is the mean-square internal pressure averaged over the inside shell surface S and time length T. It is

$$\left\langle p_{int}^2 \right\rangle = \frac{1}{S} P_i^2 \int_S \left\{ \underbrace{\sum_{l,m,n=0}^{\infty} \left[\left(G_{lmn}^R\right)^2 + \left(G_{lmn}^I\right)^2 \right] \Psi_{lmn}^2}_{Term1} + \underbrace{\sum_{\substack{l,m,n,o,=0 \\ o \neq l}}^{\infty} \left[G_{lmn}^R G_{omn}^R + G_{lmn}^I G_{omn}^I \right] \Psi_{lmn} \Psi_{omn}}_{Term2} \right\} dS,\tag{3.108}$$

where G^R and G^I are given by Eqs. (3.102) and (3.103). Ψ_{lmn} are the mode shapes of the acoustic cavity, and given by Eq. (3.83). l, m and n are the number of radial nodes, diametric nodes and longitudinal nodes in acoustic cavity mode shapes, and o is the number of circumferential waves in structural mode shapes. The integration of the *Term 1* over the interior surface yields:

$$\int_S \sum_{l,m,n=0}^{\infty} \left[\left(G_{lmn}^R\right)^2 + \left(G_{lmn}^I\right)^2 \right] \Psi_{lmn}^2 dS =$$

$$aL\boldsymbol{p} \sum_{n=1}^{\infty} \left[\left(G_{00n}^R\right)^2 + \left(G_{00n}^I\right)^2 \right]$$

$$+ \frac{1}{2} aL\boldsymbol{p} \sum_{l=0,m=1,n=0}^{\infty} v_n \left[\left(G_{lmn}^R\right)^2 + \left(G_{lmn}^I\right)^2 \right] J_m^2(k_{lm}a)$$

$$+ \frac{1}{2} aL\boldsymbol{p} \sum_{l=1,m=0,n=0}^{\infty} v_m v_n \left[\left(G_{lmn}^R\right)^2 + \left(G_{lmn}^I\right)^2 \right] J_m^2(k_{lm}a)$$

.\tag{3.109}

The integration of the *Term 2* over the interior surface yields:

$$\int_S \sum_{\substack{l,m,\,n,\,o,\,=0 \\ o \neq l}}^{\infty} \left(G_{lmn}^R G_{omn}^R + G_{lmn}^I G_{omn}^I \right) \Psi_{lmn} \Psi_{omn} \, dS =$$

$$aL\boldsymbol{p} \sum_{n,o=1}^{\infty} \left(G_{00n}^R G_{o0n}^R + G_{00n}^I G_{o0n}^I \right) J_m(k_{om}a)$$

$$+\frac{1}{2} aL\boldsymbol{p} \sum_{\substack{l=0,m=1,n=0 \\ o=0,\,o \neq l}}^{\infty} v_n \left(G_{lmn}^R G_{omn}^R + G_{lmn}^I G_{omn}^I \right) J_m(k_{lm}a) J_m(k_{om}a) \qquad (3.110)$$

$$+\frac{1}{2} aL\boldsymbol{p} \sum_{\substack{l=1,m=0,n=0 \\ o=0,\,o \neq l}}^{\infty} v_m v_n \left(G_{lmn}^R G_{omn}^R + G_{lmn}^I G_{omn}^I \right) J_m(k_{lm}a) J_m(k_{om}a)$$

Substituting Eqs. (3.109) and (3.110) into (3.108), yields

$$\left\langle p_{int}^2 \right\rangle = P_i^2 \Theta, \qquad (3.111)$$

where

$$\Theta = \frac{1}{2} \sum_{n=1}^{\infty} \left[\left(G_{00n}^R \right)^2 + \left(G_{00n}^I \right)^2 \right] + \frac{1}{4} \sum_{l=0,m=1,n=0}^{\infty} v_n \left[\left(G_{lmn}^R \right)^2 + \left(G_{lmn}^I \right)^2 \right] J_m^2(k_{lm}a)$$

$$+\frac{1}{4} \sum_{l=1,m=0,n=0}^{\infty} v_m v_n \left[\left(G_{lmn}^R \right)^2 + \left(G_{lmn}^I \right)^2 \right] J_m^2(k_{lm}a)$$

$$+\frac{1}{2} \sum_{n,o=1}^{\infty} \left(G_{00n}^R G_{o0n}^R + G_{00n}^I G_{o0n}^I \right) J_m(k_{om}a) \qquad , \qquad (3.112)$$

$$+\frac{1}{4} \sum_{\substack{l=0,m=1,n=0 \\ o=0,\,o \neq l}}^{\infty} v_n \left(G_{lmn}^R G_{omn}^R + G_{lmn}^I G_{omn}^I \right) J_m(k_{lm}a) J_m(k_{om}a)$$

$$+\frac{1}{4} \sum_{\substack{l=1,m=0,n=0 \\ o=0,\,o \neq l}}^{\infty} v_m v_n \left(G_{lmn}^R G_{omn}^R + G_{lmn}^I G_{omn}^I \right) J_m(k_{lm}a) J_m(k_{om}a)$$

where v_m and v_n are defined in Eq. (3.72), G^R and G^I are computed from Eqs. (3.102) and (3.103), l, m and n are the number of radial nodes, diametric nodes and longitudinal nodes in acoustic cavity mode shapes, and o is the number of circumferential waves in structural mode shapes.

Substituting Eqs (3.107), and (3.111) into Eq. (3.106), the analytical formula for the calculation of noise reduction spectrum is obtained as

$$NRS = 10\log_{10} \frac{\sum_{m=0}^{\infty} e_m \left| J_m(k_{1r}a) + C_m H_m^{(2)}(k_{1r}a) \right|^2}{\Theta} . \tag{3.113}$$

The NRS is only a function of frequency since the time variable is cancelled during the calculation. In Eq. (3.113), J_m is the Bessel function of the first kind of integer order m^{th}, and $H_m^{(2)}$ is the Hankel function of the second kind of integer order m^{th}, k_{1r} is the radial component of the wavenumber given by Eq. (3.13), and a is the radius of the midsurface. The coefficient C_m is given by Eq. (3.56), and Θ is given by Eq. (3.112).

3.6   Application

Numerical results from Eq. (3.113) have been generated for the ChamberCore composite cylindrical shell with radius $a = 255$ mm and effective thickness $h = 20.1$ mm. The physical parameters of the composite material are: Young's modulus $E = 60$ GPa, Poisson's ratio $m = 0.3$, effective density of the uniform shell is $r_s = 315$ kg/m^3. The speed of sound and the density of air inside and outside the cylindrical shell are $c_1 = c_2 = 346$ m/s (75° F) and $r_1 = r_2 = 1.21$ kg/m^3. The oblique incident plane wave is given by Eq. (3.12), where $q = 30$ degrees and $P_i = 100$ Pa. In order to simplify analysis, the acoustic damping ratio was set to the same value for all modes and obtained by averaging the measured results (0.28%). The structural damping ratio was also set to the same for all modes and obtained by averaging the measurement identification results obtained from measurements (4.64%).
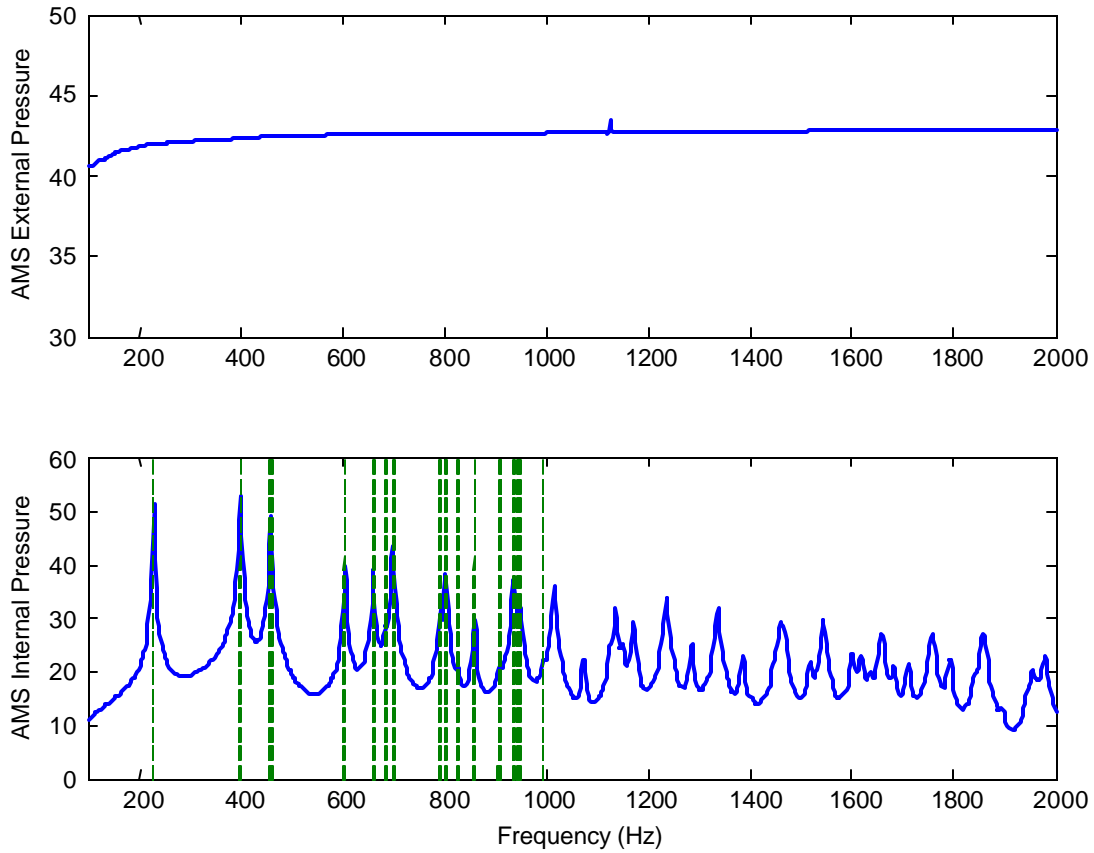
Figure 3.4 Averaged Mean-Square Exterior and Interior Pressure.

Figure 3.4 shows the spectrum of the mean-square external pressure averaged over the outside shell surface, given by Eq. (3.107), and the spectrum of the mean-square internal pressure averaged over the inside shell surface, given by Eq. (3.111). The cavity resonances between [0, 1000] Hz are indicated in the figure by vertical dashed lines. Inspecting Figure 3.4 it is observed that there are peaks in the spectrum curve of the internal averaged mean-square pressure corresponding to nearly every acoustic and structural resonance.

Figure 3.5 and Figure 3.6 show the curves of the noise reduction spectrum, given by Eq. (3.113), with a different frequency range and different *x*-axis scale method. The acoustic cavity resonances between [0, 1000] Hz are shown in the plots as dashed vertical lines, and the predicted structural resonances are larger than 1000 Hz and not shown in the figure.
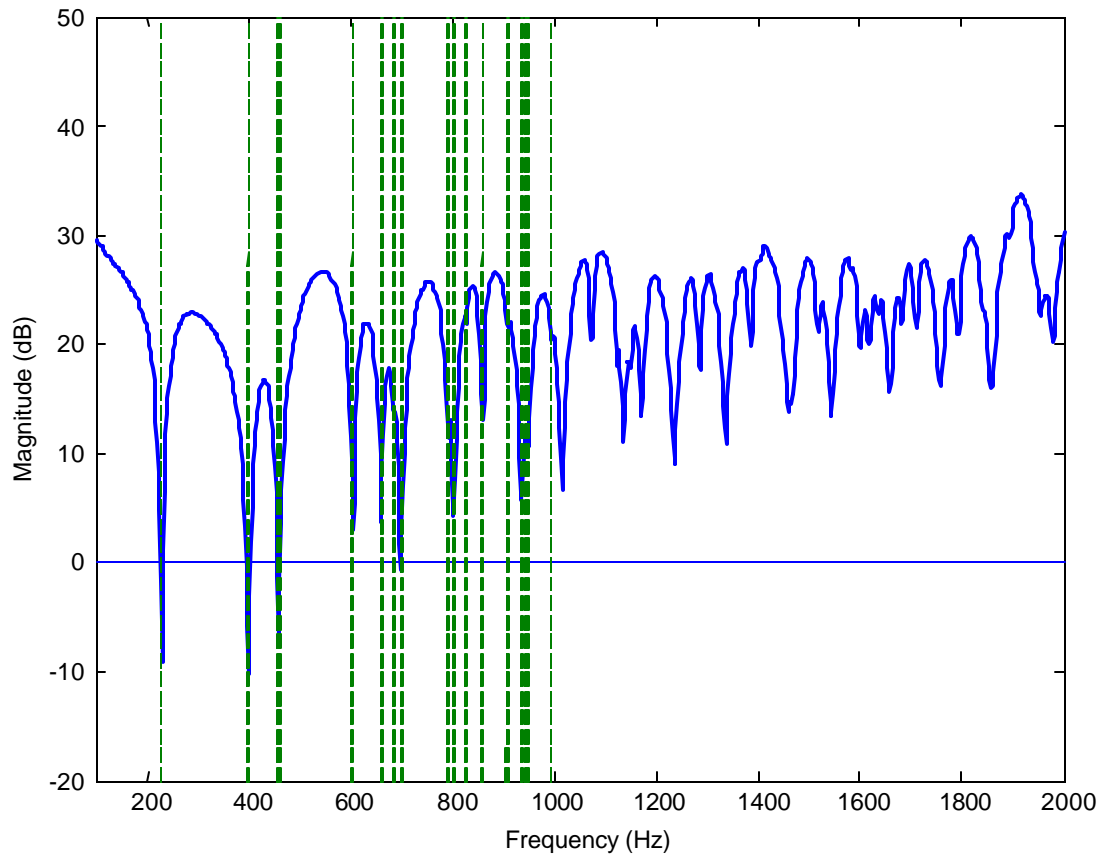
Figure 3.5 Theoretical NRS of the ChamberCore Cylindrical Fairing (1)

The principal result of this study is Figure 3.5 and it shows the effect on the noise reduction spectrum of interior acoustic cavity resonances. There is a sharp dip at almost all of the cavity resonances. The cavity resonances significantly reduce the noise reduction capability of the finite cylindrical structure causing amplification (negative NRS, also see Figure 3.5) at 228 Hz, 398 Hz, 455 Hz, 458 Hz, and 698 Hz. There are also dips corresponding to structural resonances. However, in the low frequency band, because the density of cavity acoustic resonances is much larger than that of the structural resonances (see Figure 3.5), the noise reduction spectrum is dominated by the cavity resonances here.
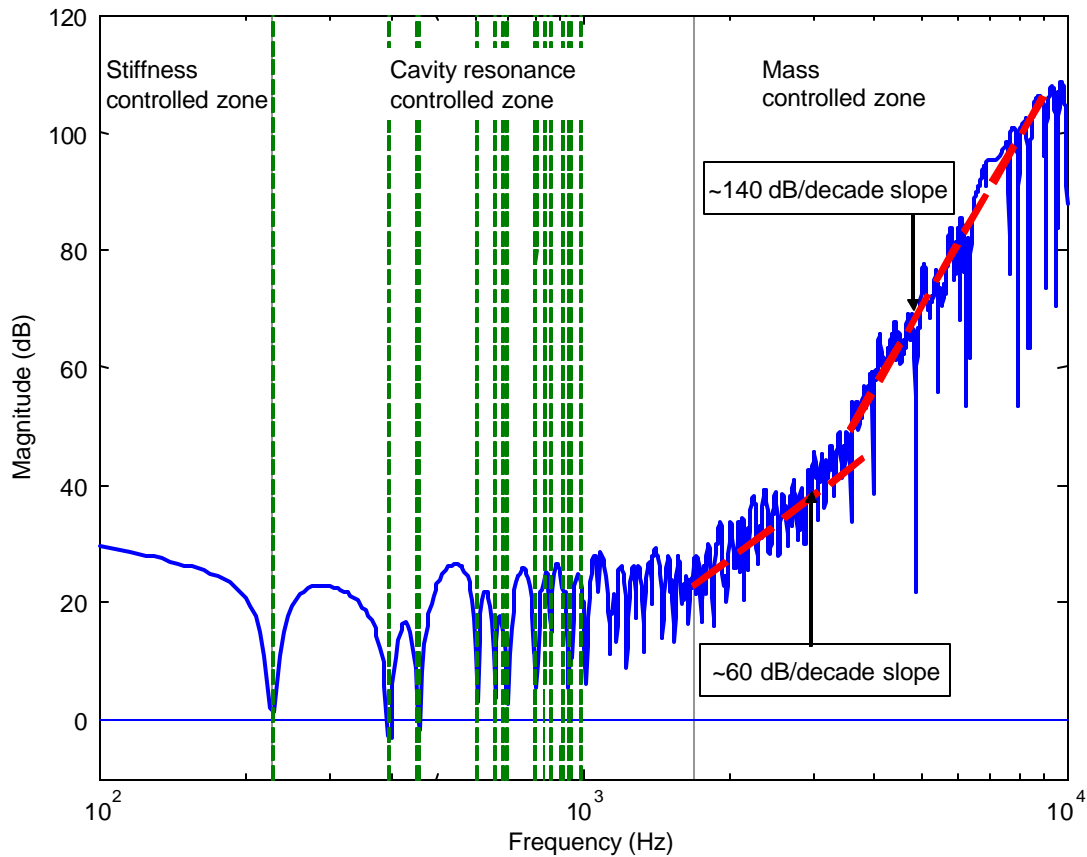
Figure 3.6 Theoretical NRS of the ChamberCore Cylindrical Fairing (2)

Figure 3.6 is the NRS curve with logarithmic x-axis. From Figure 3.6 it is observed that as the frequency increases, there is a trend developing that is similar to mass-law behavior where the NRS is increasing by 55 dB per decade as indicated by the oblique dashed line at the right side in Figure 3.6, even though there still is wide fluctuation in the NRS curve.

Figure 3.7 shows the effects on NRS of internal acoustic damping. The solid curve is the NRS curve of the ChamberCore fairing with general acoustic damping, and the dashed curve is the NRS curve of the ChamberCore fairing with a ten-times increase in the general acoustic damping. The cavity acoustic resonances between 0 to 1000 Hz are also indicated in the figure as vertical dashed lines. From Figure 3.7 it can be observed that when increasing the internal acoustic damping the noise reduction spectrum obtains significant improvement at almost every acoustic resonance. There are about 20 dB, 21 dB, 21 dB and 21 dB improvement in (001) mode

at 228 Hz, (010) mode at 398 Hz, (002) mode at 452 Hz, and (011) mode at 458 Hz, respectively, when acoustic damping is increased 10 times.
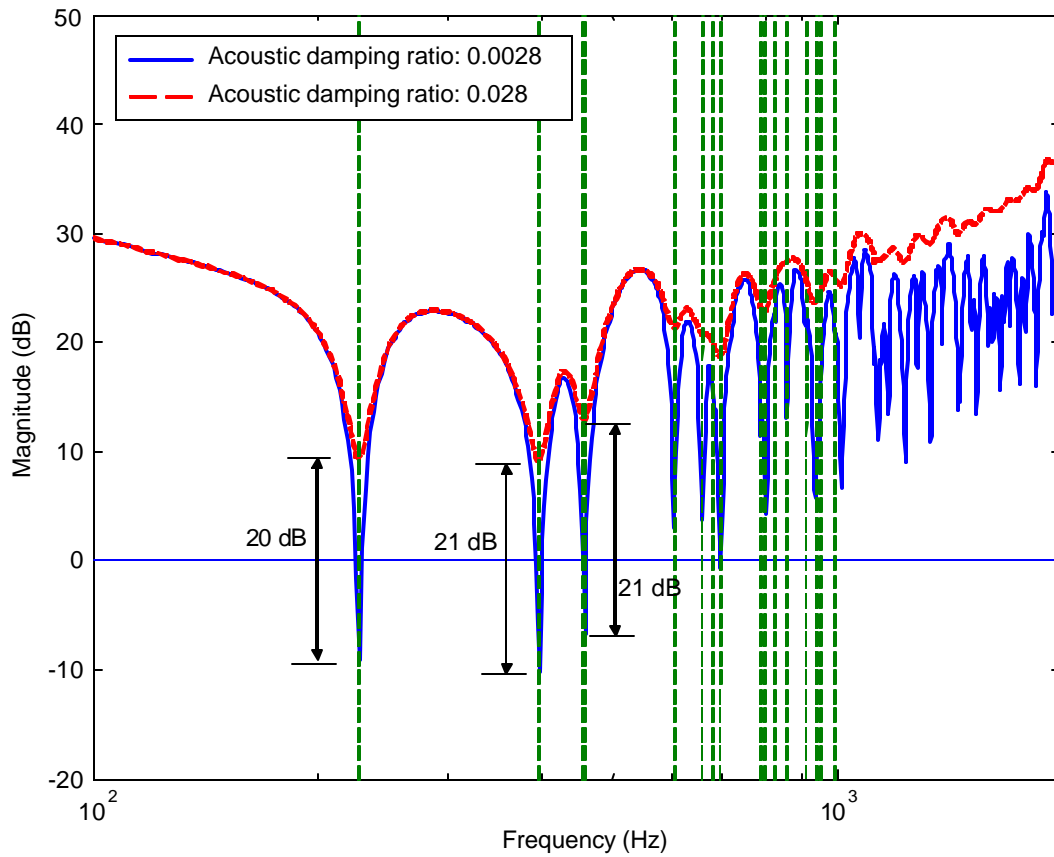
Figure 3.7 Theoretical NRS of the ChamberCore Cylindrical Fairing (3)

3.7   Conclusions

An effective uniform shell model of the ChamberCore cylindrical shell was developed. The analytical formulas for calculating the near field pressure of an infinite elastic cylindrical shell was derived and the analytical formulas for calculating the interior pressure distribution of a finite cylindrical structure was also derived. The theoretical noise

reduction spectrum (NRS) model for analytically characterizing noise transmission into a finite elastic cylindrical structure was defined and developed. An application for the ChamberCore composite fairing was studied with the theoretical NRS model. The numerical results show that the cavity resonances have a significant effect on the noise transmission into the finite cylindrical structure. At the part of high frequency band the noise reduction spectrum curve follows the mass-law behavior. The internal acoustic damping can significantly influence the noise transmission into the finite cylindrical structure.

4.0 NUMERICAL ANALYTICAL AND EXPERIMENTAL CHARACTERIZATION

Experimental studies of the structural and acoustic vibration and sound transmission can not only help one to understand the vibroacoustic behavior of the cylindrical structures, but also provide an opportunity to validate the theoretical results which have been obtained in Chapter 3.0. In this chapter, two different advanced composite structures: a mock-scale tapered cylindrical AGS composite fairing and a mock-scale cylindrical ChamberCore fairing are under study, which are supplied by the Air Force Research Laboratory's Space Vehicles Directorate (AFRL/VS). Firstly, a new modal parameter extraction method, called "state-space realization based modal parameter identification method," is presented. Then, the dynamic parameters of both structures and acoustic cavities are obtained with a combination of numerical, analytical and experimental approaches. Finally, an *in-situ* version of the noise reduction spectrum is developed to experimentally characterize the noise transmission into the two fairings.

4.1   Theory and Algorithms of the Structural Modal Identification

The state-space model identified from measured data has received considerable application in the modern controls field, especially in flexible structure control and structure- or air-borne noise control. Numerous algorithms for both the time and frequency domain realization of a state-space model have been presented in the literature. Ho and Kalman [50] proposed an important algorithm for state realization in the time domain, in which the Hankel matrix of system Markov parameters was used to construct a minimal state realization of a linear time-invariant (LTI) system. Zeiger and McEwen [51], and Kung [52] extended the Ho-Kalman algorithm in combination with the singular value decomposition (SVD) technique to reduce the order of the state-space model and improve the algorithm accuracy. Juang and Pappa [53] proposed the eigensystem realization algorithm (ERA) for modal parameter identification, which is also based on the Ho-Kalman algorithm, and combines the SVD technique to obtain a

minimum order state-space realization. Juang and Cooper [54] extended the approach to the eigensystem realization algorithm using data correlation (ERA/CD).

The canonical correlation algorithm has been used in stochastic identification problems for model construction [55-57]. Mullis and Roberts [58], and Inouye [59] applied the Markov parameters and covariance parameters to realize a state-space model. King, Desai, and Skelton [60] used the first q-Markov parameters and output covariance parameters in a generalized algorithm for state realization that is called "Q-Markov covariance (Q-Markov Cover) equivalent realization".

Liu [61] proposed a new state realization algorithm, observability range space extraction (ORSE), which was based on the SVD and generalized the ERA and the Q-Markov Cover. Later Liu, Jacques, and Miller [62] extended the concepts of the ORSE to the frequency domain, and presented another algorithm, FORSE.

4.1.1   Introduction to the ORSE Algorithm

Assume a linear time-invariant, controllable, and observable system to be identified. The discrete state-space representation of this system is:

$$\begin{cases} x(k+1) = Ax(k) + Bu(k) \\ y(k) \quad = Cx(k) + Du(k) \end{cases}.$$

(4.1)

The frequency response function can be described as:

$$G(e^{jwT}) = C(e^{jwT}I - A)^{-1}B + D,$$

(4.2)

where $x(k) \in \Re^{n_x}$ is the state vector, $y(k) \in \Re^{n_y}$ is the output vector, and $u(k) \in \Re^{n_u}$ is the input vector. $\Re^n$ represents n-dimension real vector space. A, B, C, and D are the state matrix, input influence matrix, output influence matrix, and feedthrough matrix, respectively, and will be discussed later.

In the discrete time domain, the matrix $u_q(k)$ consisted of q-input vectors and the corresponding matrix $y_q(k)$ consisted of q-output vectors are presented as:

$$u_q(k) = \begin{bmatrix} u(k) \\ u(k+1) \\ u(k+2) \\ \vdots \\ u(k+(q-1)) \end{bmatrix}, \qquad (4.3)$$

$$y_q(k) = \begin{bmatrix} y(k) \\ y(k+1) \\ y(k+2) \\ \vdots \\ y(k+(q-1)) \end{bmatrix}. \qquad (4.4)$$

From Eqs. (4.1), (4.3) and (4.4), the following equation can be obtained

$$y_q(k) = O_q x(k) + H_q u_q(k), \qquad (4.5)$$

where O_q and H_q are defined by:

$$O_q = \begin{bmatrix} C \\ CA \\ \vdots \\ CA^{(q-1)} \end{bmatrix}, \qquad (4.6)$$

and

$$H_q = \begin{bmatrix} D & 0 & \cdots & 0 \\ CB & D & \cdots & 0 \\ \vdots & \vdots & \ddots & \vdots \\ CA^{(q-2)}B & CA^{(q-3)}B & \cdots & D \end{bmatrix}. \qquad (4.7)$$

58

The matrix O_q is known as the observability matrix. If a basis for this matrix can be found, then a realization for the A and C matrices can be computed. Assuming the record length of each sample is K, the following matrices are constructed:

$$U \equiv [u_q(1) \ u_q(2) \cdots u_q(K)],$$

(4.8)

$$X \equiv [x_q(1) \ x_q(2) \cdots x_q(K)],$$

(4.9)

$$Y \equiv [y_q(1) \ y_q(2) \cdots y_q(K)],$$

(4.10)

$$M \equiv \text{Re}(YY^H) - \text{Re}(YU^H)\text{Re}(UU^H)^+ \text{Re}(UU^H),$$

(4.11)

where "Re" means the real part of the complex number or matrix, "H" denotes the complex conjugate transpose, and "+" denotes the Moore-Penrose pseudo-inverse.

Jacques [63] proved that the matrix M had the same basis as O_q if the following conditions are satisfied: (1) $K/2 > q$; (2) the frequency response of the states measured at the sample frequencies are linearly independent; (3) the frequency response for each state varies over the sample frequencies; and (4) the system is stable. The singular value decomposition of M is

$$M = V \sum V^H,$$

(4.12)

where $V \in \Re^{m \times n}$ ($m = qn_y$) is a column unitary matrix, and n_y is the number of outputs, q is the number of output vectors, n is the rank of matrix Σ, which is a diagonal matrix of singular values that are greater than zero, and $V^H V = I$. The A and C matrices for a state realization of the discrete system can be found from V:

$$V = \begin{bmatrix} V_1 \\ V_2 \\ V_3 \end{bmatrix},$$

(4.13)

$$A = \begin{bmatrix} V_1 \\ V_2 \end{bmatrix}^{+} \begin{bmatrix} V_2 \\ V_3 \end{bmatrix} , \tag{4.14}$$

$$C = V_1 , \tag{4.15}$$

where V_1 includes the first n_y rows of V, and V_3 includes the last n_y rows of V. When the A and C matrices are known, the transfer function is linear in the B and D matrices (see Eq.(4.2)), and they can be solved by the linear least square method (LSM):

$$(B,D) = \underset{B,D}{\arg\min} \left\| \begin{bmatrix} C(Ie^{jw_1 T} - A)^{-1} & I \\ C(Ie^{jw_2 T} - A)^{-1} & I \\ \vdots & \vdots \\ C(Ie^{jw_N T} - A)^{-1} & I \end{bmatrix} \begin{bmatrix} B \\ D \end{bmatrix} - \begin{bmatrix} G(e^{jw_1 T}) \\ G(e^{jw_2 T}) \\ \vdots \\ G(e^{jw_N T}) \end{bmatrix} \right\|^2 . \tag{4.16}$$

4.1.2   Modal Parameter Extraction from the Pole-Residue Model of FRF

Assume an N-DOF system with mass, stiffness, and damping matrices M, C, and K, and displacement vector y. The equation of motion for the system can be represented by the following:

$$M\ddot{y} + C\dot{y} + Ky = f(t) . \tag{4.17}$$

The transfer function of the structural system can be presented as the following rational polynomial in the s domain,

$$H_{ij}(s) = \frac{Y_i(s)}{F_j(s)} = \frac{a_0 + a_1 s + a_2 s^2 + \cdots + a_m s^m}{1 + b_1 s + b_2 s^2 + \cdots + b_n s^n} = \frac{N_{ij}(s)}{D(s)} , \tag{4.18}$$

where $Y_i(s)$ is the displacement in the ith point, and $F_j(s)$ is the force acting at the jth point, $m=2(N-1)$, and $n=2N$. From structural dynamics, we can obtain the pole-residue presentation of the transfer function as:

$$H_{ij}(s) = \sum_{r=1}^{N} \left(\frac{A_{rij}}{s - s_r} + \frac{A^*_{rij}}{s - s^*_r} \right). \tag{4.19}$$

The term in the parentheses on the right hand side of Eq. (4.19) can be represented as

$$H_{rij} = \frac{A_{rij}}{s - s_r} + \frac{A^*_{rij}}{s - s^*_r}, \tag{4.20}$$

where H_{rij} is the contribution of rth mode to H_{ij}, $s_r = -\mathbf{s}_r + jv_r$, and $s^*_r = -\mathbf{s}_r - jv_r$ are the rth conjugate pole pair of H_{ij}, and A_{rij} is the rth residue of H_{ij} which can be calculated by:

$$A_{rij} = H_{ij}(s - s_r)|_{s=s_r} = \left. \frac{N_{ij}(s)}{D'(s)} \right|_{s=s_r}. \tag{4.21}$$

Eq. (4.19) is simplified as:

$$H_{ij}(s) = \sum_{r=1}^{N} H_{rij}. \tag{4.22}$$

The relation between the pole-residue parameters and the modal parameters is as follows:

$$A_{rij} = \frac{\mathbf{y}_{ri}\mathbf{y}_{rj}}{a_r}, \tag{4.23}$$

$$A^*_{rij} = \frac{\mathbf{y}^*_{ri}\mathbf{y}^*_{rj}}{a_r}, \tag{4.24}$$

where $a_r = \mathbf{y}^H_r(2s_r M + C)\mathbf{y}_r$. If the damping can be uncoupled, a simple formula can be used to calculate a_r and poles as follows:

$$a_r = -j2w_{dr}m_r, \tag{4.25}$$

$$s_r = -w_r x_r + jw_{dr}, \tag{4.26}$$

$$s_r^* = -w_r x_r - jw_{dr}, \tag{4.27}$$

where $w_{dr} = w_r \sqrt{1 - x_r^2}$ is the damped natural frequency. Using the above theory, and curve fitting the measured transfer functions, the residues, poles, and ultimately the natural frequencies, damping ratios, and mode shapes can be calculated as follows:

$$w_{dr} = \text{Im}(s_r), \tag{4.28}$$

$$x_r = \cos\left[\arctan\left(\frac{\text{Im}(s_r)}{\text{Re}(s_r)}\right)\right], \tag{4.29}$$

$$y_{ri} = \frac{A_{rij}}{A_{rjj}} y_{rj}. \tag{4.30}$$

4.1.3 Simplification of Mode Shape Extraction for Lightly Damped Systems

A simple realization for mode shape identification can be derived if the damping ratios are small (<1%). Assuming there are only real mode shapes, the residues are purely imaginary, $A_{rij} = jV_{rij}$ and $A_{rij}^* = -jV_{rij}$. Substituting Eqs. (4.23), (4.24), (4.25), (4.26), and (4.27) into Eq. (4.20), and setting $s = jw$, the new representation of H_{rij} is

$$H_{rij}(w) = \frac{-2V_{rij}w_r\sqrt{1 - x_r^2}}{w_r^2 - w^2 - i2x_r w_r w}. \tag{4.31}$$

At resonance (i.e. $w = w_{dr}$), Eq.(4.22) can be approximated for lightly coupled systems as:

$$H_{ij}(\boldsymbol{w}_{dr}) = \sum_{r=1}^{N} H_{rij}(\boldsymbol{w}_{dr}) \approx H_{rij}(\boldsymbol{w}_{dr}) .$$

(4.32)

Since damping is assumed to be small, $\boldsymbol{w} = \boldsymbol{w}_{d\,r} = \boldsymbol{w}_r \sqrt{1 - \boldsymbol{x}_r^2} \approx \boldsymbol{w}_r$, therefore,

$$H_{ij}(\boldsymbol{w}_{dr}) \approx H_{rij}(\boldsymbol{w}_{dr}) \approx \frac{V_{rij}}{j\boldsymbol{x}_r\boldsymbol{w}_r} = -j\frac{V_{rij}}{\boldsymbol{x}_r\boldsymbol{w}_r} .$$

(4.33)

$H_{rij}(\boldsymbol{w}_{dr})$ is nearly purely imaginary value, and the residue is approximated as:

$$A_{rij} = jV_{rij} \approx -\operatorname{Im}[H_{ij}(\boldsymbol{w}_{dr})]\boldsymbol{x}_r\boldsymbol{w}_r .$$

(4.34)

Therefore, from Eq. (4.30) and (4.34) the mode shapes can be found from:

$$\boldsymbol{y}_{ri} = \frac{\operatorname{Im}[H_{rij}(\boldsymbol{w}_{dr})]}{\operatorname{Im}[H_{rjj}(\boldsymbol{w}_{dr})]}\boldsymbol{y}_{rj} .$$

(4.35)

4.1.4   State-Space Realization-Based Modal Parameter Extraction

In the field of control, the equations of motion of a linear, time-invariant multiple degree of freedom structural system can be presented as:

$$M\,\ddot{y}(t) + C\,\dot{y}(t) + K\,y(t) = F\,u(t) ,$$

(4.36)

where $u(t)$ is the vector of actuator inputs, $y(t)$ is the vector of sensor outputs, and M, C, K, and F are the mass, damping, stiffness, and force matrices, respectively. The MDOF system can also be represented with continuous time state-space equations:

$$\begin{cases} \dot{x}(t) = Ax(t) + Bu(t) \\ y(t) = Cx(t) + Du(t) \end{cases} ,$$

(4.37)

where $x(t)$ is the state vector, with $y(t)$ and $u(t)$ having the same meaning as those in Eq. (4.36). The state matrix, A, input influence matrix, B, output influence matrix, C, and feedthrough matrix, D, are defined as

$$A = \begin{bmatrix} -M^{-1}C & -M^{-1}K \\ I & 0 \end{bmatrix}, \quad B = \begin{bmatrix} -M^{-1}F \\ 0 \end{bmatrix}, \quad C = \begin{bmatrix} 0 & I \end{bmatrix}, \quad D = \begin{bmatrix} 0 \end{bmatrix}.$$

The state-space equations for the free vibration system is

$$\begin{cases} \dot{x}(t) = Ax(t) \\ y(t) = Cx(t) \end{cases}. \tag{4.38}$$

The solution of the first equation of Eq. (4.38), $\dot{x}(t) = Ax(t)$, is an eigenvalue problem. The eigenvalues of matrix A are $s_r = -w_r x_r + jw_{dr}$, $s_r^* = -w_r x_r - jw_{dr}$ (where $w_{dr} = w_r \sqrt{1 - x_r^2}$, and $r = 1, 2, \cdots N$), and eigenvector matrix is Φ. The damped natural frequency and damping ratios can be calculated using Eq. (4.28) and (4.29), respectively. Finally, the mode shape matrix of the structural system can be solved as:

$$\Psi = C\Phi. \tag{4.39}$$

This method uses knowledge of the relationship between structural dynamics and modern control theory to perform modal analysis. First, the state-space model of a structural system will be constructed using a state-space realization algorithm in the time domain or frequency domain. Then, the natural frequencies, damping ratios and mode shapes can be extracted by the method mentioned in this section.

Discussions:

(1)   State-space realization-based modal parameter identification method is needed, especially for cylindrical structures. Because of the axisymmetric property of the cylindrical shell, its circumferential modes occur in pairs (rotated 90 degrees, except for the breathing modes that have zero circumferential nodes). A system that has repeated eigenvalues and

independent mode shapes cannot be identified by algorithms that allow only single-input and single-output (SISO) systems [64, 65].

(2)   The calculation of mode shapes in this method does not require driving point FRFs.

4.2   Structural Modal Analysis

The AGS tapered composite fairing and the ChamberCore composite fairing were experimentally investigated for their vibroacoustic behavior. The AGS composite fairing (see Figure 4.1 and Figure 4.2) forms a tapered cylinder that is 1.8 mm thick with end diameters of 610 mm and 380 mm, and a height of 560 mm. Tridirectional internal ribs with a cross section of 1.5x13 mm crisscross at helix angles varying between 6 and 10 degrees as the diameter of fairing decreases. A cylindrical coordinate system is applied as shown in Figure 4.3, and will be used to describe various positions as well as the structural and acoustic modes.

Figure 4.1 Appearance of the Mock-Scale Tapered AGS Fairing
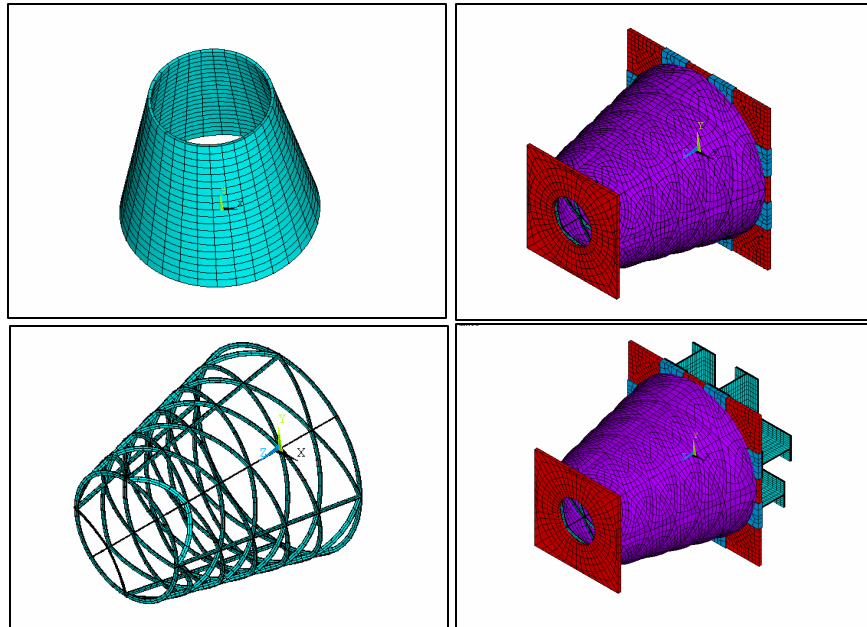
Figure 4.2 FEA Model of the AGS Fairing Showing Construction [35]

$2R_2 = 0.61$m

$2R_1 = 0.38$m

$h = 0.56$m

$\alpha = 11.5$ degrees
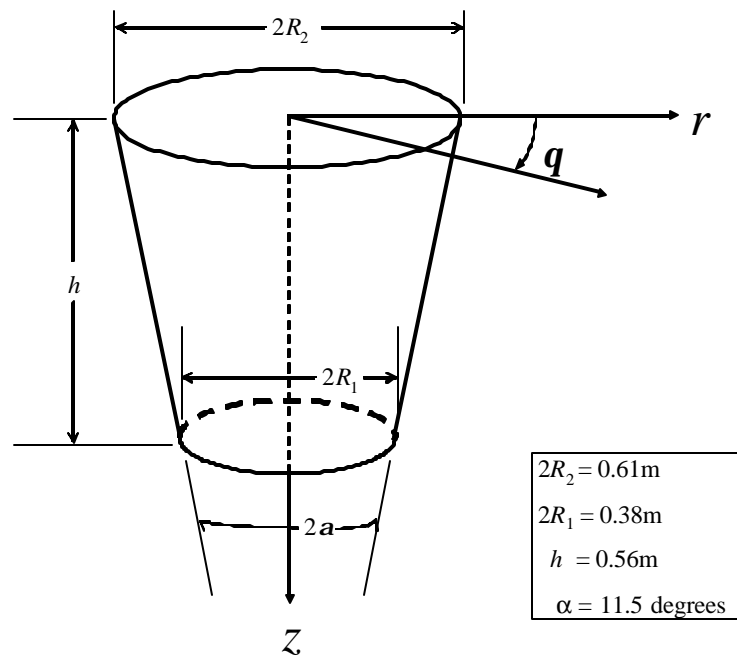
Figure 4.3 AGS Coordinate System

The following subsection outlines the construction of the AGS composite fairing [1-4]. An automated process has been developed for AGS fairings whereby the skin and ribs are created using a 5-axis filament winding process, which requires only a single cure cycle. The relatively simple construction compared to sandwich-type composite structures allows lower cost and better quality results. Type IM7 graphite fiber preimpregnated with 977-2 "Toughened Epoxy" resin was used to create the shell and ribs of the fairing. A volume fraction of approximately 60-65% was resulted. The presence of voids sought to reduce stiffness and increase damping of the structure. The average density of AGS composite material is measured as 1500 kg/m^3, and the theoretical stiffness values for the graphite-epoxy are: E_{11} = 170 GP$_a$, E_{22} = 10 GP$_a$, G_{12} = 5.5 GP$_a$.

Heavy 13 mm thick aluminum plates were installed at the top and bottom of the fairing (as shown in Figure 4.1) in order to approximate clamped, rigid boundary conditions. The larger plate was still found to couple strongly to the interior acoustics and thus a heavy **I**-beam frame was added to make it more "rigid". Modeling of the AGS tapered cylindrical shell is very complex due to the taper along the cylinder axis, the anisotropic properties of the graphite-epoxy material, the inclusion of the internal rib structures, and the dynamic interaction with the "rigid" end caps.

The ChamberCore structure is another advanced composite structure with a sandwich-type. The manufacturing process of the ChamberCore composite structure is shown in the sequence of Figure 4.4, which is a diagram taken from the patent [32]. The interior layer (upper left of Figure 4.4) is a fiber cylinder that was fabricated by filament-wound graphite fiber. The previously fabricated wedge-cross-section tubes were sectioned and subsequently co-cured with an inner and outer cylindrical shell (bottom right of Figure 4.4) to form the acoustic chambers and the structure. A picture of the mock-scale ChamberCore composite fairing considered in this study is shown in Figure 4.5. The length of the cylinder is 775 mm. The diameters of the inner and outer skins are 510 mm and 555 mm, respectively, and the thickness between the inner and outer skins is 20 mm. The angle between two chamber sidewalls is 15 degrees. A density of 1494 kg/m^3 was determined for the material using water displacement techniques. All other material constants for the ChamberCore cylinder are the same as those for ASG cylinder and listed in Table 3.1. Heavy plates constructed from two layers of medium density fiber (MDF) board were installed at the two ends of the ChamberCore cylinder to form a right cylindrical cavity

(height=760 mm, diameter=510 mm). Some treatments of **AP/Armaflex**[®] insulation were used to seal the end caps.
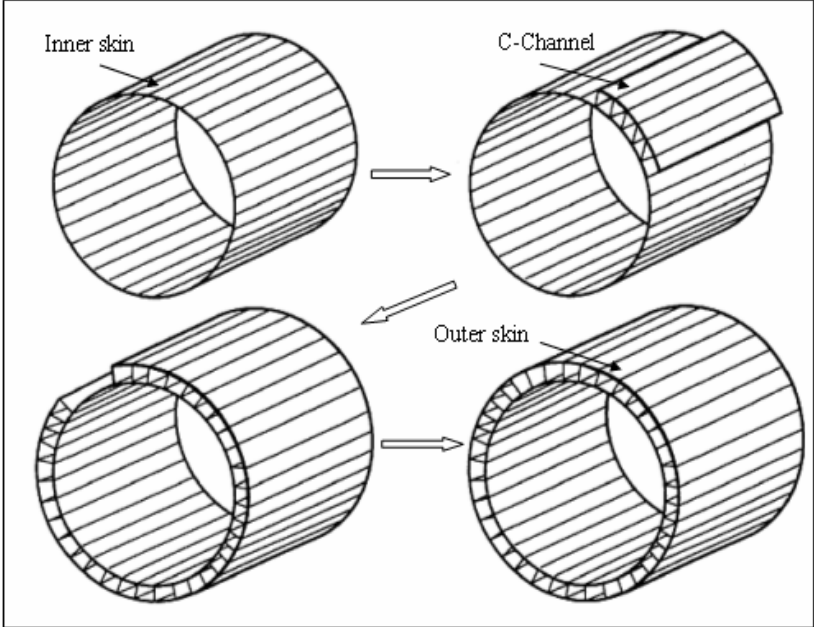
Figure 4.4 Manufacturing Process of the ChamberCore Fairing [32]
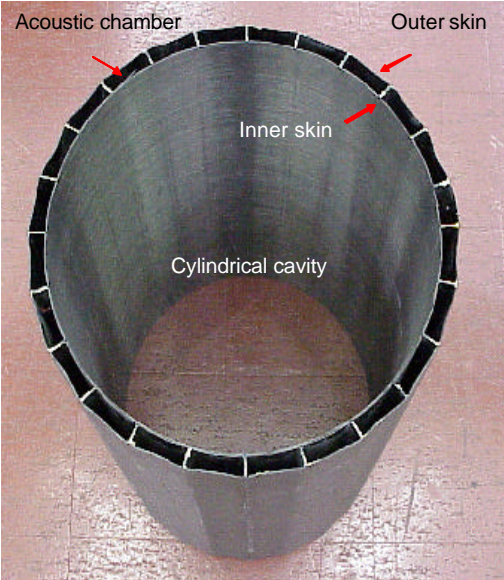
Figure 4.5 Appearance of the Mock-Scale ChamberCore Fairing

4.2.1   Numerical Modal Analysis of the AGS Tapered Cylindrical Fairing

At low frequency, most of the structural modes of the two fairings will resemble the modes of a uniform cylindrical shell, thus, the modes will be identified by indices (o, q) corresponding to the transverse (f) and the axial (z) coordinates, respectively, where the o index represents the number of full waves around the perimeter, and the q index indicates the number of half wavelengths along the z direction. Although the stiffeners mildly prevent true axisymmetry in the AGS tapered cylinder shell, the circumferential modes are still found to occur in pairs.

The structural modal analysis results of the AGS tapered fairing from FEA are presented in Vipperman *et al*. [35]. Selected mode shapes are shown in Figure 4.6.
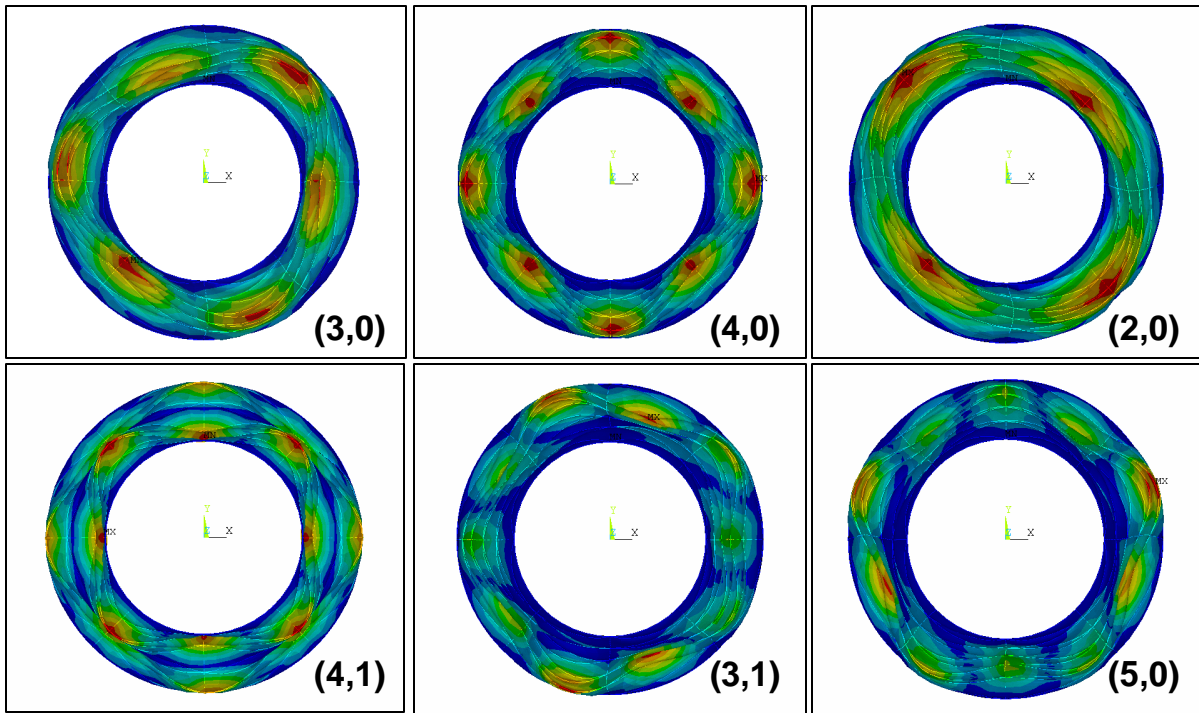
Figure 4.6 Selected Mode Shapes of the AGS Fairing from FEA

Table 4.1 Structural Modal Ordering of the AGS Fairing from FEA

Mode number	Shape (*o, q*)
1	3, 0
2	3, 0
3	4, 0
4	2, 0
5	4, 0
6	2, 0
7	4, 1
8	4, 1
9	3, 1
10	3, 1

4.2.2 Experimental Modal Analysis of the AGS and ChamberCore Fairings

Structural tap tests were conducted in order to experimentally determine the structural modal properties. A PCB model 086C03 modally tuned hammer was used to excite the structure while an array of 8 PCB 352B22 0.5-gram accelerometers measured the response at various locations (see Figure 4.7). The signal (input) from the force sensor installed in the head of the hammer and the signals (output) from accelerometers distributed across the surface of the structure were amplified by a signal conditioner (PCB Model 442A 104), and then were digitalized by SigLab MC20-48 dynamic signal analyzer. For the structural mode shape identification, 208 points were created on the surface of the AGS cylindrical shell, and 672 points were used for the surface of the ChamberCore cylindrical shell. For natural frequency and damping ratio evaluation, a large area was selected on the structural surface, in which 49 and 21 points were distributed for the AGS shell and the ChamberCore shell, respectively. Different driving points were used to provide additional insight. A curve-fit was performed on the measured frequency response functions between the inputs and response locations in order to extract global resonant frequency and damping characteristics using the observability range

space extraction algorithm followed by a nonlinear least square (NLS) optimization, which was realized using the MATLAB® optimization toolbox. Figure 4.8 depicts a representative FRF and curve-fit.
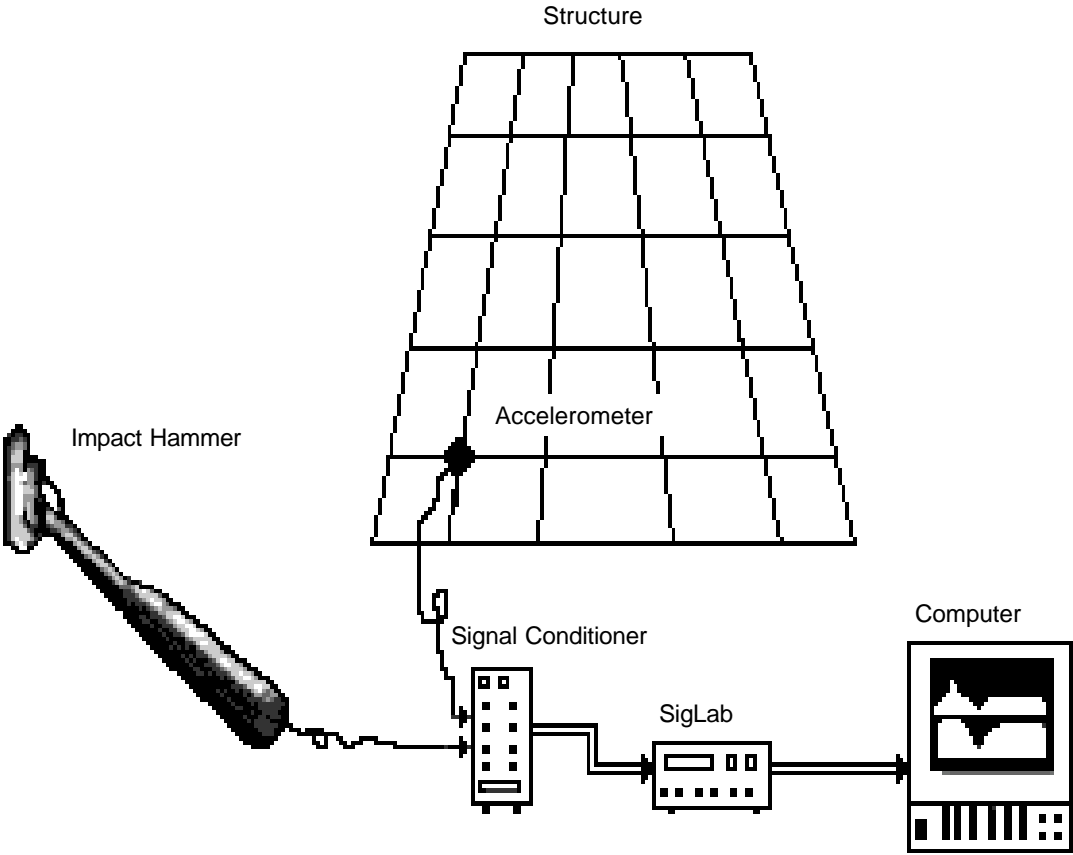
Figure 4.7 Schematic Diagram of the Modal Experimental System
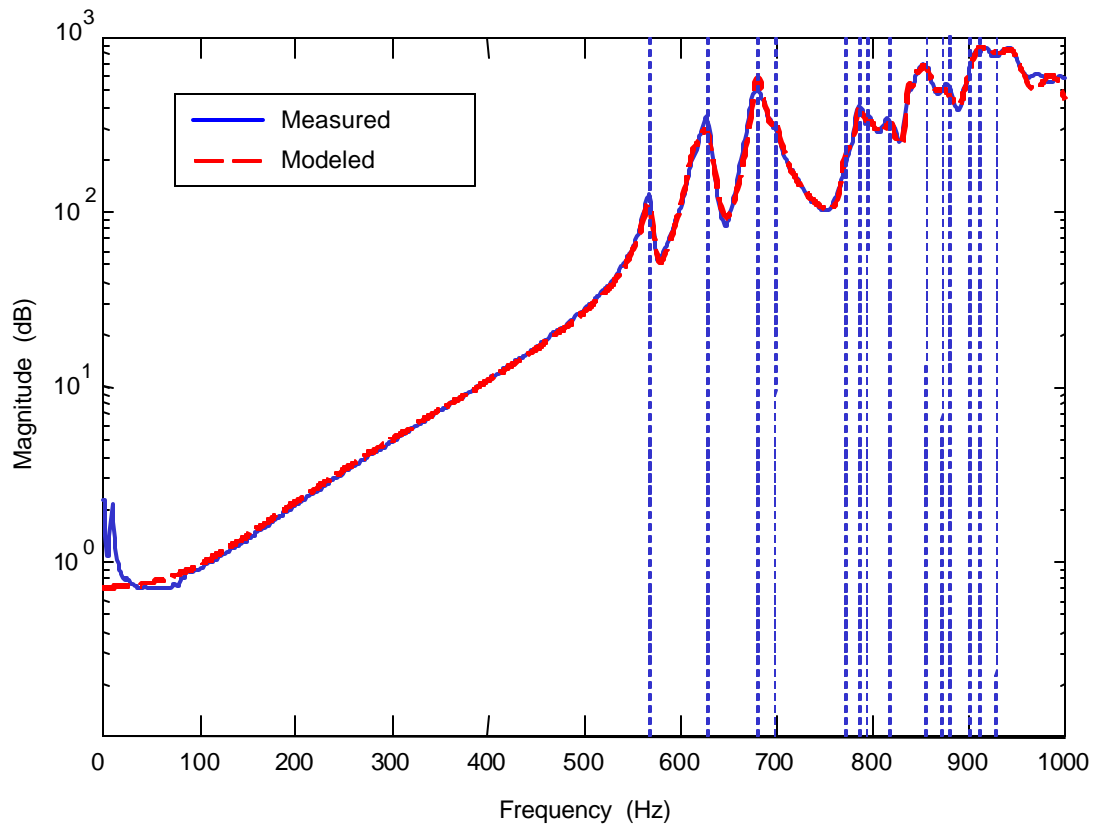
Figure 4.8 Measured Structural FRF and Curve-fit of the AGS Fairing

Table 4.2 represents the results of the AGS structural modal frequencies and damping ratios between 0 Hz and 1000 Hz. The damping values were found to be between 0.04% and 1.5%. The modal density becomes high above 800 Hz. Note that some frequencies listed in Table 4.2 may be an artifact from system identification and not actual modes. The methods proposed in [66] were used to verify them.

Table 4.2 Measured Structural Modal Parameters of the AGS Fairing

Index	Frequency (Hz)	Damping ratio (%)
1	568.5	0.92
2	628.6	1.14
3	680.8	1.00
4	698.6	0.62
5	772.1	0.73
6	786.21	0.45
7	793.4	1.19
8	818.6	0.78
9	843.9	0.33
10	856.2	1.01
11	872.9	1.18
12	901.1	0.82
13	911.4	0.85
14	923.2	0.63

For the ChamberCore configuration, the FRFs between the same input and the normal acceleration of the points on the inside and outside shells (they have the same f and z coordinates) were compared. It was found that there were no differences between inner and outer measurements in the bandwidth of interest. Therefore, the outside shell was experimentally tested for the modal identification. Figure 4.9 shows a representative measured FRF and curve-fit. Table 4.3 shows the modal frequencies and damping ratios of the ChamberCore structure between 0 Hz and 1000 Hz, which were identified by simultaneously curve-fitting 21 selected FRFs.
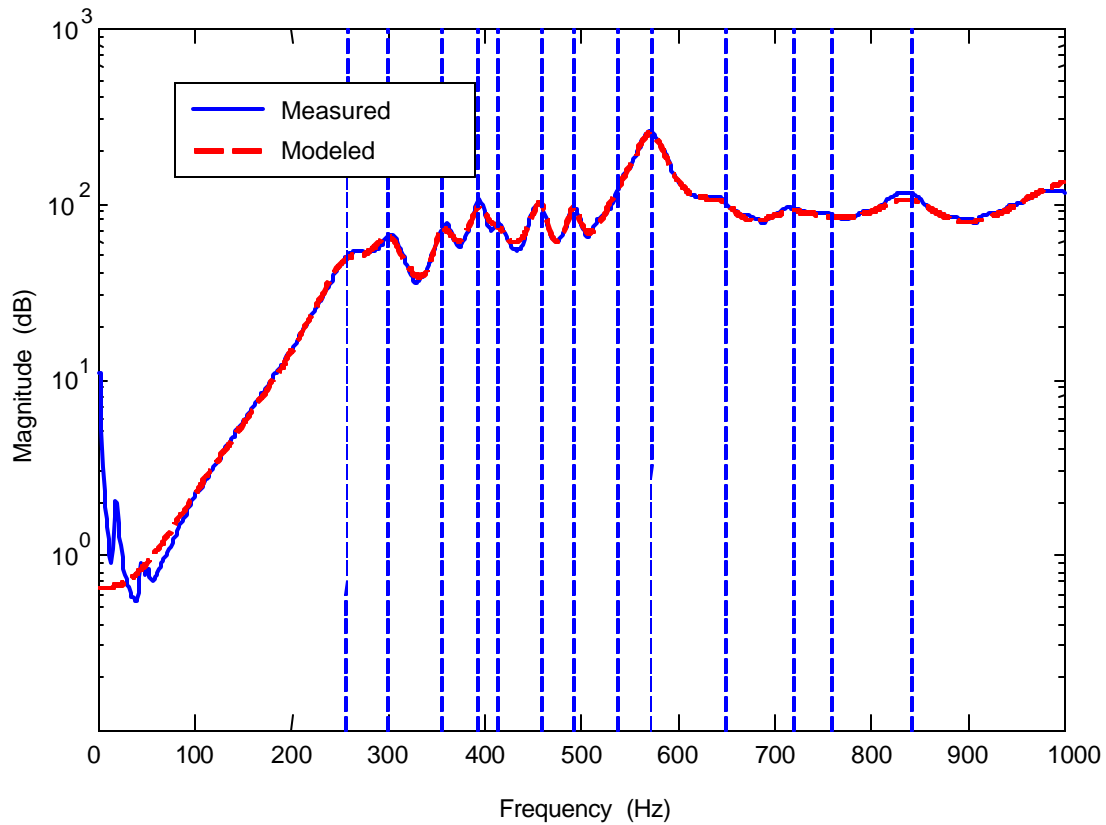
Figure 4.9 Measured FRF and Curve-fit of the ChamberCore Fairing

Comparing Figure 4.9 with Figure 4.8, it is seen that there are seven modes below 500 Hz for the ChamberCore cylindrical structure, but all modes of the AGS cylindrical structure are concentrated in the high frequency range (larger than 500 Hz). Therefore, the ChamberCore cylindrical fairing has more uniform modal density, and higher damping than the AGS tapered cylindrical fairing across the interesting band (from 0 Hz to 1000 Hz).

Table 4.3 Measured Structural Modal Parameters of the ChamberCore Fairing

Index	Frequency (Hz)	Damping ratio (%)
1	256.5	10.08
2	299.2	5.73
3	354.9	3.14
4	392.4	2.67
5	413.6	2.12
6	492.1	6.23
7	538.2	2.59
8	572.2	3.66
9	650.7	7.19
10	718.8	7.26
11	759.4	4.52
12	842.1	5.91

4.3   Acoustic Modal Analysis

The acoustic modes will also be referenced with respect to the cylindrical coordinate system given by Figure 4.3 and the indices (l, m, n). The first modal index, l, represents the number of radial nodes along the r-direction, and the second, m, represents the number of diametric nodes along the transverse f coordinate, and the last, n, represents the number of longitudinal nodes along the z-axis.

4.3.1 Acoustic Modal Analysis of the AGS Tapered Cylindrical Cavity

It is hard to analyze the AGS tapered cylindrical cavity using analytical methods because of the tapered cavity. The FEA method was used to provide a foundation to understand the relationship between mode number, mode shapes and natural frequencies.

Numerical Modal Analysis of the AGS Tapered Cylindrical Cavity

The rigid-wall tapered acoustic cavity was modeled with finite element analysis method, and Figure 4.10 shows some of the resulting acoustic modes that conform well to standard cylindrical mode shapes.
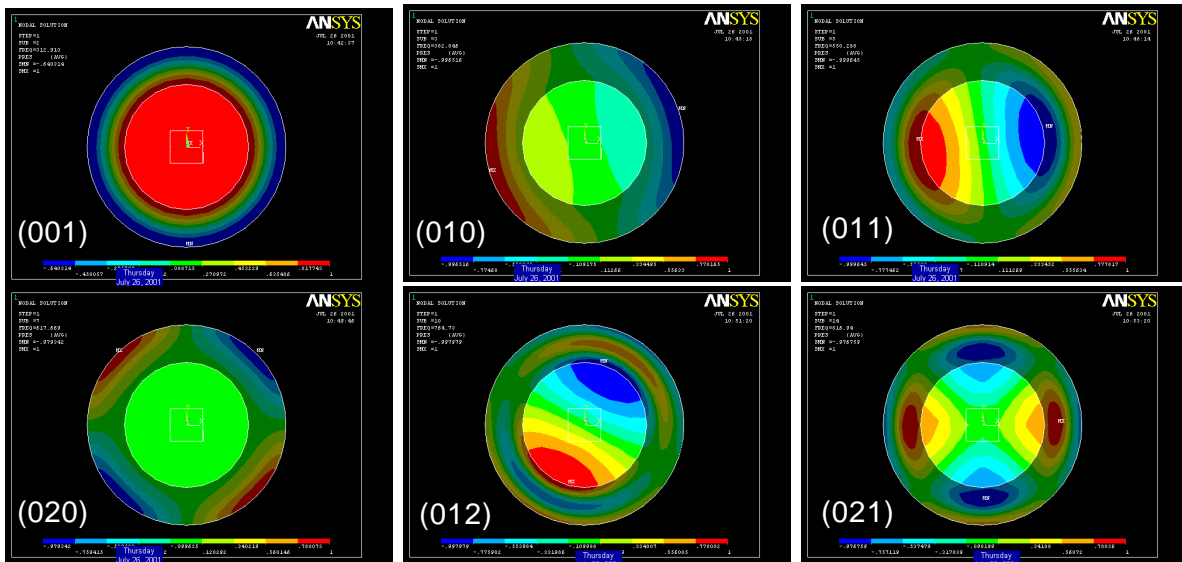
Figure 4.10 Selected Modal Shapes of the AGS Tapered Cylindrical Cavity from FEA

Experimental Modal Analysis of the AGS Tapered Cylindrical Cavity

The experimental acoustic modal analysis was performed by exciting the tapered cylindrical cavity with a Kenwood™ loudspeaker (KFC-W2000) mounted at the bottom. A boom was constructed and installed inside the cylinder. Four microphones were installed on the boom to measure the cavity response. The boom can be rotated around z-axis of the cylinder, and easily moved up and down along the axis. A total of 260 acoustic measurements were taken with the four internal microphones positioned at combinations of the following coordinates: r = {38.1, 76.2, 114, 152} mm, f = {0, 15, 30, 45, 60, 75, 90, 105, 120, 135, 150, 165, 180} degrees, and across vertical planes at z = {152, 254, 356, 457, 559} mm. At each position, the FRF was computed between the input of the speaker and each of the four array microphones. Figure 4.11 shows a typical measured FRF between the speaker and an internal microphone. Note also that the modes of the speaker dynamics have been identified in Figure 4.11.
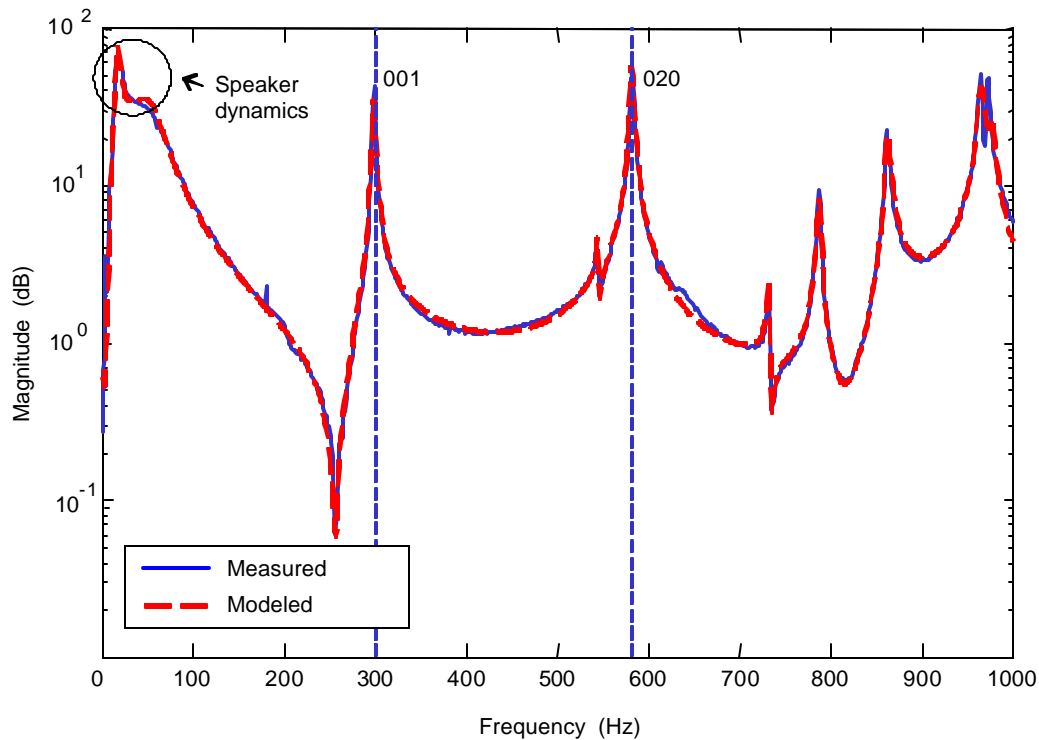
Figure 4.11 Measured FRF and Curve-fit of the AGS Tapered Cylindrical Cavity

A simultaneous curve-fit was performed on 49 of the 260 FRFs, so that modal properties could be extracted. The identified acoustic dynamic parameters between 0 to 1000 Hz are presented in below Table 4.4

Table 4.4 Measured Acoustic Modal Parameters of the AGS Tapered Cylindrical Cavity

Index	FEA shape (l,m,n)	FEA frequency (Hz)	Measured frequency (Hz)	Damping ratio (%)
1	001	312.9	300.5	0.29
2	010	382.8	384.8	0.23
3	011	550.3	547.3	0.18
4	020	617.7	583.0	0.22
5	021	621.7	613.4	0.27
6	012	764.7	735.4	0.14
7	100	786.5	787.5	0.20
8	030	843.2	839.6	0.33
9	031	889.0	867.5	0.28
10	103	946.6	942.0	0.16
11	022	982.1	970.2	0.35

4.3.2 Acoustic Modal Analysis of the ChamberCore Cylindrical Cavity

When analyzing the acoustic-dominated modes, one usually assumes that the cylindrical shell is rigid. The cavity created by the closed ChamberCore cylindrical shell can be seen as a right cylindrical cavity with closed terminations. Therefore, the acoustic properties of this cavity can be easily calculated by analytical methods.

Analytical and Numerical Modal Analysis of the ChamberCore Cylindrical Cavity

The acoustic cavity enclosed by the ChamberCore cylindrical shell and two end caps was modeled as a right cylindrical cavity closed by rigid walls. The height and diameter of the cavity

are 760 mm and 510 mm, respectively. The natural frequencies were analytically and numerically calculated. The equation for the calculation of natural frequencies is Eq. (3.84), and the obtained frequencies below 1000 Hz are listed in Table 4.5. The mode shape indices are the same as those used for the AGS tapered cylindrical cavity. The acoustic mode shapes were obtained from numerical method, and are shown in Figure 4.12.

Table 4.5 Calculated Acoustic Modal Parameters of the ChamberCore Cylindrical Cavity

Index	Analytical shape (l,m,n)	Analytical frequency (Hz)	Numerical frequency (Hz)	Error %
1	001	227.6	227.8	0.1
2	010	397.6	397.9	0.1
3	002	455.3	456.6	0.3
4	011	458.2	458.5	0.1
5	012	604.4	605.6	0.2
6	020	659.6	660.4	0.1
7	021	697.7	698.6	0.1
8	022	801.4	802.9	0.2
9	100	827.5	829.9	0.3
10	101	858.2	860.7	0.3
11	030	907.3	909.9	0.1
12	031	935.4	936.3	0.1
13	102	944.4	945.6	0.1

From the last column in Table 4.5, it is observed that the errors between the numerical and analytical results are very small. It means that accurate results can be obtained using the simple analytical method.

Mode: 001, Frequency: 228 Hz.   Mode: 010, Frequency: 398 Hz

Mode: 002, Frequency: 452 Hz.   Mode: 011, Frequency: 458 Hz
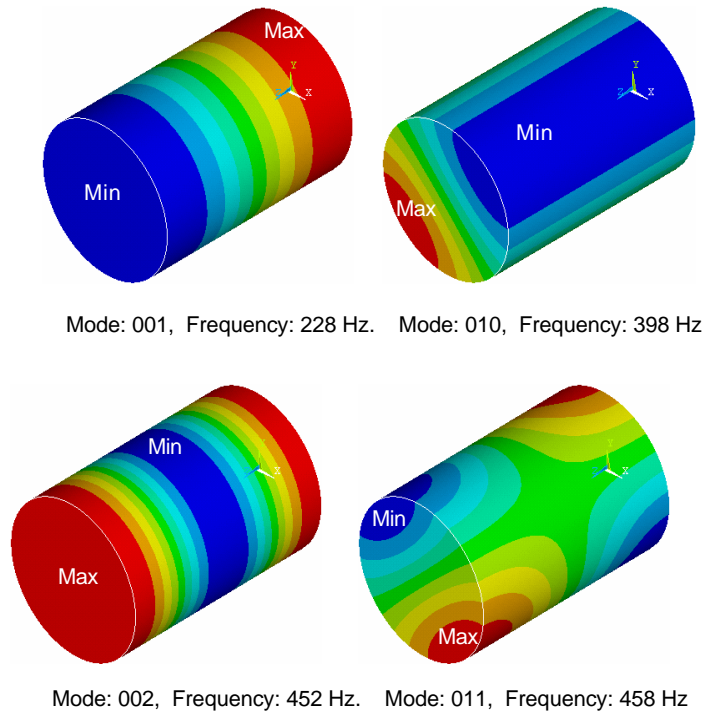
Figure 4.12 Selected Mode Shapes of the ChamberCore Cylindrical Cavity from FEA
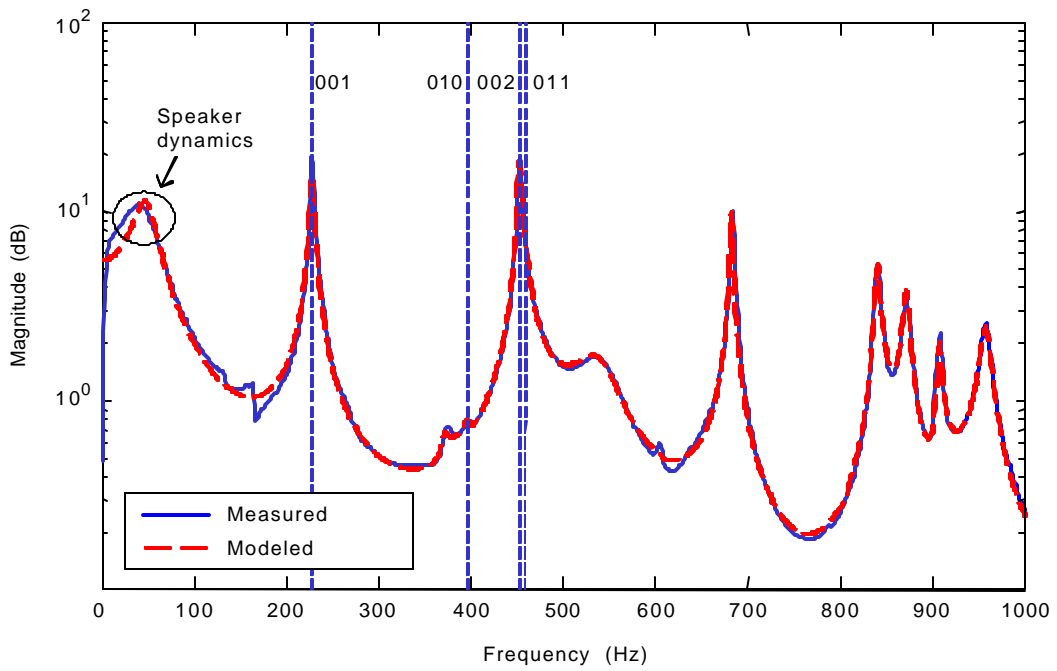
Figure 4.13 Measured FRF and Curve-fit for the ChamberCore Cylindrical Cavity

Experimental Acoustic Modal Analysis of the ChamberCore Cylindrical Cavity

The configuration of the experimental system is nearly identical as that in Section 4.3.1. The difference is that a new boom was constructed since the old one used for the tapered AGS fairing was limited in radius by the small end of the tapered conical shape. The acoustic modal analysis was also performed by exciting the cavity by the attached speaker at the bottom. A total of 48 acoustic measurements were taken with the internal microphones positioned at combinations of the following coordinates: $r = \{55, 145, 235\}$ mm, $f = \{0, 30, 60, 90\}$ degrees, and across vertical planes at $z = \{120, 240, 360, 480\}$ mm. A curve-fit was performed on all measured FRFs for modal frequency and damping ratio identification. The results are presented in Table 4.6. Figure 4.13 shows a typical measured acoustic FRF and curve-fit.

Table 4.6 Measured Acoustic Modal Parameters of the ChamberCore Cylindrical Cavity

Index	Analytical shape (l,m,n)	Analytical frequency (Hz)	Measured frequency (Hz)	Damping ratio (%)
1	001	227.6	227.8	0.99
2	010	397.6	398.0	1.22
3	002	455.3	451.9	0.44
4	011	458.2	458.1	0.87
5	012	604.4	602.1	0.51
6	020	659.6	657.6	0.98
7	021	697.7	681.0	0.23
8	022	801.4	8030	0.49
9	100	827.5	839.5	0.32
10	101	858.2	872.0	0.39
11	030	907.3	906.3	0.28
12	031	935.4	935.5	0.34
13	102	944.4	955.9	0.55

4.4   Measurement of the Sound Transmission Behavior into Cylindrical Shells

In this section, an *in-situ* version of the noise reduction spectrum was developed to experimentally characterize the noise transmission into the composite cylindrical shells. The method is based upon a spatial average of mean-square pressure measurements from the inside and outside of the cylindrical structure, and computed from

$$NRS = -10\log_{10}\frac{\left\langle p_{int}^2 \right\rangle}{\left\langle p_{ext}^2 \right\rangle},\qquad\qquad(4.40)$$

where $< p_{ext}^2 >$ is the exterior mean-square pressure averaged over the exterior shell surface of the cylinder, and $< p_{int}^2 >$ is the internal mean-square pressure averaged over the internal shell surface of the cylinder.

4.4.1   Configuration of the Sound Reduction Spectrum Measurement

Four speakers were arranged around the structure and driven with independent white noise sources having a bandwidth of 0-20 kHz in order to simulate a diffuse field. The speakers and the structure were suspended 620 mm above the floor. An external microphone was traversed to 16 or 24 different measurement locations for the AGS tapered fairing and for the ChamberCore fairing, respectively. The outer measurement microphone was 15 mm from the surface of the cylinder shell. The 16 locations for the AGS tapered cylinder spanned across four different vertical heights, $h = \{44, 190, 330, 480\}$ mm, and four different transverse angles $f = \{0, 90, 180, 270\}$ degrees. The 24 locations for the ChamberCore cylinder spanned across six different vertical heights, $h = \{120, 240, 360, 480, 600, 720\}$ mm. An internal microphone was installed at 20 mm from the internal surface for the AGS structure. The position of the internal microphone for the AGS tapered fairing had to be adjusted after every measurement in order to consider the effects of the taper. An internal microphone was installed at the end of a boom 245

mm from the central axis for the ChamberCore structure. The internal microphone recorded measurements that were at the same height and angles as the exterior measurements.

Figure 4.14 shows the noise reduction spectrum measurement system for the ChamberCore cylindrical fairing. The bottom hole, the attached bottom speaker, and the installed three microphones in the right-hand side of the boom only severed for modal analysis. When measuring noise reduction spectrum, the speaker was removed and the hole was closed and filled with sand. Figure 4.15 depicts a top view of the measurement setup for the ChamberCore cylindrical fairing. The measurement system for the AGS tapered fairing is almost the same as that for the ChamberCore cylindrical fairing. The only difference is that there is no boom inside the AGS tapered cylindrical cavity, and the position of the internal microphone has to be adjusted by hand at every measurement in order to consider the effects of the taper.
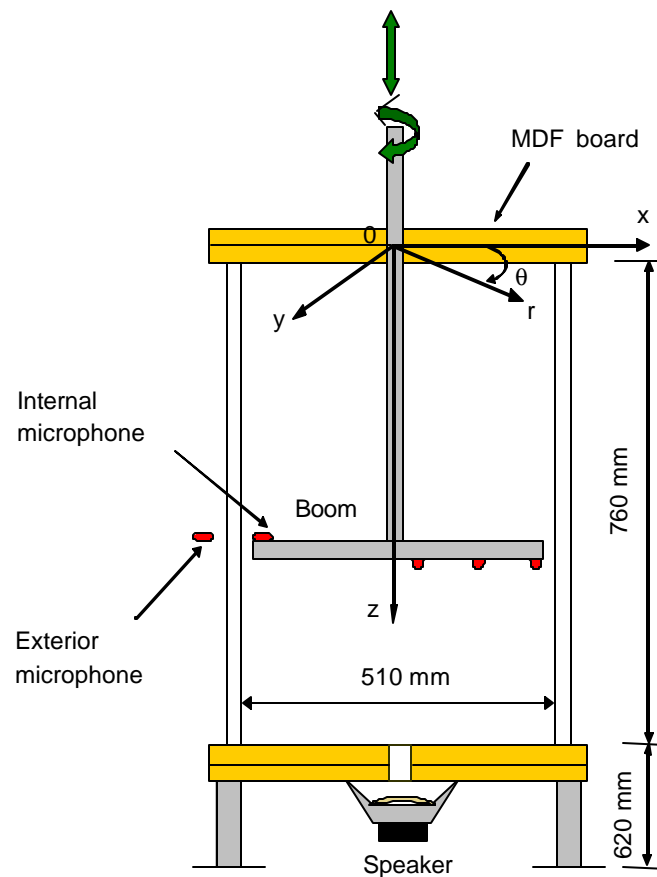
Figure 4.14 NRS Measurement Setup for the ChamberCore Cylindrical Fairing
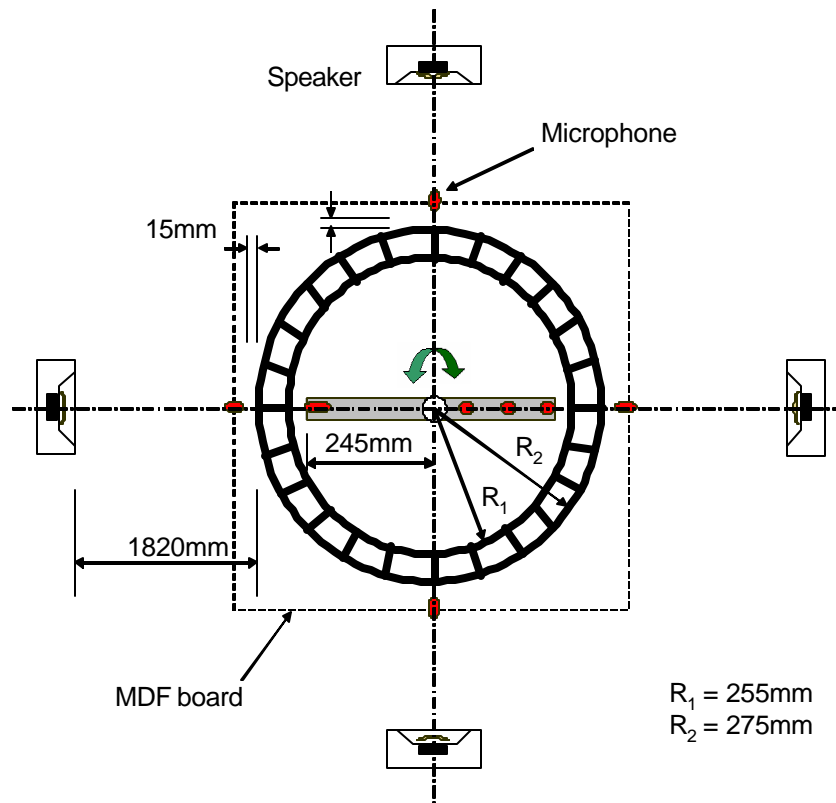
Figure 4.15 Top View of NRS Measurement Setup

All signals were generated and measured using a Siglab MC20-48 dynamic signal analyzer. B&K Type 4190 free-field half inch microphones were used for all measurements. A Marchand PS-24 power amplifier drove enclosed KLH (work bandwidth from 0 to 20,000 Hz) loudspeakers to generate the external noise.

4.4.2   Measured NRS of the AGS Tapered Cylindrical Fairing

The experimental NRS results for the AGS fairing are shown in Figure 4.16 and Figure 4.17. In Figure 4.16, the linear axis was used for both frequency and noise reduction spectrum. The NRS

in the range of [0, 1000] Hz is shown, and the effects of acoustic cavity resonances and structural resonances are indicated in the figure as vertical dashed lines and vertical dash-dotted lines, respectively. The measurements were repeated 3 times with different configurations, and yielded nearly identical NRS results.
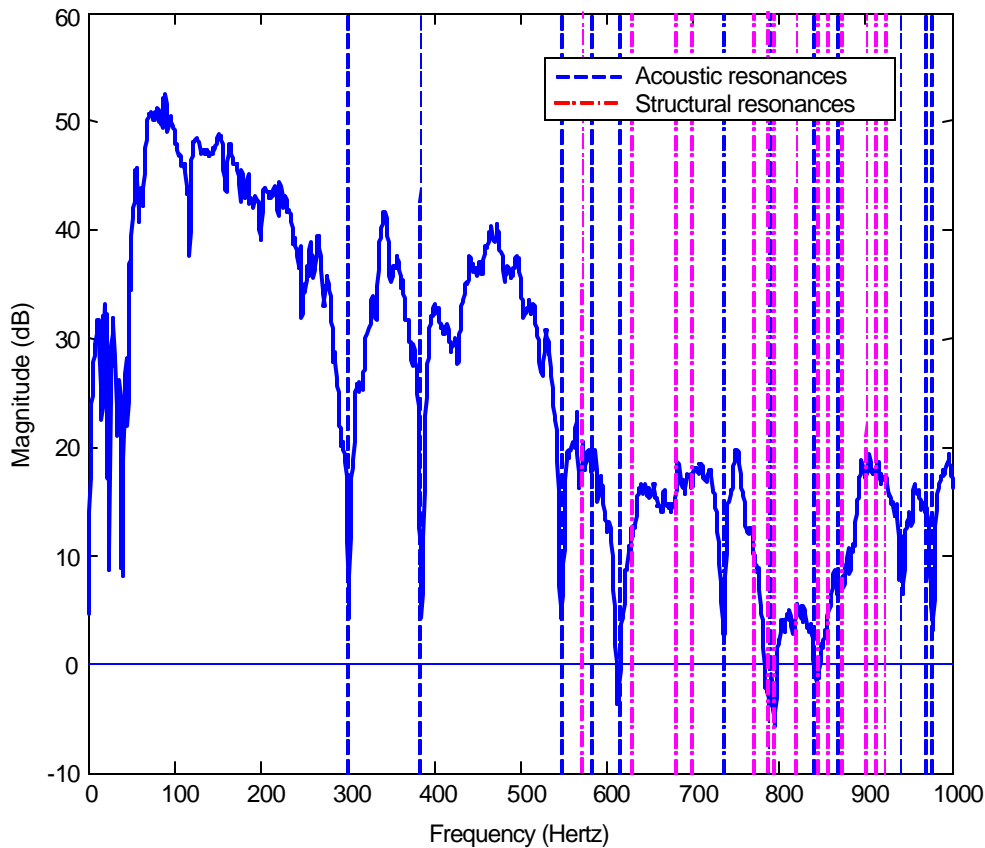
Figure 4.16 Measured NRS of the AGS Fairing (1)

Discussions about Figure 4.16:

(1)   Frequencies below 100 Hz should be ignored, since the bandwidth of the loudspeakers rolls off below 100 Hz. From 100 Hz to the first cavity resonance (300.5 Hz), the NRS has a decreasing trend due to stiffness effects.

(2)   Commensurate dips in the NRS are noted at most all of the acoustically dominant resonant frequencies (e.g. 301, 385, 547, 583, 613, 735, 788, 840, 868, 942, 970, and 976

Hz, with the exception being 583 Hz). It can be seen that the cavity resonances have significant effects on the sound transmission into a cylindrical shell.

(3)   From Figure 4.16, it is found that the structural resonances are also seen to affect on the NRS. The 30-40 dB decrease of NRS happens in the frequency range of 772 to 856 Hz compared with the low frequency range (100-250Hz). Dips exist at the 6th, 7th, 8th, 10th, 11th structural resonances (e.g. 786, 793, 818, 843, 856, and 873 Hz). However, comparing with cavity resonances, structural resonances have less significant effects on the NRS.

(4)   Note that NRS has a minimum at 786 Hz, in which there exists one cavity resonance and two structural resonances. Both structural and acoustic resonances at this frequency likely contribute to the amplification of the internal sound field, which is the lowest observed value on the NRS curve (-5 dB). Note also that the coincidence is predicted to occur there.

(5)   The results of measured NRS show that in order to improve the noise transmission behavior through AGS faring, the acoustically dominant modes will need to be controlled. Internal absorptive treatments are limited in rocket fairings because of the space requirement of the payload. Therefore, alternative acoustic designs should be considered inside the fairing to improve the interior acoustic impedance, such as a reactive design. The NRS could perhaps be improved at 786, 793, 818, 843, 856, and 873 Hz, where structural modes contribute. Some passive control strategies can be considered to improve the damping features of the structural resonances in the high frequency range, but likely at modest improvement.

In Figure 4.17, the NRS is replotted with a logarithmic frequency axis which extends from 100 to 10000 Hz. The approximate structural stiffness-, acoustic cavity resonance-, and mass-controlled regions of the NRS are indicated in the figure. Because the ring frequencies and critical frequencies are not found to help explain the experimental results, they are not shown in the figure.
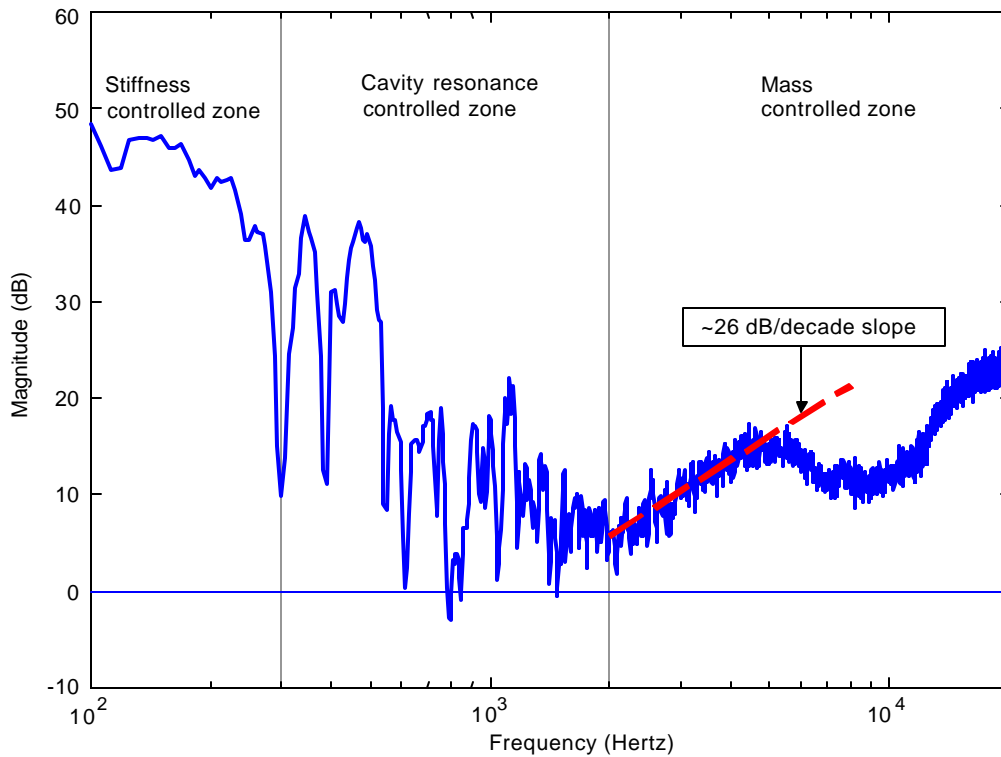
Figure 4.17 Measured NRS of the AGS Fairing (2)

Discussion about Figure 4.17:

(1) Structural stiffness-controlled zone:

From 0 Hz to the first cavity resonance frequency, 301 Hz, the sound transmission will be controlled by the mechanical stiffness.

(2) Cavity resonance-controlled zone:

It begins from the first cavity resonance, 301 Hz, and approximately ends at 2000 Hz.

(4) Mass-controlled zone:

After 2000 Hz, the NRS curve shows a trend developing where the NRS is generally increasing by 26 dB per decade as indicated by the oblique dashed line at the right side of the Figure 4.17. This slope is consistent with classical mass-law behavior, which is also the behavior expected beyond the critical coincidence frequency.

(5) The dip around 10,000 Hz may be induced by ring frequency or coincidence.

4.4.3   Measured NRS of the ChamberCore Cylindrical Fairing

The experimental results of the NRS for the ChamberCore fairing are shown in Figure 4.18 and Figure 4.19. Linear frequency axis is used, and the frequency range of interest is [0, 1000] Hz in Figure 4.18. The cavity resonance frequencies (vertical dashed lines) and the structural resonance frequencies (vertical dash-dotted lines) are shown in the NRS to indicate the effects of acoustic cavity and structural resonances for the ChamberCore cylindrical structure.
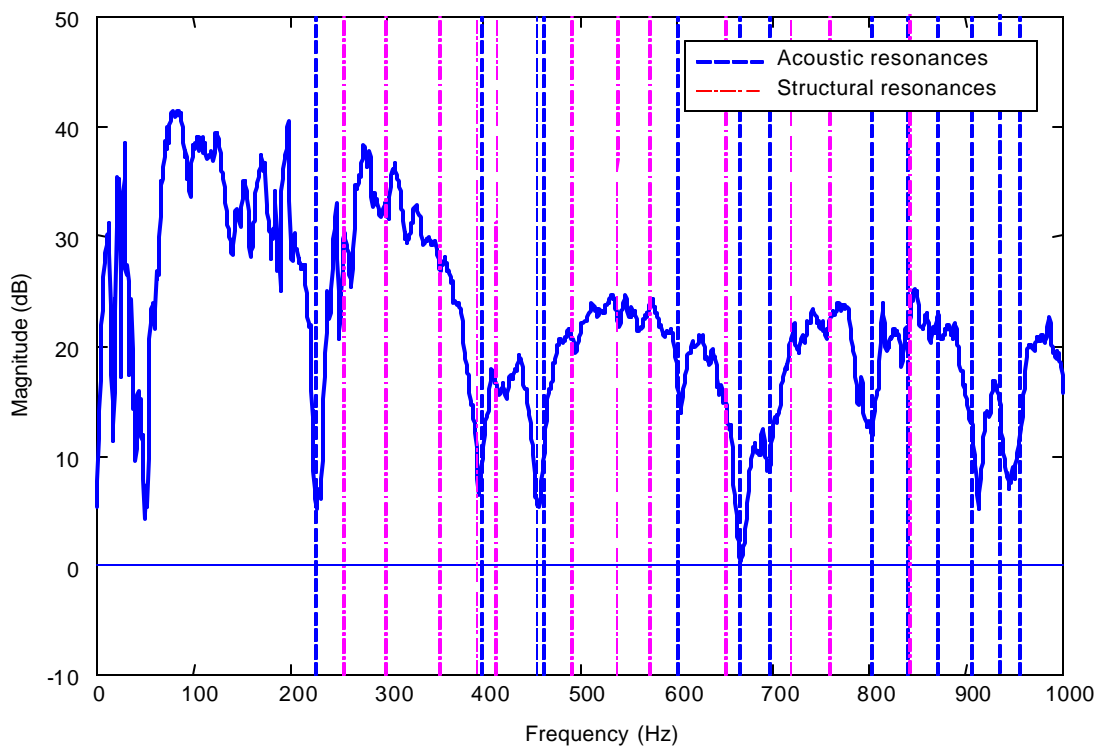
Figure 4.18 Measured NRS of the ChamberCore Fairing (1)

Discussions about Figure 4.18:

(1)   In the low-frequency region of the NRS (from 100 Hz to the first cavity resonance, 228 Hz), the noise reduction spectrum is seen to be roughly 35 dB, but fluctuates a lot.

(2)   Dips in the NRS are noted at most of the cavity resonance frequencies (228, 398, 452,

458, 602, 658, 681, 803, 906, 936 and 956 Hz). There are no dips at the cavity resonance frequencies 840 and 872 Hz.

(3)   The structural resonances are found not to significantly influence the NRS with the exception of the fourth structural resonances at 392 Hz (damping 2.7%), where both acoustic and structural resonances occur, it is hard to say if both of cavity and structural resonance affect NRS there.

(4)   The minimum value of the NRS occurs at the sixth acoustic cavity mode at 660 Hz.

(5)   The measurement results show that the cavity resonances have the most influence on the NRS. In order to reduce the noise transmission through the ChamberCore cylinder, the acoustically dominant modes will need to be controlled.

Methods to change the interior acoustic impedance of the ChamberCore fairing should be considered, such as acoustic Helmholtz resonators. The NRS could perhaps be improved at 392 where ChamberCore structural modes are thought to contribute by applying constrained layer damping treatments.
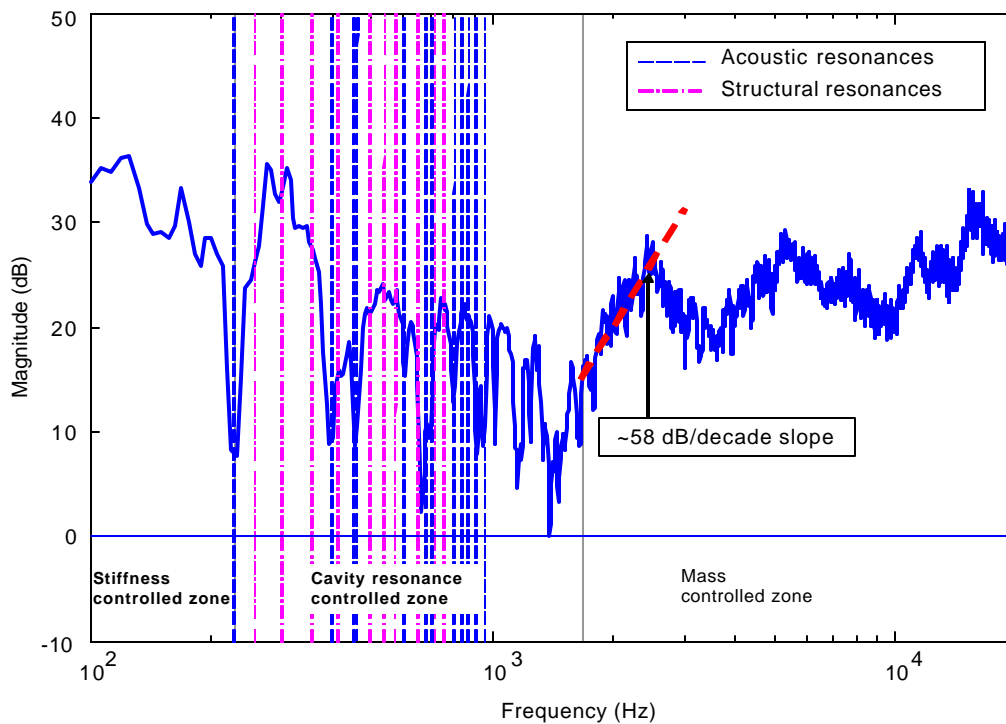
Figure 4.19 Measured NRS of the ChamberCore Fairing (2)

In Figure 4.19, the logarithmic scale is also used for the frequency axis along with a large frequency range (100 - 20000 Hz). The acoustic and structural resonances are indicated as vertical dashed lines and vertical dash-doted lines in the figure. The approximate structural stiffness-, acoustic cavity resonance-, and mass-controlled zones of the NRS are also presented in the figure. The ring frequency, critical frequencies are not shown in the figure because these frequencies were not found to be useful to characterize the NRS.

Discussion about Figure 4.19:

(1)   Structural stiffness-controlled zone

The "structural stiffness-controlled" zone is from 0 Hz to the first cavity resonance frequency, 228 Hz.

(2)   Cavity resonance-controlled zone

It begins at the first cavity resonance at 228 Hz, and ends at the beginning of the coincidence-controlled zone at about 1600 Hz.

(4)   Mass-controlled zone

When the frequency is larger than 1600Hz, there is a trend developing where the NRS is generally increasing by 58 dB per decade as indicated by the oblique dashed line at the right side of the Figure 4.19. This trend is consistent with the classical mass-law behavior.

(5)   The dips in the mass-controlled zone may be induced by ring frequency or coincidence.

4.5   Conclusions

In this chapter, the dynamic properties of the AGS tapered composite fairing and the ChamberCore composite fairings were analyzed numerically, analytically, and experimentally. The noise transmission behavior of the two composite fairings was also experimentally characterized by means of the measurement of noise reduction spectrum. It is found that the

cavity resonances have significant effects on the sound transmission into the fairings, and the structural resonances do not find to significantly influence the sound transmission into the fairings. The stiffness-controlled zone, cavity resonance-controlled zone and mass-controlled zone were identified to characterize the sound transmission behavior of the two fairings. The experimental results are consistent with the theoretical results which were proposed in Chapter 3.0.

5.0 NOISE TRANSMISSION CONTROL FOR THE CHAMBERCORE CYLINDRICAL FAIRING USING PASSIVE MATERIALS

Passive control strategies are widely used in the aerospace industry because they are simple and practical [8, 9, 10]. In this chapter, the effects on the noise transmission reduction of passive materials were experimentally investigated. This study also served to experimentally verify the three regions in NRS curves (stiffness-controlled zone, cavity resonance-controlled zone, and mass-controlled zone) identified in Chapter 4.0.

5.1 Noise Transmission Control Using Passive Materials

Four kinds of passive materials with different density were used in this study. They were (1) fiberglass (density 17 kg/m^3), (2) opened cell foam (density 32 kg/m^3), (3) perlite (density 152 kg/m^3), (4) polyethylene pellets (density 544 kg/m^3), and (5) sand (density 1603 kg/m^3). The use of sand is not suggested as a practical control means, but rather as a "best case" passive control material. These passive materials were respectively filled into the wall-chambers of the ChamberCore cylindrical structure, and the noise reduction spectrums were measured by the developed system in Chapter 4.0. The NRS results are shown from Figure 5.1 to Figure 5.5
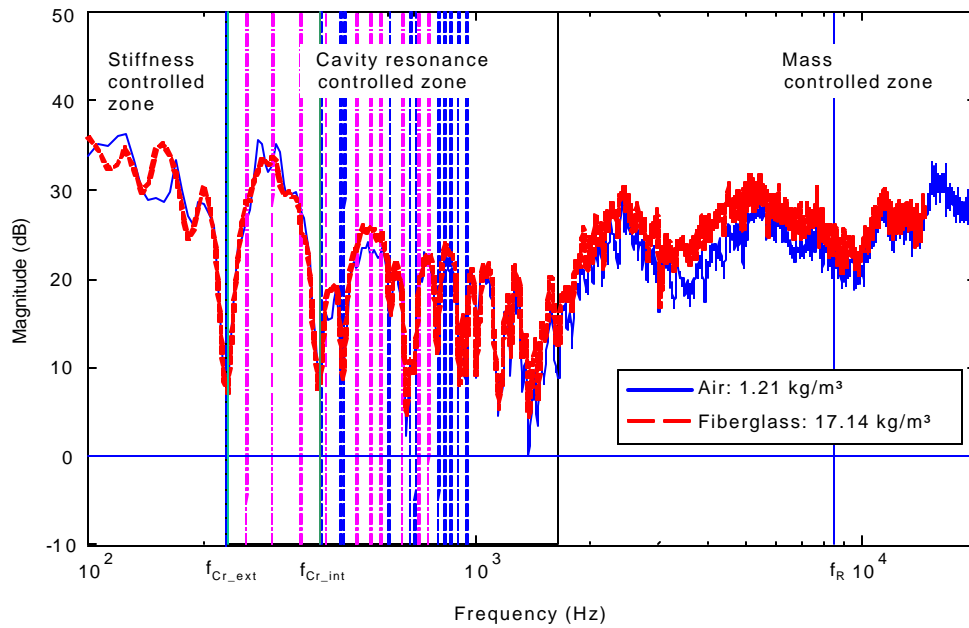
Figure 5.1 Noise Transmission Control Using Passive Fill Materials (1)
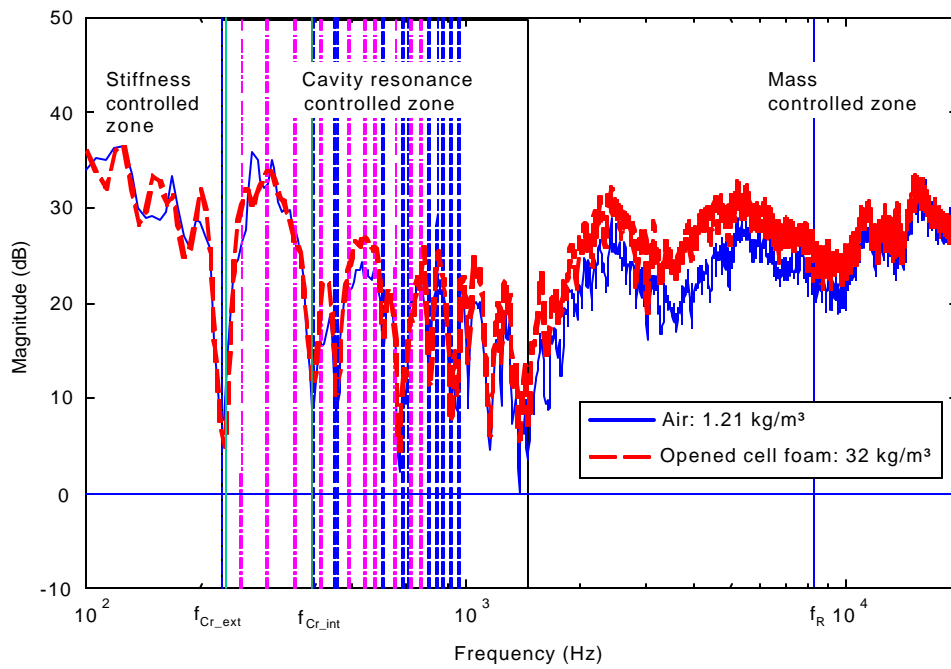
Figure 5.2 Noise Transmission Control Using Passive Fill Materials (2)
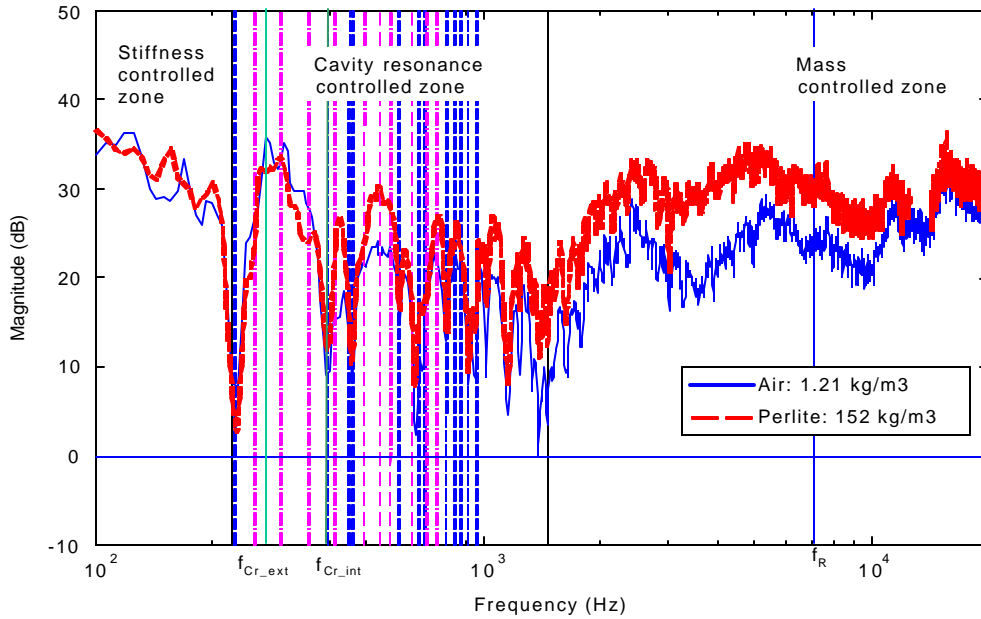
Figure 5.3 Noise Transmission Control Using Passive Fill Materials (3)
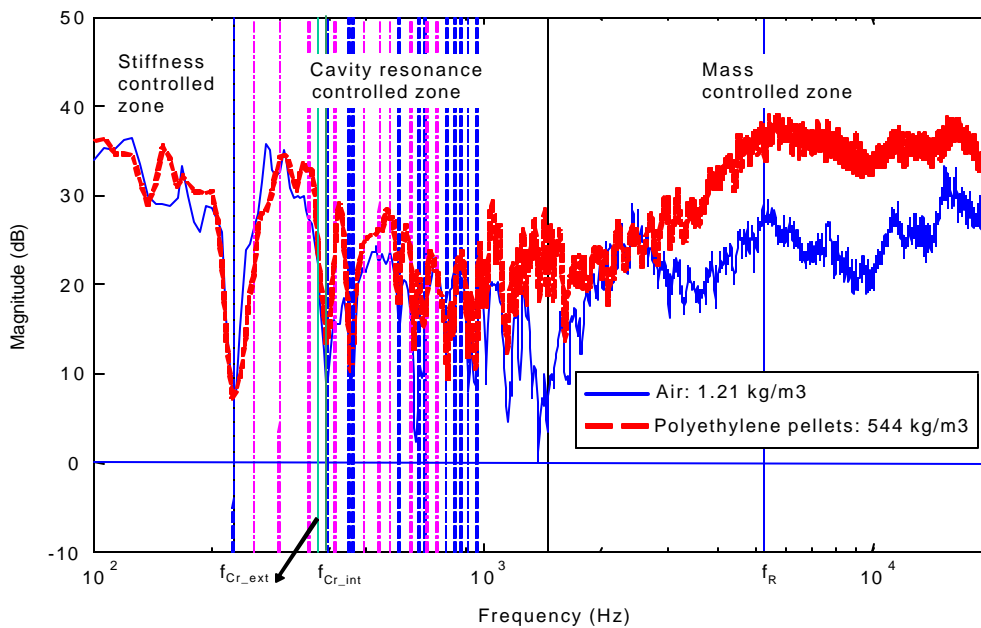
Figure 5.4 Noise Transmission Control Using Passive Fill Materials (4)
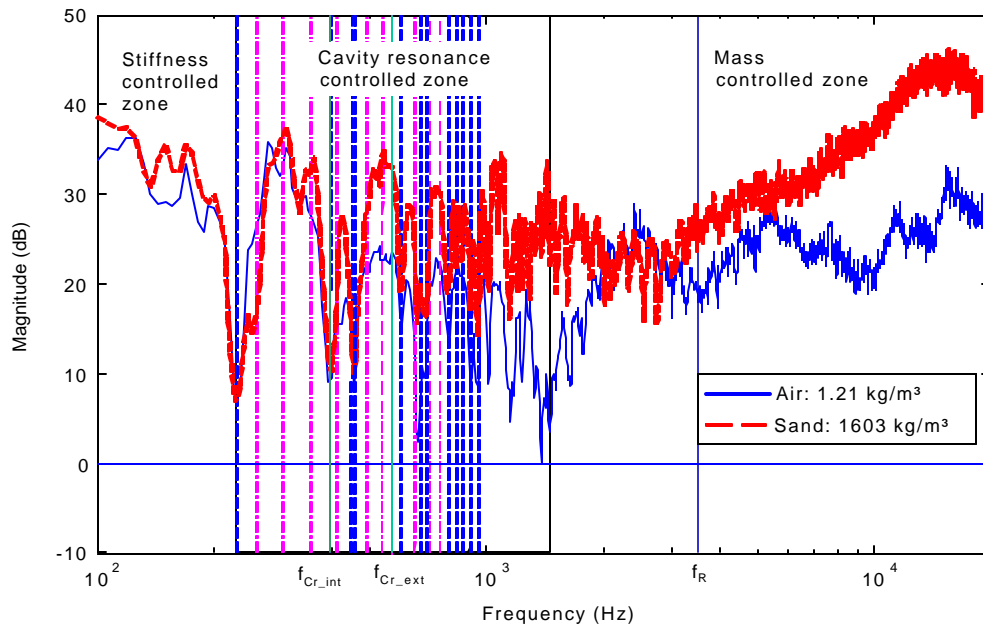
Figure 5.5 Noise Transmission Control Using Passive Fill Materials (5)

From Figure 5.1 to Figure 5.5 the solid line represents the NRS for the empty wall-chambers, and the dashed line indicates the NRS for the wall-chambers filled with passive materials. f_{Cr_int}, f_{Cr_ext}, and f_R are the internal critical frequency, external critical frequency, and ring frequency, respectively. From Figure 5.1 to Figure 5.5 it can be observed that the NRS in the stiffness-controlled zone is mostly unaffected by fills since they have little contribution to the structural stiffness. One can also observe that as the density of fill increases, improvement of the NRS in the mass-controlled zone as well as in the cavity resonance controlled zone occurs. For the lighter fills (i.e. fiberglass and opened cell foam) the NRS results in little change of the cavity resonance-controlled zone, because the small variation in density cannot significantly change structural dynamic properties. However, for the higher density fills (i.e. perlite, polyethylene pellets and sand) the part of cavity resonance-controlled zone closest to the mass-controlled zone is more significantly affected because a significant reduction of the structural dynamic response occurs for this case. However, there is no improvement found in the first cavity resonance. One can see improvements between resonances, but even more at higher resonances. Thus, putting

fills inside the wall-chambers is not a practical control strategy since the cavity resonances dominate the NRS.

From these NRS curves, the cavity resonance-controlled zone can be approximately determined that it begins from the first cavity resonance 228 Hz, and ends near 1600 Hz. Before the cavity resonance-controlled zone is the stiffness-controlled zone, and after the cavity resonance-controlled is the mass-controlled zone. This result is the same as that identified in Chapter 4.0.

5.2   Conclusions

In this chapter, passive control using various fills was investigated. The results of passive control measurements showed that installing passive fills in the wall-chambers could not affect the NRS in the stiffness-controlled zone but significantly affect the NRS in the cavity resonance-controlled zone and mass-controlled zone.

6.0 NOISE TRANSMISSION CONTROL FOR THE CHAMBERCORE CYLINDRICAL FAIRING USING ACOUSTIC RESONATORS

The investigation results have determined that the sound transmission into the Chamber-Core cylindrical fairing in the low-frequency band is dominated by acoustic cavity resonances [34, 35, 77 -79]. Therefore, noise attenuation at the first several cavity resonances (such as, 228, 398, 451, 458 Hz) will significantly improve the sound transmission into the ChamberCore fairing in the low frequency band [93]. There are several types of proprietary acoustic tiles, foams and heavy acoustic blankets that can effectively absorb noise energy above 300 Hz in payload fairings [6, 80]. However, dealing with the low-frequency band sound requires a different approach. The reason for this is that low-frequency sounds have long wavelengths and a purely absorptive low frequency acoustic blanket needs to be at least one eighth of a wavelength deep to be effective. At a frequency of 200Hz, that's approaching eight inches, which is obviously prohibitive. Understandably, a more popular approach is to build a damped, resonant structure that will absorb a significant proportion of a specific frequency band by converting it to heat via frictional losses.

The Helmholtz resonators are commonly used for this purpose, and have been very widely used in architecture or cavity noise control [81, 82, 83]. However, to be successful, the working frequency of the Helmholtz resonator must be accurately tuned to the frequencies which they are to control. Generally, a Helmholtz resonator has a very narrow bandwidth, but by introducing an absorbent material such as fiberglass or mineral wool into the neck, the operating range can be widened.

Many acoustic liners in aircraft engine intake and exhaust applications are Helmholtz resonators [84]. These acoustic liners are appropriately designed to provide a desired acoustic impedance boundary condition that reduces the propagation of noise in the engine nacelle. Single layer passive liners generally consist of a perforated face plate and a rigid back plate, separated by a honeycomb structure. These operate together as a conventional Helmholtz resonator.

Acoustic energy may be absorbed by viscous effects at the facing sheet and by the onset of turbulence.

Because of the special structure of the ChamberCore cylinder, its chambers provide a potential for the Helmholtz resonator realization to reduce the noise transmission into the ChamberCore fairing. There are two types of acoustic resonators modeled, designed, and manufactured in this chapter. First is the short cylindrical Helmholtz resonator which was used to preliminarily investigate the feasibility of the noise control of the ChamberCore cylinder in low frequency band (below 500 Hz), and second was the long T-shaped acoustic resonator. The long T-shaped acoustic resonators are used here because they more closely match the final acoustic resonator version, which were integrated into the chambers of the ChamberCore cylindrical fairing. In this chapter, it is always assumed that only plane wave can propagate in the two kinds of resonators, therefore, the wavelength of interest sound must be much larger than the maximum cross-sectional geometric dimension of the resonators. The targeted frequencies are the first four cavity resonances: (001) mode at 228 Hz, (010) mode at 398 Hz, (002) mode at 452 Hz and (011) mode at 458 Hz (see Table 4.6). The final goal is to obtain at least a 3 dB improvement in the noise reduction spectrum in the vicinity of these frequencies.

6.1   Preliminary Study of Noise Transmission Control Using Helmholtz Resonators

The feasibility of noise control using Helmholtz resonators was investigated in this section. The reason for using the short cylindrical Helmholtz resonators in the preliminary investigation is based on the two problems under consideration: firstly, the short resonator is a conventional Helmholtz resonator, it is easy to model and design, and secondly, the structure of cylindrical resonator is simple and easy to manufacture [94]. The new model of cylindrical Helmholtz resonator for resonant frequency calculation and design was derived using the wave propagation theory [90]. The Helmholtz resonators were designed and manufactured. The effect of the resonator position on the noise reduction was experimentally investigated, and the relationship between two or more closely spaced resonators was also experimentally studied. The

optimal positions of the Helmholtz resonators were discussed. The noise control using cylindrical Helmholtz resonators was investigated experimentally.

6.1.1 Cylindrical Helmholtz Resonator: Principle, Resonant Frequency and Design

Helmholtz resonator (HR) is named after Hermann Ludwig Ferdinand von Helmholtz (1821-1894), the German scientist who worked out the design equation for the resonator. Essentially, a Helmholtz resonator consists of two parts, a rigid-walled cavity of volume V, and a neck or an opening with area S and length L. The absorption principle of the Helmholtz resonator is that when putting a Helmholtz resonator in a sound field at a resonant frequency, it will expose very low acoustic impedance at its opening and the sound level will drop in the vicinity during one acoustic cycle. At the same time because of rather high impedance at the closed end of its cavity the sound level inside the resonator goes up and the energy is dissipated into heat. The part of the energy which is not dissipated will be returned to the sound field at later cycle.

In the classical model of the Helmholtz resonator, it is lumped into the following three idealized elements. The fluid in the neck moves as a unit to store kinetic energy and provides the mass element. The opening radiates sound, thus provides the resistance element, and the viscous losses of the moving air in the neck provides additional resistance. The compressible air in the cavity stores potential energy, and is modeled as stiffness element. The classical formula for calculation of the resonance frequency of the Helmholtz resonator is as shown the following, which can be found in every standard acoustic text-book:

$$ f = \frac{c}{2p} \sqrt{\frac{S}{L_{eff}V}} , \tag{6.1} $$

where c is the speed of sound, and L_{eff} is the effective neck length which includes end corrections [85, 86]. This model can just work at the low frequency band where the largest physical dimension of the resonator is much smaller than the acoustic wavelength [85, 86]. Alster's work has shown that the error of the resonance frequencies between calculated by Eq. (6.1) and measured sometimes reaches as much as 30 percent [87]. Therefore, acoustics

researchers proposed several extended theoretical models for Helmholtz resonators to obtain more accurate resonant frequencies [87, 88, 89]. In this section, the wave acoustic theory is used to derive general and accurate formulas for resonant frequency calculation and cylindrical Helmholtz resonator design.
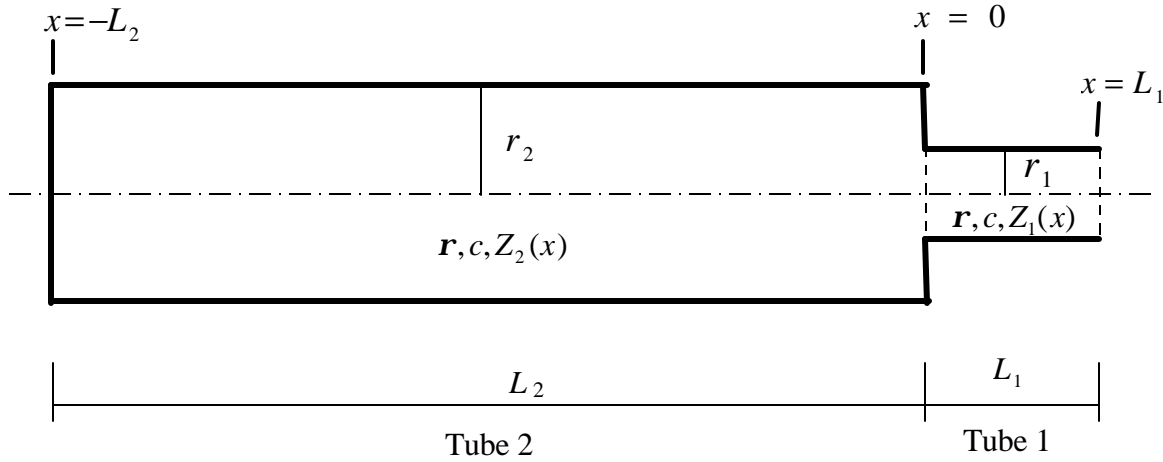
Figure 6.1 Cylindrical Helmholtz Resonator

A cylindrical Helmholtz resonator is shown in Figure 6.1. The resonator consists of two concentric circular tubes. Tube 1 with area S_1 and effective length L_1 is the neck of the resonator. Tube 2 with area S_2 and length L_2 is the cavity of the resonator. It is assumed that only plane waves propagate in the two tubes. The general expression for the acoustic pressure in the position x is

$$p(x,t) = Ae^{j(wt-kx)} + Be^{j(w+kx)}, \tag{6.2}$$

where the constants A and B are determined by the boundary conditions at $x=0$, $x=L_1$ and $x=-L_2$. $k=?/c$ is the wavenumber, and $?$ is the sound source frequency. The continuity equation holds at the junction of Tube 1 and Tube 2

$$Z_1(0) = Z_2(0) , \tag{6.3}$$

where $Z_1(0)$ and $Z_2(0)$ are the acoustic impedance of the two tubes at $x=0$, respectively. The acoustic impedance at the position x can be expressed as [90]

$$Z(x) = \frac{rc}{S} \frac{Ae^{-jkx} + Be^{jkx}}{Ae^{-jkx} - Be^{jkx}}. \tag{6.4}$$

For Tube 1, the acoustic impedance at $x=0$ and $x=L_1$ can be expressed as

$$Z_1(0) = \frac{rc}{S_1} \frac{A+B}{A-B}, \tag{6.5}$$

$$Z_1(L_1) = \frac{rc}{S_1} \frac{Ae^{-jkL_1} + Be^{jkL_1}}{Ae^{-jkL_1} - Be^{jkL_1}}. \tag{6.6}$$

Eliminating the constants A and B from Eqs. (6.5) and (6.6) yields

$$Z_1(0) = \frac{Z_1(L_1) + j\dfrac{rc}{S_1}\tan(kL_1)}{1 + j\dfrac{S_1}{rc}Z_1(L_1)\tan(kL_1)}. \tag{6.7}$$

A similar expression follows for Tube 2:

$$Z_2(0) = \frac{Z_2(-L_2) - j\dfrac{rc}{S_2}\tan(kL_2)}{1 - j\dfrac{S_2}{rc}Z_2(-L_2)\tan(kL_2)}. \tag{6.8}$$

From the boundary conditions we know that

$$Z_1(L_1) = 0, \tag{6.9}$$

$$Z_2(-L_2) = \infty. \tag{6.10}$$

Substituting Eqs. (6.9) and (6.10) into Eqs. (6.7) and (6.8), yields

$$Z_1(0) = j\frac{rc}{S_1}\tan(kL_1), \tag{6.11}$$

$$Z_2(0) = j\frac{rc}{S_2}\cot(kL_2). \tag{6.12}$$

Substituting Eqs. (6.11) and (6.12) into (6.3), we get the eigenfunction for the cylindrical Helmholtz resonator:

$$\tan(kL_1) = \frac{S_1}{S_2}\cot(kL_2), \tag{6.13}$$

where $k = ?/c$. The first eigenvalue is called the "Helmholtz" frequency, and succeeding determining the higher modes of the resonator. Note that the derivation here is more general in the sense that no particular tube length has been assumed. Therefore, the neck and the cavity length may be comparable to a wavelength or longer than a wavelength. Also note that all derivation here is base upon the plane wave propagation principles, thus the maximum diameter of the resonator must be much smaller than the interest wavelength.

The Maclaurin series expansions for the tangent and cotangent functions are:

$$\tan kl = kl + \frac{1}{3}(kl)^3 + \frac{2}{15}(kl)^5 + \cdots. \tag{6.14}$$

$$\cot kl = \frac{1}{kl} - \frac{1}{3}(kl) - \frac{1}{45}(kl)^3 - \cdots. \tag{6.15}$$

When the first two terms in Eqs. (6.14) and (6.15) are retained, a sufficiently accurate Helmholtz resonator formula is found from Eq. (6.13) and simplified to

$$w = c\sqrt{-\frac{3L_1S_2 + L_2S_1}{2L_1^3S_2} + \sqrt{\left(\frac{3L_1S_2 + L_2S_1}{2L_1^3S_2}\right)^2 + \frac{3S_1}{L_1^3L_2S_2}}} \ . \tag{6.16}$$

If the maximum geometric dimension of the resonator is smaller than 1/16 of a wavelength [88], the classical formula Eq. (6.1) can be found by retaining the first term in Eqs. (6.14) and (6.15).

If L_1 is very small, the Panto and Miller's formula can be obtained by retaining the first term in Eq. (6.14), and the first two terms in Eq. (6.15), and simplifying to [88]

$$w = c\sqrt{\frac{S_1}{L_1L_2S_2 + \frac{1}{3}L_2^2S_1}} \ . \tag{6.17}$$

Eq. (6.13) will be used to design the cylindrical Helmholtz resonator. If given any four of L_1, S_1, L_2, S_2, and $?$, the unknown parameter can be solved from Eq. (6.13). For instance, given L_1, S_1, S_2, and $?$, then L_2 can be solved as

$$L_2 = \frac{c}{w}\,arc\cot\left(\frac{S_2}{S_1}\tan\left(\frac{w}{c}L_1\right)\right). \tag{6.18}$$

The effective neck length L_1 can be expressed as

$$L_1 = L_{neck} + \Delta L_{in} + \Delta L_{out} , \tag{6.19}$$

where L_{neck} is the neck length, $?L_{in}$ is the interior end correction, and $?L_{out}$ is the outer end correction. Rayleigh proposed the well-known correction for $?L_{out}$ [85], and Ingard proposed the inside end correction $?L_{in}$ [86].

$$\Delta L_{out} = \frac{8}{3p}r_1 , \tag{6.20}$$

$$\Delta L_{in} = 0.85\left(1 - 1.25\frac{r_1}{r_2}\right), \qquad \left(\frac{r_1}{r_2} \le 0.4\right), \tag{6.21}$$

$$\Delta L_{in} = 0.19 r_1, \qquad \left(\frac{r_1}{r_2} = 0.65\right). \tag{6.22}$$

The design of the Helmholtz resonator consists of three main elements. The first is a hollow PVC tube to provide a volume for the resonator cavity. The second element is the two plastic end caps to close the PVC tube and create the cavity. The third element in the design is the opening in one end cap to create the neck of the resonator. The geometric dimensions of the designed cylindrical Helmholtz resonators are listed in Table 6.1. Note the numbering convention for the resonators, where the number corresponds to the resonant frequency, e.g. HR-228 is a 228 Hz resonator.

Table 6.1 Geometric Dimensions of Cylindrical Helmholtz Resonators

Helmholtz resonator name	Helmholtz frequency (Hz)	Neck radius r_1 (mm)	Neck area (mm^2)	Neck length (mm)	Cavity radius r_2 (mm)	Cavity area (mm^2)	Cavity length (mm)
HR228	228	4.8	72.4	6.7	20.2	1281.9	188.3
HR398	398	16.0	804.2	5.9	20.2	1281.9	181.9
HR452	452	16.0	804.2	5.9	20.2	1281.9	156.1
HR458	458	16.0	804.2	5.9	20.2	1281.9	153.6

6.1.2 Experimental Verification

In order to verify the theoretical predictions, an experiment was designed to measure the frequency response of the Helmholtz resonators used in this study. The measurement system is shown in Figure 6.2.
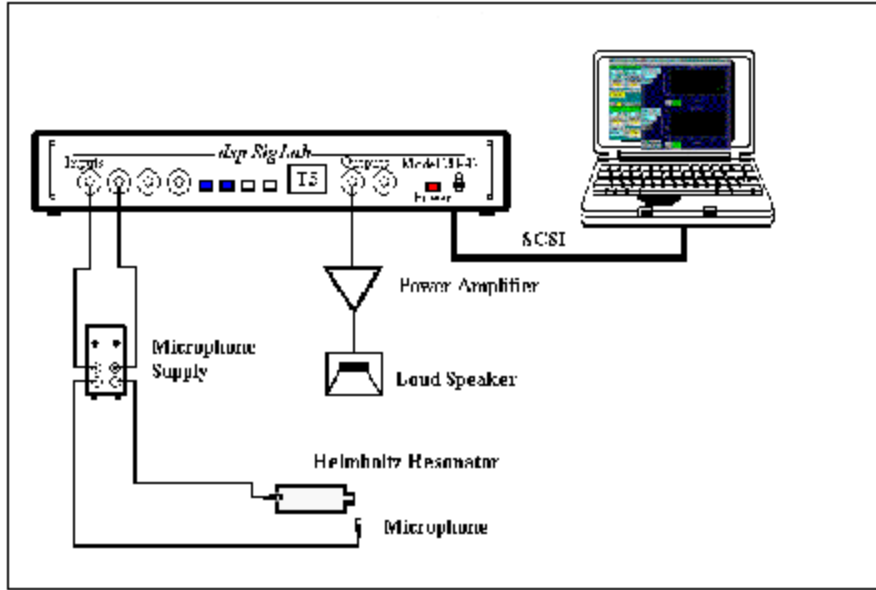
Figure 6.2 Measurement System for Helmholtz Resonators

The resonator was excited by an external source. One microphone was put in the outside and close to the neck of the resonator to measure input, and another microphone was installed in the end of the Helmholtz resonator to measure the inside response. A representative frequency response function for the HR228 Helmholtz resonator is shown in Figure 6.3. The predicted and measured resonant frequencies are listed in Table 6.2.
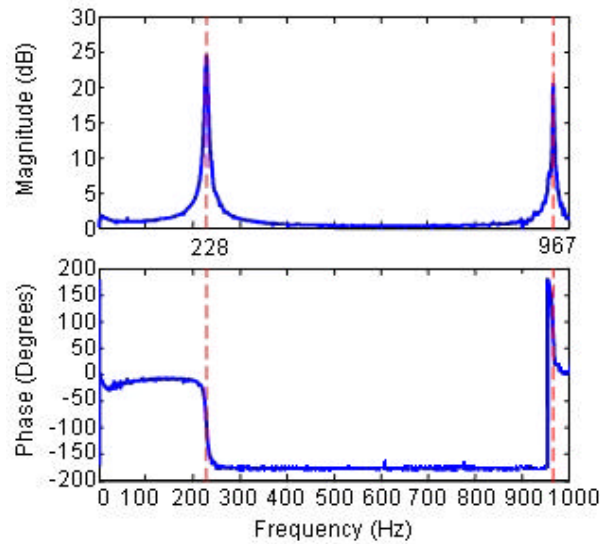
Figure 6.3 Measured FRF of the HR228 Helmholtz Resonator

Table 6.2 Predicted and Measured Resonant Frequencies for Helmholtz Resonators

Group	Measured (Hz)	Predicted by Panton's Model (Hz)	Error (%)	Predicted by Eq. (1.14) (Hz)	Error (%)
HR228	228.4 966.6 1841.3	228.1 984.7 1872.6	0.13 1.87 1.70	228.0 983.5 1870.1	0.18 1.75 1.56
HR398	397.5 1203.8	398.6 1222.9	0.28 1.59	398.0 1211.4	0.13 0.63
HR452	451.3 1351.9	452.9 1401.3	0.35 3.65	452.0 1383.3	0.16 2.32
HR458	457.8 1378.1	458.9 1421.5	0.24 3.15	458.0 1402.6	0.04 1.78

In Figure 6.3 the Helmholtz frequency is 228 Hz, and the second resonance occurs at 967 Hz. From Table 6.2 it can be observed that the maximum error is 0.18% between predicted and measured Helmholtz frequencies. The predicted results are excellent, and the manufactured resonators do not require tuning. Comparing the results predicted by Panton and Miller's model with the results predicted by Eq. (6.13), the Helmholtz frequency predicted by Eq. (6.13) is more accurate than the counterpart predicted by Panton and Miller's model [88]. The results predicted by Panton and Miller's model are generally larger than the results predicted by Eq. (13), especially in the high modes. This is a result of the lumped mass in Panton and Miller's model.

6.1.3   Noise Transmission Control Using Helmholtz Resonators

Several combinations of cylindrical Helmholtz resonators were used to investigate the noise control of the ChamberCore cylinder at low frequencies, especially at the first four targeted frequencies: 228, 398, 452, and 458 Hz. The Helmholtz resonators were located in a place corresponding to the acoustic cavity modes that were to be attenuated and close to the interior walls where there is an area of high modal pressure. The effects of the closely spaced resonators on the noise attenuation were also investigated.

Tests and Test Results

Using the same measurement system and configuration as it was used in Section 4.4, several tests were designed to experimentally investigate the effects of Helmholtz resonators to noise transmission reduction in the ChamberCore cylindrical fairing. The first test did not include any Helmholtz resonators. The intent was to map the acoustic field within the empty payload fairing so that the effect of introducing the Helmholtz resonators in the next tests could be determined.

The second test was designed to experimentally investigate the relationship of closely spaced Helmholtz resonators. Soh *etc.* experimental investigation showed that when the center distance of two identical resonators was greater than a quarter wavelength apart, the sound transmission loss was larger than that of a single resonator, however, when two resonators at same resonant frequency were in close proximity, the two resonators interacted and lead to a decrease in the overall performance compared to that of a single resonator [91]. Two HR228 Helmholtz resonators (referred as to HR228-1 and HR228-2) were selected to study the spacing between two resonators with same-frequency, and the HR228 and HR398 resonators (referred as to HR228-3 and HR398-1, respectively) were selected to study the spacing between two resonators with different-frequency. The relative positions of all resonators are listed in Table 6.3. The measured NRS curves are shown in Figure 6.4 and Figure 6.5.

Table 6.3 Relative Positions of Cylindrical Helmholtz Resonators

		Helmholtz resonator	Coordinates		
			r(mm)	q (degree)	z (mm)
Same-	Case-1	HR228-1	255	315	710
		HR228-2	255	310	710
Frequency	Case-2	HR228-1	255	315	710
		HR228-2	255	225	710
	Case-3	HR228-1	255	315	710
		HR228-2	255	135	710
Different-	Case-4	HR398	255	15	710
		HR228-3	255	20	710
Frequency	Case-5	HR398	255	15	710
		HR228-3	255	105	710
	Case-6	HR398	255	15	710
		HR228-3	255	195	710
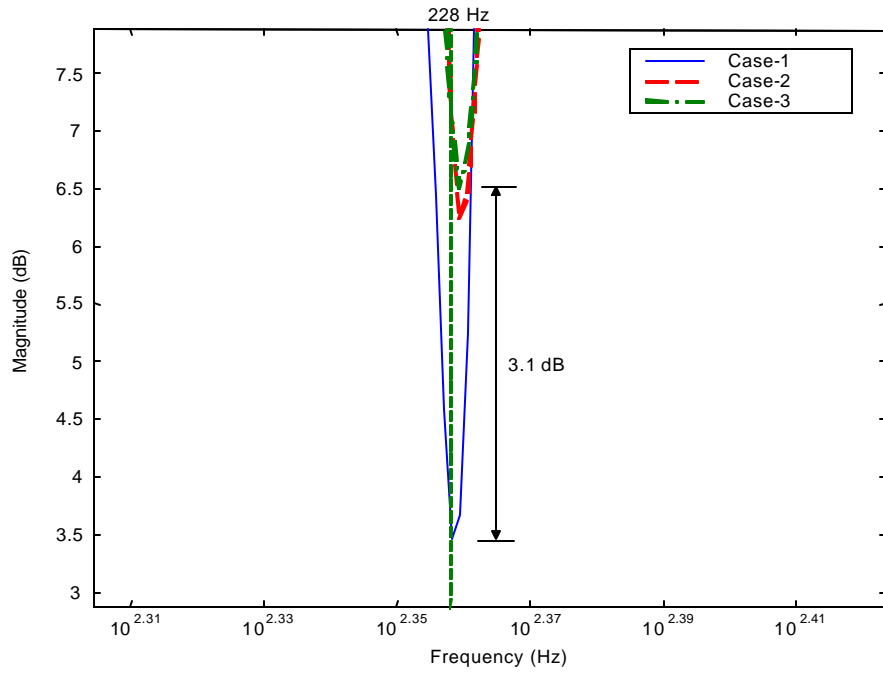
Figure 6.4 Effects on NRS of Two Closely Spaced Identical Resonators
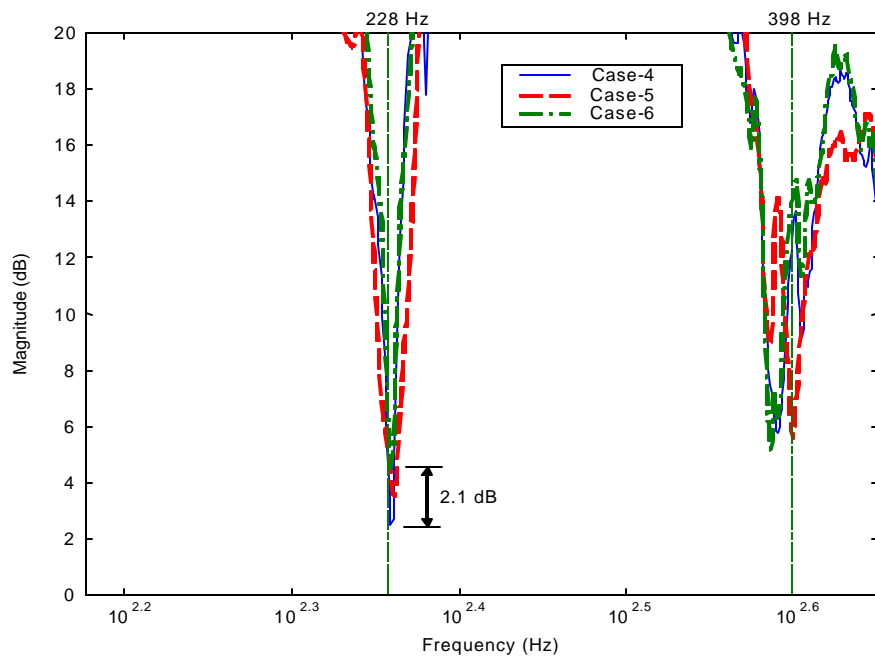
Figure 6.5 Effects on NRS of Two Closely Spaced Different-Frequency Resonators

In Table 6.3, Case-1, Case-2 and Case-3 are used for the same-frequency case, and there are the same r and z coordinates and 5-degree, 90-degree and 180-degree difference in transverse position in Case-1, Case-2, and Case-3, respectively. Case-4, Case-5 and Case-6 are used for the different-frequency case, and there are also the same r and z coordinates and 5-degree, 90-degree and 180-degree difference in transverse position in Case-4, Case-5 and Case-6, respectively. Figure 6.4 is the NRS curves of the ChamberCore cylindrical fairing with resonators HR228-1 and HR228-2 at different relative positions. The Helmholtz resonator HR228-1 was fixed at (r, q, z) = (255 mm, 315 degrees, 710 mm), and the resonator HR228-2 moved over the places of (255 mm, 310 degrees, 710 mm), (255 mm, 225 degrees, 710 mm), and (255 mm, 135 degrees, 710 mm). When the two resonators were installed at 90 degrees apart in Case-2, the NRS is 0.8 larger than that in Case-1. When the two resonators were installed at 180 degrees apart in Case-3, the NRS around the targeted frequency (228 Hz) is 3.1 dB larger than that in Case-1. The optimal positioning of the two closely spaced resonators is 180 degrees apart (Case-3). The same results were observed in a paper by Soh, *ect* [91]. Figure 6.5 is the noise reduction spectrum curves of the ChamberCore cylinder with resonators HR398 and HR228-3. The HR398 Helmholtz resonator was fixed at (r, q, z) = (255 mm, 15 degrees, 710 mm), and the HR228 resonator moved over the places of (255 mm, 20 degrees, 710 mm), (255 mm, 105 degrees, 710 mm), and (255 mm, 195 degrees, 710 mm). It is found that the control of the mode (010) at 398Hz is not so sensitive to the position change between the two closed different-frequency resonators except for the shift in modal frequency. For the control of mode (001) at 228 Hz, the same results are observed as for the identical resonators in Figure 6.4. Also, optimum relative spacing appears to be 180 degrees apart.

The third test was designed to investigate the noise attenuation in a specific frequency using Helmholtz resonators. Because the cylinder represents a 3-D noise control problem, in order to get a uniform noise reduction, there two identical resonators were used for each controlled frequency and both were installed in the vicinity of the two ends of the cylinder and close to the cylindrical walls. Referring back to Figure 4.12, the optimal position for HR228 resonators (corresponding to 001 cavity mode) is the top or bottom side of the cylinder and close to the chamber walls. The optimal position for the HR452 resonators (corresponding to 002 cavity mode) is the two ends or center part of the cavity and close to the cylindrical walls. The HR398 resonator (corresponding to 010 cavity mode) and HR458 resonator (corresponding to

011 cavity mode) were installed in the top end of the cylinder and close the interior shell walls. The optimal circumference position (q) for the two acoustic modes control was especially investigated and experimentally determined. The positions of the Helmholtz resonators in the test are summarized in Table 6.4. In Table 6.4, "Top" means the resonator is in the top part of the cylindrical cavity and "Bottom" means the resonator is in the bottom part of the cylindrical cavity. Because the natural frequencies of the mode 002 and mode 011 are very close, a combination of Helmholtz resonators HR452-Top, HR452-Bottom and HR458-Bottom was used in the control of mode 002 and 011. The measured NRS curves with/without Helmholtz resonators are shown in Figure 6.6, Figure 6.7 and Figure 6.8.

Table 6.4 Position of Each Specific Resonators in the Test

Helmholtz resonator		Coordinates		
		r(mm)	q (Degree)	z (mm)
HR228	-Top	255	300	100
HR228	-Bottom	255	315	710
HR398	-Top	255	30	100
HR398	-Bottom	255	15	710
HR452	-Top	255	210	100
HR452	-Bottom	255	225	710
HR458	-Bottom	255	195	710
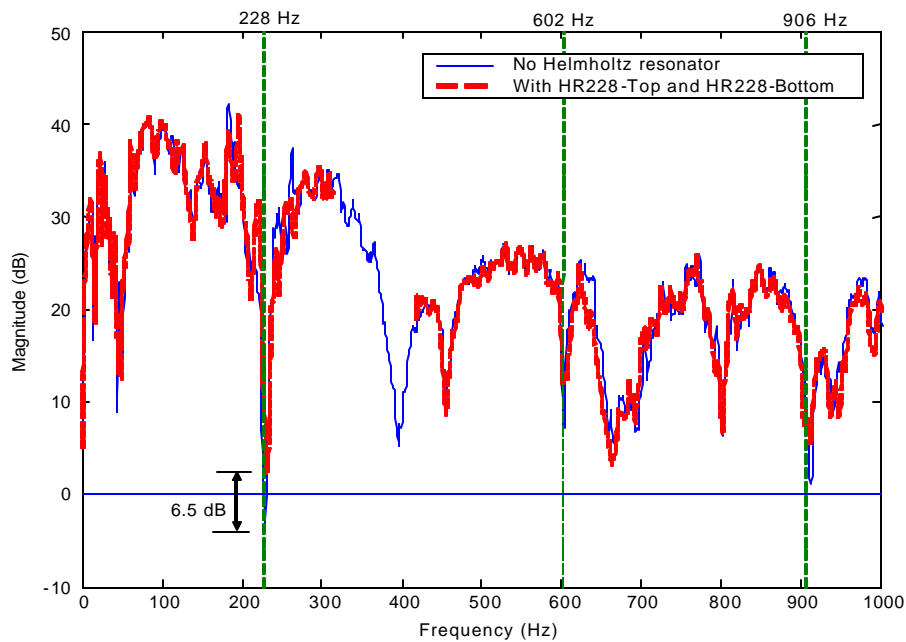
Figure 6.6 Noise Transmission Control Using HR228-Top and HR228-Bottom HRs
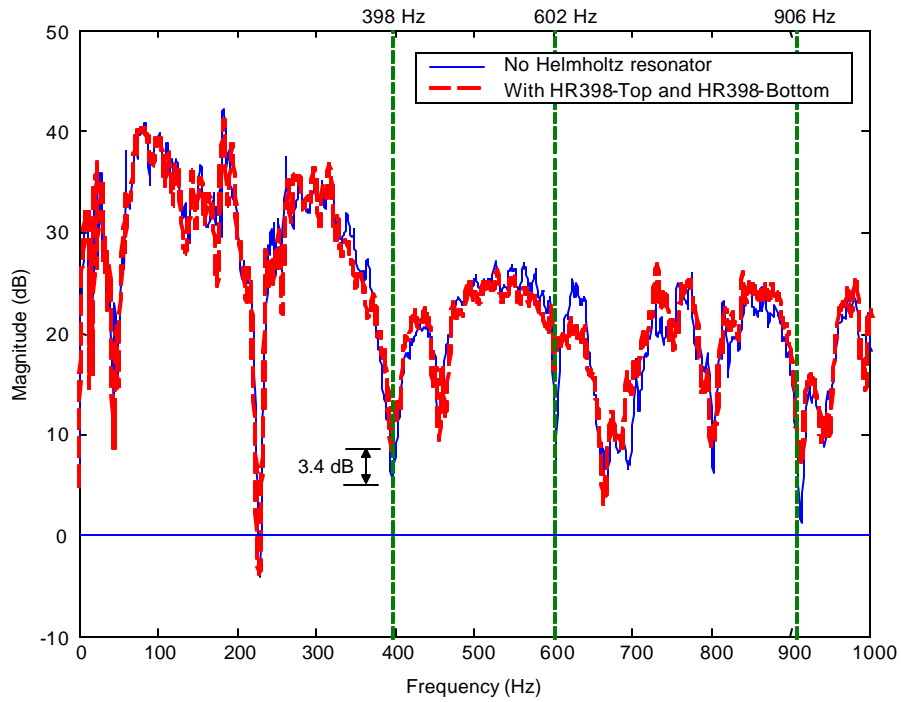
Figure 6.7 Noise Transmission Control Using HR398-Top and HR398-Bottom HRs
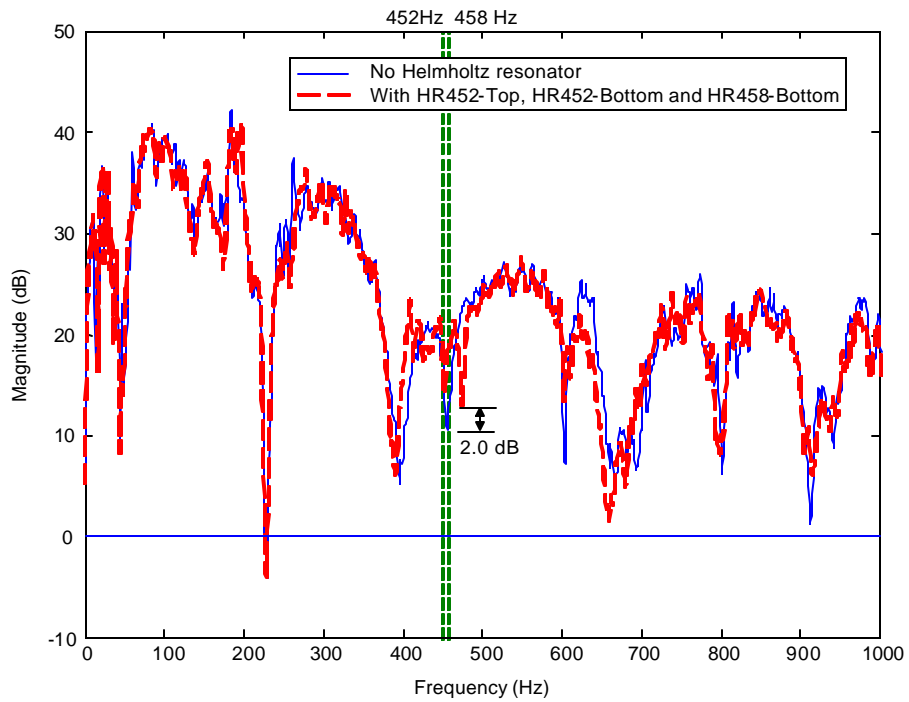
Figure 6.8 Noise Transmission Control Using Two HR452 and One HR458 HRs

Figure 6.6 is the NRS curves of the ChamberCore cylinder with/without two HR228 resonators. The resonators were installed in the positions (255 mm, 300 degrees, 100 mm) and (255mm, 315 degrees, 710 mm). In Figure 6.6 the overall NRS is 6.5 dB improvement around 228 Hz (dot vertical line). The maximum average NRS improvement around 228 Hz occurs in the plane of z =100 mm, and is 9.8 dB.

Figure 6.7 is the NRS curves of the ChamberCore cylinder with/without two HR398 resonators. The resonators were installed in the positions (255 mm, 30 degrees, 100 mm) and (255mm, 15 degrees, 710 mm). In Figure 6.7 the overall NRS improvement is 3.4 dB around 398 Hz (dot vertical line). The maximum average NRS improvement around 398 Hz occurs in the plane of z =100 mm, and is 5.3 dB. There is significant overall NRS increase to be found in the frequency 602 Hz and 906 Hz. They are 9.2 dB and 5.9 dB respectively.

Figure 6.8 is the NRS curves of the ChamberCore cylinder with/without the combination of two HR452 resonators and one HR458 resonator. The two HR452 resonators were respectively installed in the position (255 mm, 210 degrees, 100 mm), (255mm, 225 degrees, 710 mm), and the HR458 resonator was placed at (255mm, 195 degrees, 710 mm). In Figure 6.8 the overall NRS increase is 2.0 dB around 456 Hz (dot vertical line). The maximum average NRS improvement around 456 Hz occurs in the plane of z =340 mm, and is 6.0 dB. The overall NRS improvement is small for this combination. The reason for this may be a result of the 452 Hz resonator at (255mm, 225 degrees, 710 mm) being close the 458 Hz resonator at (255mm, 195 degrees, 710 mm), thus, the two resonators (Helmholtz frequencies are almost same) interact and lead to a decrease in the overall performance.

Finally, based on the above investigation, the combination of two HR228, two HR398, two HR452, and one HR458 Helmholtz resonators were installed inside the ChamberCore cylinder in the positions listed in Table 6.4. The measured NRS curves are given in the Figure 6.9.
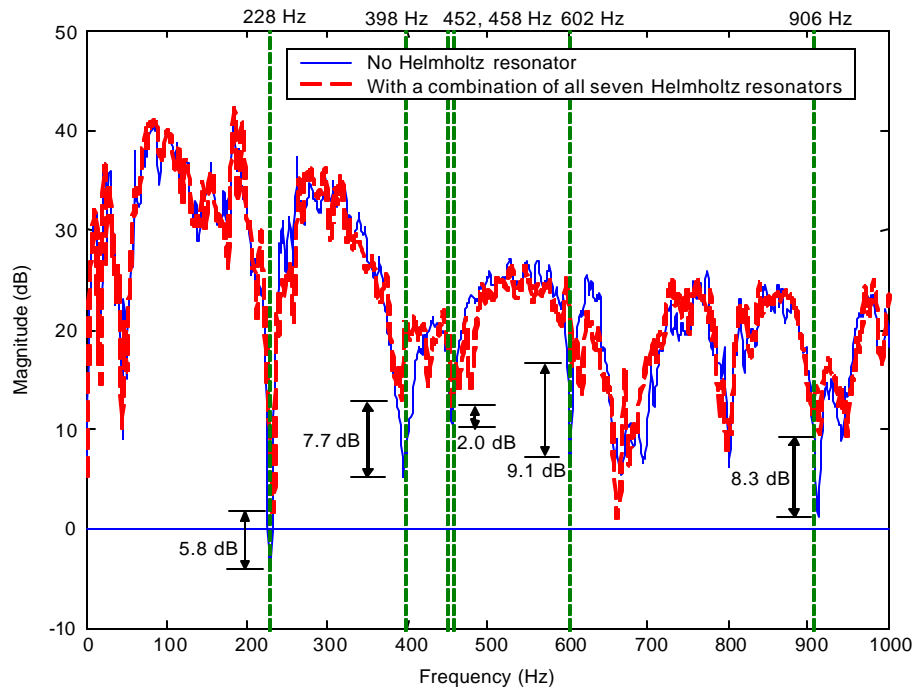
Figure 6.9 Noise Transmission Control Using Seven Cylindrical HRs

In Figure 6.9, the solid curve is the NRS when the cylindrical acoustic cavity is empty, and the dashed curve is the NRS when the combination of resonators is placed in the cavity. The dashed vertical lines depict acoustic resonant frequencies with significant noise improvement. There is a 5.8 dB overall increase around 228 Hz, a 7.7 dB overall increase around 398 Hz, and a 2.0 dB overall increase around 456 Hz. There is also significant improvement: 9.1 dB around 602 Hz and 8.3 dB around 906 Hz due to modal coupling.

6.2   Noise Transmission Control Using Long T-shaped Acoustic Resonators

Short cylindrical Helmholtz resonators have been used to investigate the feasibility of noise control in the ChamberCore cylinder in Section 6.1. The results show that the combination

of well-positioned Helmholtz resonators is effective at attenuating the noise transmission into the ChamberCore cylindrical fairing. However, because the real structure of chambers prohibits the realization of cylindrical Helmholtz resonators, other shapes of acoustic resonators must be considered. In order to effectively use the chambers' volume of the ChamberCore cylinder, a popular device, the long, T-shaped acoustic resonator was considered [95]. Strictly, because of the large geometric dimension ($kl \gg 1$), the resonators used in this section can not be called Helmholtz resonators, and instead of with "acoustic resonators".

A novel and general model for the long T-shaped acoustic resonator was derived, and experimentally verified in Section 6.2.1. The acoustic resonators which respectively have resonant frequency 228 Hz, 398 Hz, 452 Hz, and 458 Hz were also designed and constructed in Section 6.2.1. The noise transmission control results using long T-shaped acoustic resonators were given in Section 6.2.2.

6.2.1   Long T-Shaped Acoustic Resonator: Resonant Frequency and Design

Merkli proposed a model for the calculation of resonant frequencies of the T-tube resonator [89]. However, his model is too special, and can only solve the problems for which the cross sections of the three branches are circular shape with the same diameter. Considering that the shape of cross-section may be trapezoid, and the cross-sectional area of the three branches may be different, it is need to develop a more general model for resonator design and resonant frequency calculation for the long T-shaped acoustic resonator. As in Section 6.1.1, wave propagation theory is also used to derive the general model here.

A long T-shaped acoustic resonator is shown in Figure 6.10. All boundaries are assumed to be rigid, and the axial cross-section of each branch is assumed to be uniform. There are no sources inside the resonator, and the effects of mean flow are neglected for this problem. The fluid contained in the resonator is assumed to be stationary, homogeneous, inviscid and non-heat conducting. The temperature distribution in the resonator is assumed to be 75°F everywhere. The resonator consists of three branches: Branch 1, Branch 2, and Branch 3 as labeled in Figure 6.10. The Branch 1 is perpendicular to Branch 2 and Branch 3. Because the nature dynamic properties

114

of the resonator do not change with the direction of wave propagation and the coordinate system, it is assumed that the incident plane wave is from the opening of Branch 1, and that it transmits down to Branch 2 and Branch 3. Thus, the axis origin is set at the outside opening end. In Fig. 2, L_1, L_2, and L_3 are the effective length of Branch 1, Branch 2, and Branch 3, respectively, S_1, S_2, and S_3 are the cross sectional area of the Branch 1, Branch 2, Branch 3, respectively, $Z_1(x_1)$, $Z_2(x_2)$, and $Z_3(x_2)$ are the acoustic impedance at position x_1 of the Branch 1, and position x_2 of Branch 2 and Branch 3, respectively.
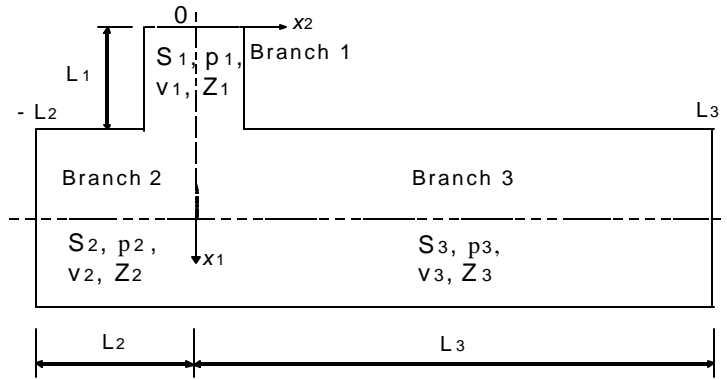
Figure 6.10 Long T-Shaped Acoustic Resonator

The first boundary condition at the junction is that the pressure is single value,

$$p_1(L_1) = p_2(0) = p_3(0) . \tag{6.23}$$

The second boundary condition at the junction is that the continuity equation holds:

$$v_1(L_1)rS_1 = v_2(0)rS_2 + v_3(0)rS_3 , \tag{6.24}$$

where v is the acoustic velocity, r the air density. The third, forth, and fifth boundary conditions are the acoustic impedance boundary conditions:

$$Z_1(0) = 0 , \tag{6.25}$$

$$Z_2(-L_2) = \infty , \tag{6.26}$$

$$Z_3(L_3) = \infty . \tag{6.27}$$

In terms of the acoustic impedance, $Z = r/vS$, Eqs. (6.23) and (6.24) can be combined to give

$$\frac{1}{Z_1(L_1)} = \frac{1}{Z_2(0)} + \frac{1}{Z_3(0)} . \tag{6.28}$$

From Eqs. (6.5) and (6.6) the acoustic impedance of $Z_1(L_1)$, $Z_2(0)$, and $Z_3(0)$ can be expressed as

$$Z_1(L_1) = \frac{Z_1(0) - j\frac{rc}{S_1}\tan(kL_1)}{1 - j\frac{S_1}{rc}Z_1(0)\tan(kL_1)} , \tag{6.29}$$

$$Z_2(0) = \frac{Z_2(-L_2) - j\frac{rc}{S_2}\tan(kL_2)}{1 - j\frac{S_2}{rc}Z_2(-L_2)\tan(kL_2)} , \tag{6.30}$$

$$Z_3(0) = \frac{Z_3(L_3) + j\frac{rc}{S_3}\tan(kL_3)}{1 + j\frac{S_3}{rc}Z_3(L_3)\tan(kL_3)} . \tag{6.31}$$

Substituting Eqs. (6.25), (6.26), and (6.27) into Eqs. (6.29), (6.30) and (6.31) yields

$$Z_1(L_1) = -j\frac{rc}{S_1}\tan(kL_1) , \tag{6.32}$$

116

$$Z_2(0) = \frac{1}{j\dfrac{S_2}{\boldsymbol{r}c}\tan(kL_2)}, \tag{6.33}$$

$$Z_3(0) = \frac{1}{j\dfrac{S_3}{\boldsymbol{r}c}\tan(kL_3)}. \tag{6.34}$$

Substituting Eqs. (6.32), (6.33) and (6.34) into (6.28), and simplifying, the eigenfunction for the long T-shaped acoustic resonator can be obtained as:

$$S_1 \cot(kL_1) = S_2 \tan(kL_2) + S_3 \tan(kL_3), \tag{6.35}$$

where $k=?/c=2\boldsymbol{p}\,f/c$ is the wavenumber of sound. Note that there are no limitations given during the derivation of Eq. (6.35). Therefore, the area of the three branches may be same or not, and the branch lengths may be comparable to resonance wavelength or longer. When the area of the three branches is the same and the effective lengths of the three branches satisfy: $L_1=l_{\text{eff}}$ and $L_2=L_3=L_{\text{eff}}$, the Merkli's formula can be obtained from Eq. (6.35):

$$\cot(kl_{\text{eff}}) = 2\tan(kL_{\text{eff}}), \tag{6.36}$$

where l_{eff} is the effective length of Branch 1, and L_{eff} is the effective length for Branch 2 and Branch 3 in Merkli's formula.

Equation (6.35) can be used for two purposes. First it is used to calculate resonant frequencies for the long T-shaped acoustic resonators, and second to design the long T-shaped acoustic resonators. The resonant frequencies can be found from the intersection of abscissa axis with the function $F(f) = S_2/S_1 \tan(2\boldsymbol{p}\,fL_1/c)\tan(2\boldsymbol{p}\,fL_2/c) + S_3/S_1 \tan(2\boldsymbol{p}\,fL_1/c)\tan(2\boldsymbol{p}\,fL_3/c)$. The first root is the so-called Helmholtz frequency, and succeeding resonances are the higher mode frequencies.

Design of Long T-Shaped Acoustic Resonators

In order to study the problems of design and end corrections, detailed geometric dimensions of the long T-shaped acoustic resonator are given in Figure 6.11. In Figure 6.11 (A), the three branches are cylindrical tubes, L_{B1_1} and L_{B1_2} are the smallest and largest heights of the Branch 1, L_{B2} and L_{B3} are the lengths of Branch 2 and Branch 3, respectively. The shaded part is the junction area. In Figure 6.11 (B), the Branch 1 may be rectangular or circular cross section, and the Branch 2 and Branch 3 are the rectangular cross section. , L_{B1}, L_{B2} and L_{B3} are the lengths of Branch 1, Branch 2 and Branch 3, respectively.
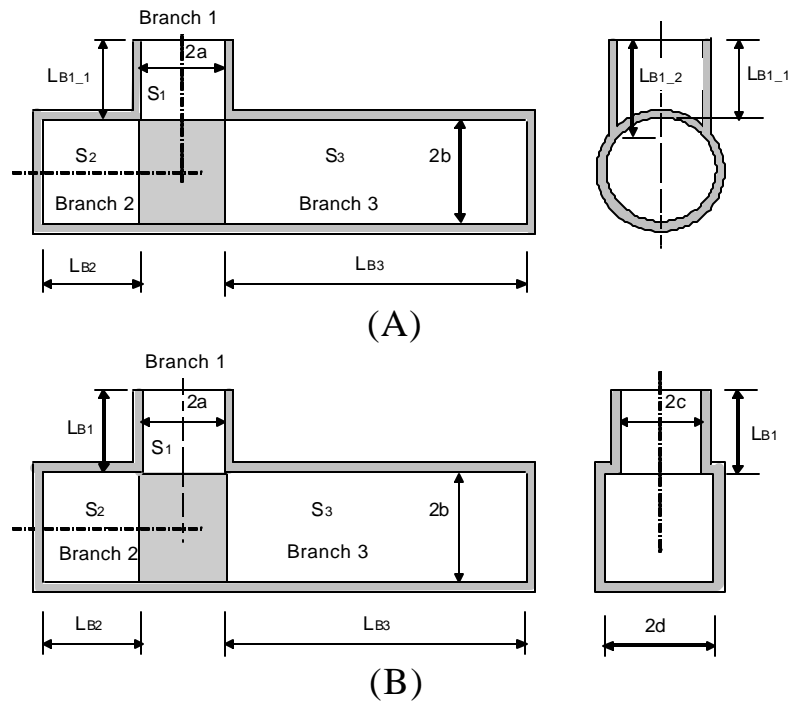
Figure 6.11 Geometry of the T-shaped Acoustic Resonator

In Merkli's model the lengths of Branch 2 and Branch 3 are assumed to be equal. This assumption makes it impractical for designing integrated acoustic resonators into the ChamberCore cylinder. In order to control the targeted cavity modes, the resonators must be placed in an optimal position that corresponds to the controlled modes. However, the assumption of equal lengths limits the freedom of selecting the position in a finite cylinder. The intended model for the T-shaped acoustic resonator theory should permit any one variable of S_1, S_2, S_3,

L_{B1}, L_{B2}, and L_{B3} to be calculated for a designated resonant frequency. Another shortcoming of Merkli's model concerns the length correction calculation. He defined a "common intersection volume" formed by intersecting the three equal cross-sectional branches of the acoustic resonator. Then, this volume was transformed geometrically into cylinders of the same radius as the basic tubes with the length correction. The rule for the calculation of length correction is based on a linear ratio (weight) of each branch length in the three branch lengths (see Eq. (6.43)-(6.45)). The length correction in his model does make the design of T-shaped acoustic resonators complex because the lengths are coupled to each other in Eq. ((6.37)-(6.39)), and can only be solved by numerical methods. A simple and reasonable approach for the design of T-shaped acoustic resonators and calculation of end correction is needed.

For the purpose of noise control in the ChamberCore cylindrical fairing there are two conditions which should be considered in the design of T-shaped acoustic resonators. The first is saving the space occupied by resonators, and the second is placing resonator in an optimal position. The first consideration dictates that the length of Branch 1 is as short as possible, and the second consideration requires that either L_{B2} or L_{B3} is determined to fit an optimal position corresponding to the particular controlled cavity mode. Assuming that L_1 and L_2 are given as well as the areas of the three branches, then the following design equations permit one to solve L_3.

$$
L_3 = \frac{a \tan\left(\dfrac{S_1}{S_3}\cot(kL_1) - \dfrac{S_2}{S_3}\tan(kL_2) \right) + (i-1)\boldsymbol{p}}{k} ,
\qquad (6.37)
$$

where i (=1, 2, 3, 4, …) is the order number of the acoustic resonator mode whose resonant frequency is given. In order to control the low frequency cavity mode of the ChamberCore fairing at 228 Hz, the order number of acoustic resonator mode is set to one. In order to control other high frequency cavity modes, the order number of the acoustic resonator mode may be larger than one. The reason for this is that if k is larger ($k=2\boldsymbol{p}f/c$) and $i=1$, L_3 will become very small.

End Corrections of Long T-Shaped Acoustic Resonators

End corrections are very important in resonator design and in solving for resonant frequencies. Especially, the end corrections always play a decisive role in analyzing the acoustic performance of the T-shaped resonators which include small geometric dimensional branches. As described in Section 6.1, the end corrections are well established and extensively documented for classical Helmholtz resonators. However, for T-shaped acoustic resonators, the theory is not so mature yet. In this section, three new models for the calculation of end corrections will be proposed and compared with Merkli's model.

1. Model 1 (Merkli's model)

When the three branches of T-shaped resonators have the same circular cross-sections with radius a, Merkli's model for the calculation of end correction is:

$$L_1 = L_{B1\_1} + \Delta L_{1\_1} + \Delta L_{1\_2} + \Delta L_c , \tag{6.38}$$

$$L_2 = L_{B2} + \Delta L_{2\_1} + \Delta L_{2\_2} , \tag{6.39}$$

$$L_3 = L_{B3} + \Delta L_{3\_1} + \Delta L_{3\_2} , \tag{6.40}$$

where $?L_{1\_1}$, $?L_{1\_2}$ and $?L_{1\_3}$ are the end corrections induced by the common volume for Branch 1, Branch 2, and Branch 3, respectively, and $?L_{2\_1}$, $?L_{2\_2}$ and $?L_{2\_3}$ are the end corrections induced by the intersection volume for Branch 1, Branch 2, and Branch 3, respectively [Merkli's model]. $?L_c$ is the end correction of the opening end of Branch 1. They are calculated by the following equations.

$$\Delta L_{1\_1} = \Delta L_{1\_2} = \Delta L_{1\_3} = a(1 - \frac{8}{3\boldsymbol{p}}) , \tag{6.41}$$

$$\Delta L_c = \begin{cases} \dfrac{8a}{3\boldsymbol{p}} & (2\text{ka} < 1) \\[2ex] \dfrac{c^2}{\boldsymbol{p}^3 f^2 a} & (\text{ka} \gg 1) \end{cases}, \tag{6.42}$$

$$\Delta L_{1\_2} = \frac{16a}{3\boldsymbol{p}} \frac{L_{B1\_1}}{L_{B1\_1} + L_{B2} + L_{B3}}, \tag{6.43}$$

$$\Delta L_{2\_2} = \frac{16a}{3\boldsymbol{p}} \frac{L_{B2}}{L_{B1\_1} + L_{B2} + L_{B3}}, \tag{6.44}$$

$$\Delta L_{3\_2} = \frac{16a}{3\boldsymbol{p}} \frac{L_{B3}}{L_{B1\_1} + L_{B2} + L_{B3}}. \tag{6.45}$$

2. Model 2 (Hybrid Rayleigh's Impedance)

Model 2 is a novel model for the calculation of end corrections and effective lengths. In this model, the Branch 1 is considered as the neck of the acoustic resonator with a circular tube of radius a. Its effective length may be calculated as

$$L_1 = L_{B1\_1} + \Delta L_{\text{out}} + \Delta L_{\text{out}}, \tag{6.46}$$

where $?L_{\text{out}}$ is the interior and outer end correction, which is calculated by Rayleigh's correction model [85]

$$\Delta L_{\text{out}} = \frac{8}{3\boldsymbol{p}} a. \tag{6.47}$$

The end correction of Branch 2 and Branch 3 are based on acoustic impedance. Because the acoustic impedance has an inverse ratio relationship with the area, the volume V_{junct} of the junction part (shaded part in Fig. 3 A and B) will be partitioned as a weighted area, and then the obtained volume is transformed geometrically into the branches of same area as the

basic branches with end corrections DL_2 and DL_3. The formulas for the calculation of the end corrections of Branch 2 and Branch 3 are, respectively:

$$V_{\text{junct}} = (S_2 + S_3)a,$$ (6.48)

$$\Delta L_2 = \frac{2V_{\text{junct}}}{S_2 + S_3},$$ (6.49)

$$\Delta L_3 = \frac{2V_{\text{junct}}}{S_2 + S_3}.$$ (6.50)

Considering the special case that the cross-sectional areas of Branch 2 and Branch 3 are the same, the end corrections of the Branch 2 and branch 3 are set to $2a$ (see Fig 3 A and B). Therefore, the factor 2 is included in Eq. (6.49) and Eq. (6.50).

3. Model 3 (Simplified Impedance)

Model 3 is also a novel model for the calculation of end corrections and effective lengths. In order to simplify the design, it is desired that the formulas for the calculation of end corrections be as simple as possible. Since the interior end correction and the outer end correction are in opposite directions, it may be more accurate to neglect both end corrections [88]. In this model, there is no end correction for Branch 1, and the effective length of Branch 1 is the smallest length of Branch 1. The effective length of Branch 2 and Branch 3 are the same as for Model 2.

$$L_1 = L_{B1\_1},$$ (6.51)

$$L_2 = L_{B2} + \Delta L_2,$$ (6.52)

$$L_3 = L_{B3} + \Delta L_3.$$ (6.53)

4. Model 4 (Alternate Simplified Impedance)

Model 4 is also a novel model for the calculation of end corrections and effective lengths. In this model, the effective length of Branch 2 and Branch 3 are the same as for Model 2 and Model 3. The effective length of Branch 1 is defined as the mean of the smallest and largest branch lengths L_{B1_1} and L_{B1_2}, respectively.

$$L_1 = \frac{L_{B1\_1} + L_{B1\_2}}{2} .$$

(6.54)

Since in model 3 and Model 4, the cross-sectional shape can be anything, there are no limitations for them. The only thing that needs to mention here again is that the maximum cross-sectional geometric dimension of the resonators must be much smaller than the wavelength of the interested sound, which is required by the plane wave propagation principles used in this chapter.

Validation of the End Correction Models

Three long T-shaped acoustic resonators (AR) were constructed from hard-walled PVC-tubing and fittings for the purpose of experimental validation end correction models. They are referred as to AR-1, AR-2, AR-3, respectively. In order to match the requirement of Merkli's model, the three branches of the resonators use circular cross-sections with the same radius. The AR-1 was constructed by PVC tubes with radius 20.2 mm. The AR-2 and AR-3 were made from PVC tubes whose radius is 13.2 mm. The geometric dimensions of the resonators are listed in Table 6.5. An experiment was designed to measure the frequency response of the acoustic resonators. The measurement system is the same as shown in Figure 6.2. Representative measured bode plots for AR-2 are shown in Figure 6.12. The measured and predicted natural frequencies for all of the resonators between 0-1000 Hz are given in Table 6.6. The error between measured and predicted resonant frequencies is also given.

Table 6.5 Geometric Dimensions of Three Long T-Shaped Acoustic Resonators

		AR-1	AR-2	AR-3
Branch 1	Radius: a (mm)	20.2	13.2	13.2
	Area: S_1 (mm^2)	1281.9	547.4	547.4
	Length: L_{B1_1} (mm)	38.0	5.0	4.2
	Length: L_{B1_2} (mm)	58.2	18.2	17.4
Branch 2	Radius: b (mm)	20.2	13.2	13.2
	Area: S_2 (mm^2)	1281.9	547.4	547.4
	Length: L_{B2} (mm)	71.5	32.8	352.4
Branch 3	Radius: b (mm)	20.2	13.2	13.2
	Area: S_3 (mm^2)	1281.9	547.4	547.4
	Length: L_{B3} (mm)	634.0	680.8	352.4
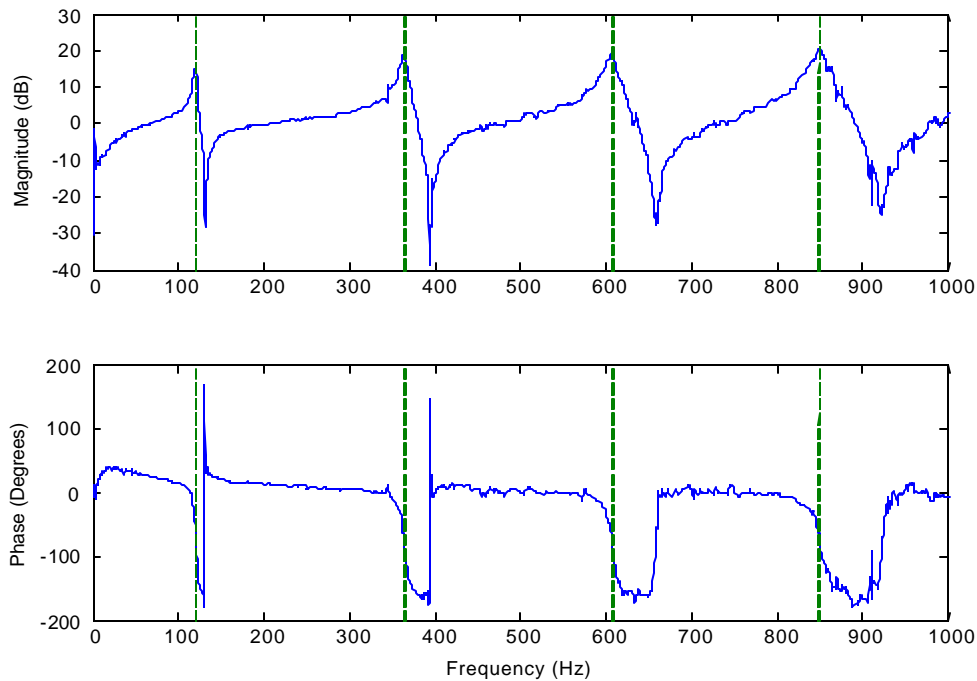
Figure 6.12 Measured FRF of the AR-2

From Figure 6.12 it can be observed that AR-2 has four resonant frequencies in the frequency band [0, 1000] Hz: 121.3 Hz, 366.6 Hz, 613.1 Hz, and 858.8 Hz.

Table 6.6 Measured and Predicted Frequencies of T-Shaped Acoustic Resonators

Group	Measured (Hz)	Model 1 (Hz)	Error (%)	Model 2 (Hz)	Error (%)	Model 3 (Hz)	Error (%)	Model 4 (Hz)	Error (%)
	122.2	117.4	3.9	116.5	4.7	124.2	1.6	121.9	0.2
	364.4	330.5	9.3	315.5	13.4	361.3	0.9	348.0	4.5
AR-1	568.1	501.9	11.7	480.0	15.5	547.7	3.6	519.0	8.6
	720.9	698.7	3.1	693.3	3.8	709.2	1.6	701.5	2.7
	926.9	928.3	0.2	927.8	0.1	927.8	0.1	927.8	0.1
	121.3	119.5	1.4	117.4	3.2	121.2	0.1	120.2	0.9
	366.6	357.6	2.5	349.2	4.7	364.2	0.7	360.3	1.7
AR-2	613.1	593.1	3.3	570.6	6.9	606.8	1.0	599.0	2.3
	858.8	823.1	4.2	850.8	0.9	848.9	1.1	838.8	2.9
AR-3	223.8	214.9	4.0	197.9	11.6	223.3	0.2	215.3	3.8
	675.9	637.9	5.6	585.3	13.4	669.4	1.0	675.9	4.7
Average			4.5		7.1		1.1		2.9

As shown in Table 6.6, the end corrections for Model 3 give the best results for the prediction of resonant frequencies under 1,000 Hz for long T-shaped acoustic resonators, and the end corrections for Model 2 give the worst results. The end corrections for Merkli's model give much worse results than those given by Model 3 and Model 4. The reason for this may be that the end corrections for Merkli's model are only based on the geometric considerations, and does not take into account the acoustic effects.

From the results, Model 3 is found to be the best and yet has the simplest equations. The maximum errors of the first and second predicted resonant frequencies are only 1.6% and 1.0%, respectively. This model also predicts the resonant frequencies of higher modes very well, as seen by the average error (1.1%) given in the last row. Consequently, Model 3 will be used to design the acoustic resonators for the noise transmission control of the ChamberCore structure.

Design and Construction of the Long T-Shaped Acoustic Resonators

In order to control the first four cavity modes: (001) at 228 Hz, (010) at 398 Hz, (002) at 452 Hz, and (011) at 458 Hz, the long T-shaped acoustic resonators, which respectively include the resonant frequencies of 228 Hz, 398 Hz, 452 Hz, or 458 Hz, were designed using Eq. (6.37) and Eqs. (6.51)-(6.53), and they were referred to as AR228, AR398, AR452, and AR458,

respectively. The AR228 was designed with (i=1) in Eq. (6.37), and AR398, AR452 and AR458 were designed with (i=2) in Eq. (6.37). The geometric dimensions of the designed resonators are given in Table 6.7.

Table 6.7 Geometric Dimensions of Designed T-Shaped Acoustic Resonators

Group		AR228		AR398		AR452	AR458
		-Top	-Bottom	-Top	-Bottom	-Top	-Bottom
Branch 1	Radius: a (mm)	13.2	13.2	13.2	13.2	13.2	13.2
	Area: S_1 (mm^2)	547.4	547.4	547.4	547.4	547.4	547.4
	Length: L_{B1_1} (mm)	10.0	10.0	10.0	10.0	10.0	10.0
Branch 2	Radius: b (mm)	20.2	20.2	20.2	20.2	20.2	20.2
	Area: S_2 (mm^2)	1281.9	1281.9	1281.9	1281.9	1281.9	1281.9
	Length: L_{B2} (mm)	63.2	43.2	63.2	43.2	63.2	43.2
Branch 3	Radius: b (mm)	20.2	20.2	20.2	20.2	20.2	20.2
	Area: S_3 (mm^2)	1281.9	1281.9	1281.9	1281.9	1281.9	1281.9
	Length: L_{B3} (mm)	328.7	328.9	598.8	599.9	519.4	513.5

In Table 6.7, "Top" means the opening of the resonator will close to the top part of the cylinder, and "Bottom" means the opening of the resonator will close to the bottom part. The designed long T-shaped acoustic resonators were constructed by commercially available circular cross-sectional PVC-tubing and fittings (see Figure 6.13). The measured transfer function for each resonator is shown in Figure 6.14 - Figure 6.19. The measured and predicted resonant frequencies under 1,000Hz are listed in Table 6.8.

Figure 6.13 Picture of the AR398
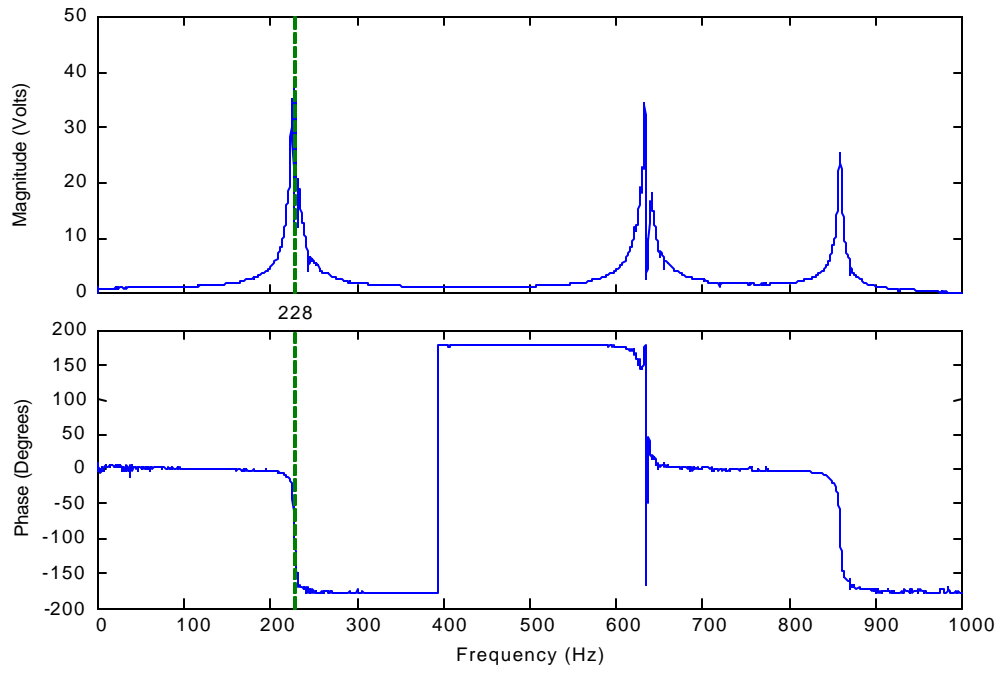
Figure 6.14 Measured FRF of the AR228-Top
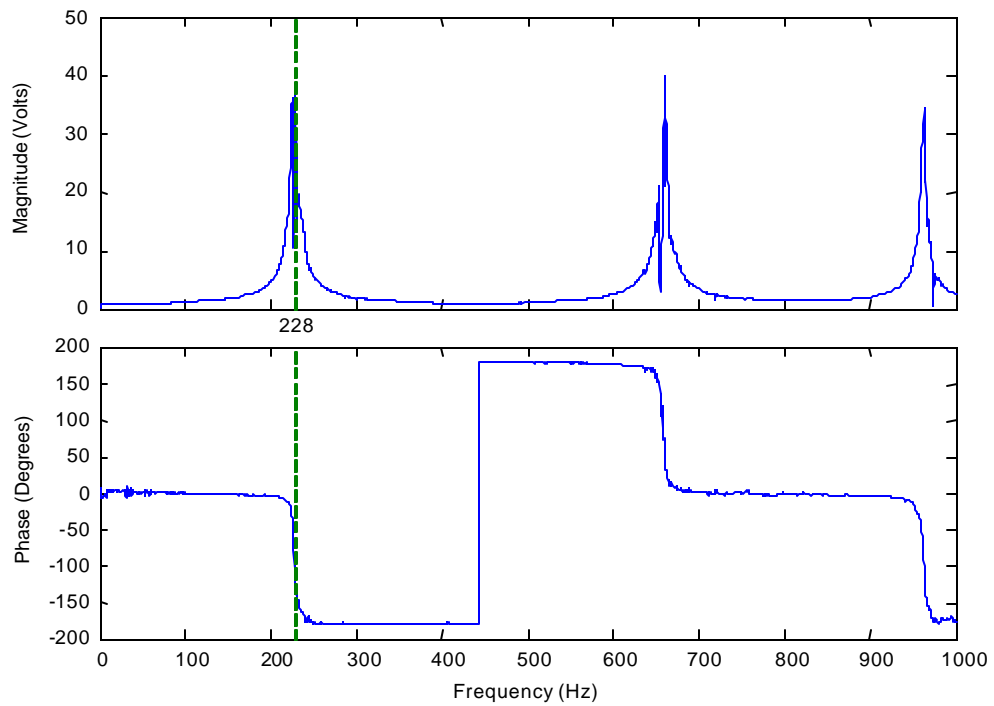
Figure 6.15 Measured FRF of the AR228-Bottom

127
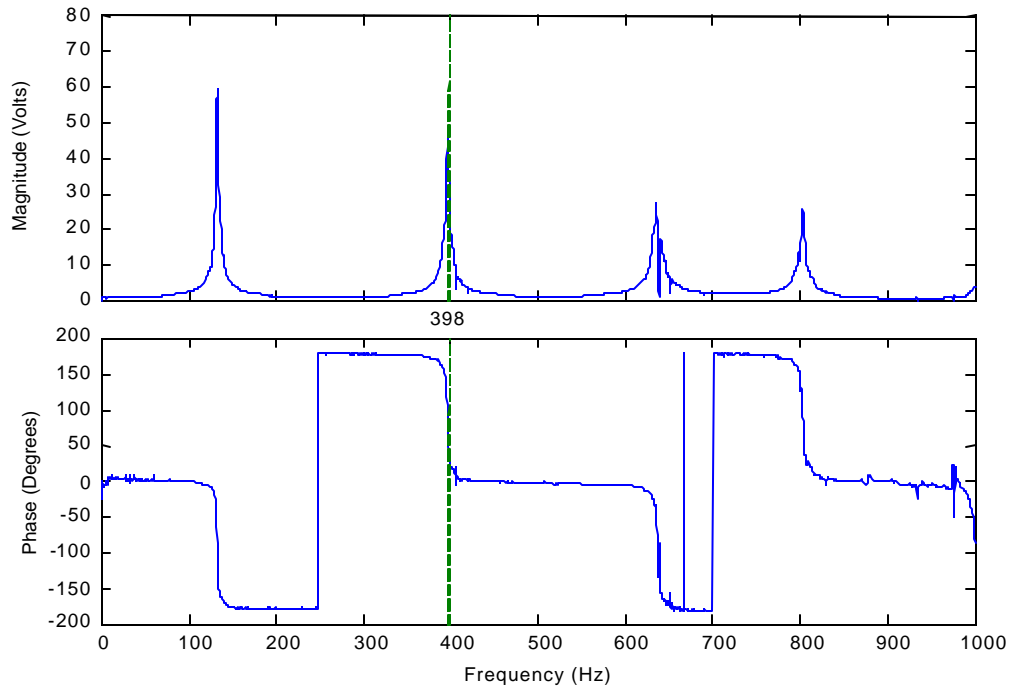
Figure 6.16 Measured FRF of the AR398-Top
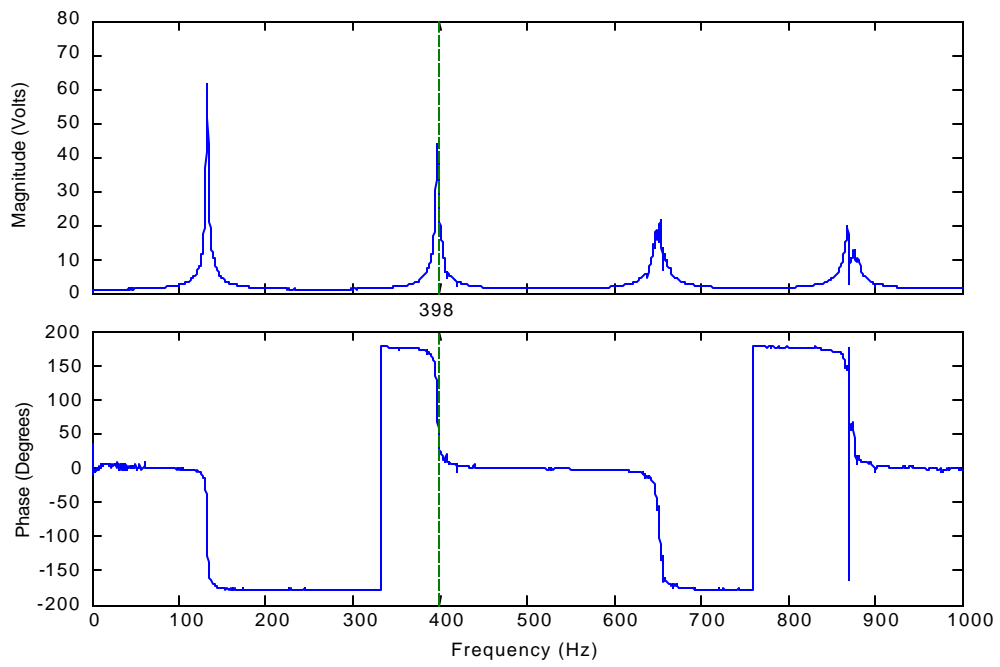
Figure 6.17 Measured FRF of the AR398-Bottom
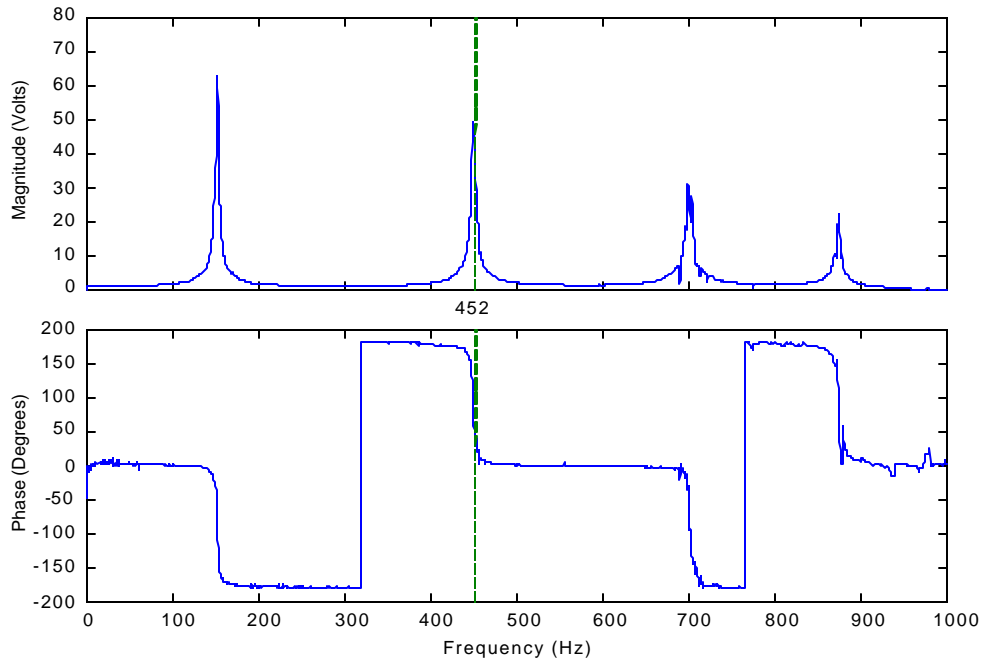
Figure 6.18 Measured FRF of the AR452-Top
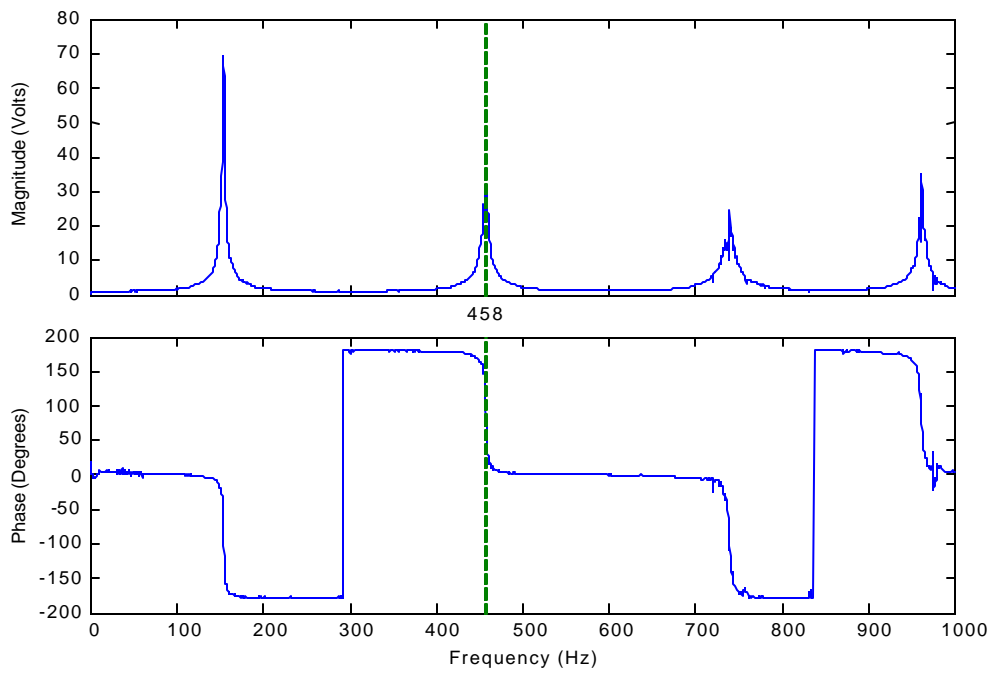
Figure 6.19 Measured FRF of the AR458-Bottom

129

Table 6.8 Measured and Predicted Frequencies of Designed Acoustic Resonators

Group		Measured (Hz)	Predicted (Hz)	Error (Hz)	Error (%)
AR228	-Top	227.5	228.0	-0.5	0.22
		632.8	647.3		2.29
		858.8	806.3		6.11
	-Bottom	228.4	228.0	+0.4	0.18
		660.3	666.5		0.94
		962.8	926.3		3.79
AR398	-Top	132.8	133.3		0.38
		396.6	398.0	-1.4	0.35
		635.3	645.0		1.53
		803.4	774.3		3.62
		-	963.8		-
	-Bottom	132.5	133.1		0.45
		397.2	398.0	-0.8	0.20
		653.1	655.6		0.38
		868.4	866.0		0.28
AR452	-Top	151.6	151.8		0.13
		450.3	452.0	-1.7	0.38
		698.8	703.4		0.66
		873.4	825.9		5.44
AR458	-Bottom	153.1	153.5		0.26
		458.8	458.0	+0.8	0.17
		739.1	744.6		0.74
		961.6	927.9		3.50

As shown in Table 6.8, the maximum error at designed frequencies is 0.38% (-1.7Hz). The designed results were excellent, and did not require tuning.

6.2.2 Noise Transmission Control Using Long T-Shaped Acoustic Resonators

The goal of using long T-shaped acoustic resonators in the ChamberCore cylindrical fairing is to obtain a 3 dB improvement in the noise reduction spectrum in the first four targeted frequencies: 228, 398, 452, and 458 Hz with a combination of acoustic resonators. The positions of the long T-shaped acoustic resonators will be based on the results listed in Table 6.4. The acoustic resonators: AR228-Top, AR228-Bottom, AR398-Top, AR398-Bottom, AR452-Top, AR458-Bottom are installed in the position (z, θ) =(85 mm, 300 degrees), (65 mm, 315 degrees),

(85 mm, 30 degrees), (65 mm, 15 degrees), (85 mm, 220 degrees), and (65 mm, 195 degrees), respectively, and close to the cylindrical walls. The test system is the same as that used in Section 4.4. The test results of the NRS when all designed long T-shaped acoustic resonators were installed inside the cylindrical cavity compared with the no control results are shown in Figure 6.20.
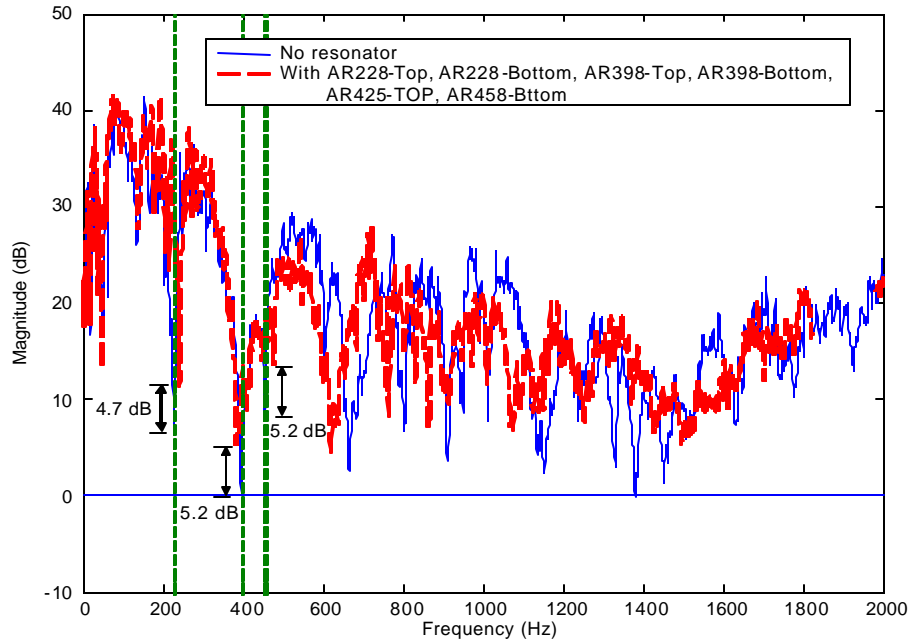
Figure 6.20 Noise Transmission Control Using Six Long T-Shaped ARs (1)

In Figure 6.20, there is significant noise control in not only the targeted frequencies but also in the high frequency band. The NRS increase is 4.7 dB, 5.2 dB, 5.3 dB and 5.3 dB at 228 Hz, 398 Hz, 452 Hz and 458 Hz, respectively. There is significant noise attenuation and resonant frequency shifts over all frequency bands because of the very strong coupling between the acoustic cavity and the long T-shaped acoustic resonators. The maximum improvement in the NRS occurs in the area of 1050 Hz and 1450 Hz. The maximum noise reduction at targeted frequencies occurs at the plane of $z = 480$ mm, and is shown in Figure 6.21. The improvement of

averaged NRS in this plane is 4.7 dB, 7.9 dB, 7.2 dB, and 7.2 dB for the cavity resonance at 228 Hz, 398 Hz, 452 Hz, and 458 Hz, respectively.
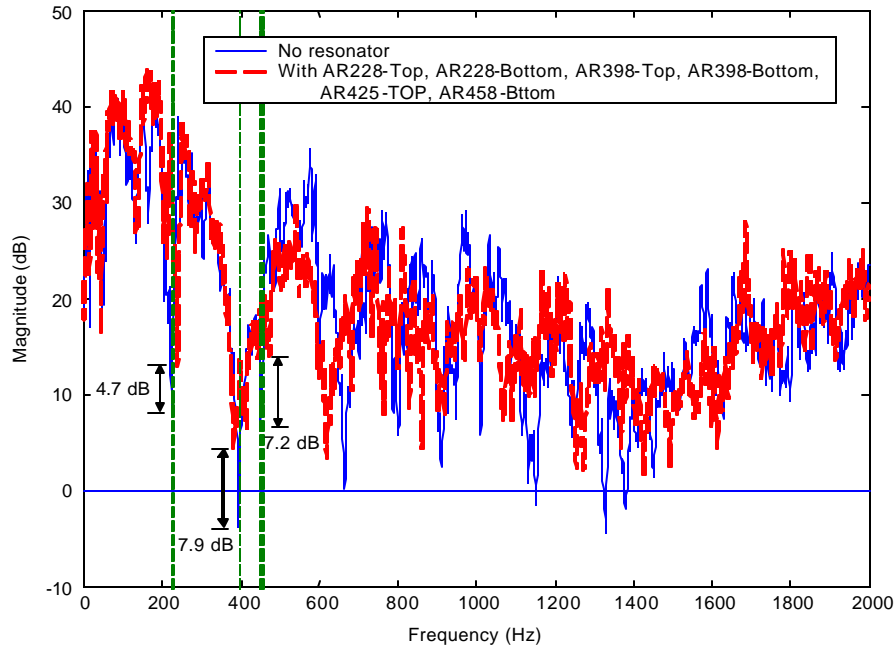
Figure 6.21 Noise Transmission Control Using Six Long T-Shaped ARs (2)

6.3   Noise Transmission Control Using Chamber-Based T-Shaped Acoustic Resonators

A novel and general model for the calculation of resonant frequencies of the long T-shaped acoustic resonators has been successfully derived in Section 6.2. A new and general long T-shaped acoustic resonator design equation and design schemes have also been developed. Three new end correction models (Model 2 through Model 4) based on the consideration of acoustics have been proposed and experimentally validated. Model 3 gives excellent results for frequency prediction and resonator design. All the new models proposed in Section 6.2 are no limitations for the cross-sectional shape end length of the three branches. The results from using

well-positioned, long, T-shaped acoustic resonators to control the noise transmission into the ChamberCore cylinder show that there is significant noise attenuation over all frequency bands. The goal of producing 3 dB of control in the first four targeted modes was exceeded by at least 1.7 dB.

The next steps for the noise transmission control of the ChamberCore cylinder using acoustic resonators will be to fabricate the acoustic resonators directly into the ChamberCore wall itself. The acoustic resonators fabricated by the wall-chambers of the ChamberCore structure are referred as "long chamber-based T-shaped acoustic resonators." The theories and results developed in Section 6.1 and Section 6.2 will be used here. The preliminary objective of this study is also to obtain a 3 dB NRS improvement in the first four targeted cavity resonances: 228 Hz, 398 Hz, 452 Hz, and 458 Hz using the long chamber-based T-shaped acoustic resonators.

6.3.1   Design and Construction of the Chamber-Based Acoustic Resonators

The chamber-based T-shaped acoustic resonators used in this study named as the following. The resonator for controlling the cavity mode (011) at 228 Hz is referred to as "CH228;" the resonator for controlling the cavity mode (010) at 398 Hz is referred to as "CH398;" the resonator for controlling the cavity mode (020) at 452 Hz is referred to as "CH452;" and the resonator for controlling the cavity mode (011) at 458 Hz is referred to as "CH458." The CH228 was designed with the condition $i=1$ (see Eq. (6.37)), and other resonators were designed with the condition $i=2$. Branch 2 and Branch 3 were constructed by chambers whose cross-sectional shape is trapezoidal, and Branch 1 was made from a circular cross-sectional PVC tube. Two CH228 resonators, two CH398 resonators, one CH452 resonator, and one CH458 resonator were designed. Only one CH452 and CH458 were designed since multiple acoustic resonators did not provide significantly better control. The optimal positions of the resonators were based on the investigation results of Section 6.1 and 6.2 (see Table 6.4) and were given in Table 6.9. The geometric dimensions of the acoustic resonators are given in Table 6.10.

Table 6.9 Position of Each Long Chamber-Based T-Shaped Acoustic Resonators

Acoustic resonator	Position coordinates		
	r(mm)	q (Degree)	z (mm)
CH228-Top	245	300	100.0
CH228-Bottom	245	315	710.0
CH398-Top	245	30	100.0
CH398-Bottom	245	15	713.5
CH452-Top	245	210	100.0
CH458-Bottom	245	195	710.0

Table 6.10 Geometric Dimensions of Designed Chamber-Based Acoustic Resonators

Group		CH228		CH398		CH452	CH458
		-Top	-Bottom	-Top	-Bottom	-Top	-Bottom
Branch 1	Radius: a (mm)	13.2	13.2	13.2	13.2	13.2	13.2
	Area: S_1 (mm^2)	547.4	547.4	547.4	547.4	547.4	547.4
	Length: L_{B1_1} (mm)	10.0	10.0	10.0	11.0	10.0	10.0
Branch 2	Area: S_2 (mm^2)	1370.0	1440.0	1410.0	1350.0	1390.0	1400.0
	Length: L_{B2} (mm)	86.8	26.8	86.8	121.8	86.8	26.8
Branch 3	Area: S_3 (mm^2)	1370.0	1440.0	1410.0	1350.0	1390.0	1400.0
	Length: L_{B3} (mm)	326.7	326.1	594.0	584.4	513.3	512.2

The chamber-based, T-shaped acoustic resonators were constructed from the chambers of the ChamberCore cylindrical fairing, a circular cross-sectional PVC tubes that forms Branch 1, and "hard" closed-foam. The closed-foam was used to close the two ends of the chambers to form Branch 2 and Branch 3. The drawbacks of using closed-foam is that the closed ends of Branch 2 and Branch 3 cannot reflect sound waves well because the foam surface is raw and the stiffness of the "hard" closed-foam is much smaller than that of PVC materials. Therefore, the designed resonators have pretty large errors with the ideal ones. The advantage of using the closed-foam is that the "closed end" formed by "hard" close-foam can be moved along the chambers. Therefore, the resonators can be easily tuned through adjusting the position of the "closed end" to change the length of Branch 2 or Branch 3. The long chamber-based T-shaped acoustic resonators are shown in Figure 6.22. The measured resonant frequencies of the tuned resonators are given in Table 6.11, and the resonant frequencies of the resonators are also listed in the table. The errors are given in the last column in the table as well.
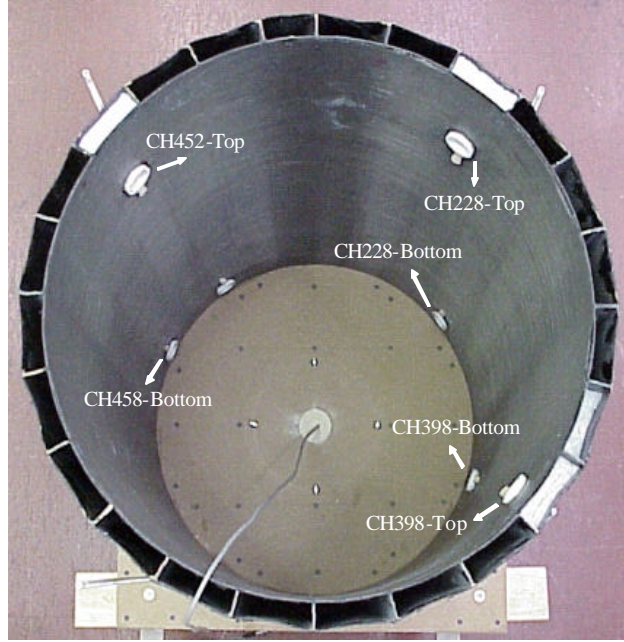
Figure 6.22 Layout of the Long Chamber-Based T-Shaped Acoustic Resonators

Table 6.11 Measured Frequencies of Tuned Chamber-Based Acoustic Resonators

Group		Measured (Hz)	Designed (Hz)	Error (%)
CH228	-Top	228.4	228.0	0.18
		584.4	598.6	2.43
		-	742.8	-
	-Bottom	227.5	228.0	0.22
		678.4	672.9	0.81
CH398	-Top	135.9	133.0	2.13
		400.3	398.0	0.57
		600.6	658.9	9.71
		-	906.1	-
	-Bottom	141.3	135.4	4.17
		398.4	398.0	0.10
		544.7	506.9	6.94
		758.4	693.6	8.54
		-	959.5	-
CH452	-Top	154.4	152.9	0.97
		452.9	452.0	0.20
		682.8	630.0	7.73
		-	795.7	-
CH458	-Bottom	152.8	153.2	0.26
		459.4	458.0	0.30
		760.3	754.4	0.78

6.3.2 Noise Transmission Control Using Tuned Chamber-Based Resonators

Three tests were designed to experimentally investigate the contribution of the long chamber-based T-shaped acoustic resonators to the noise transmission reduction in the Chamber-Core cylindrical firing [96]. The first test will not include any control resonators inside the cylinder. Rubber stoppers were inserted into the necks of Branch 1 to disable the acoustic resonators. The measured results will provide a basic reference for evaluating the effects of introducing the chamber-based resonators in the following tests.

The second subsequent tests were designed to individually investigate the noise transmission attenuation in each targeted frequency (228 Hz, 398 Hz, 452 Hz and 458 Hz). The CH228-Top and CH228-Bottom resonators were used to control the cavity mode (001) at 228 Hz. The NRS curve is shown in Figure 6.23. The measured maximum averaged NRS increase occurs at the plane z=120 mm, and the NRS curve is shown in Figure 6.24.
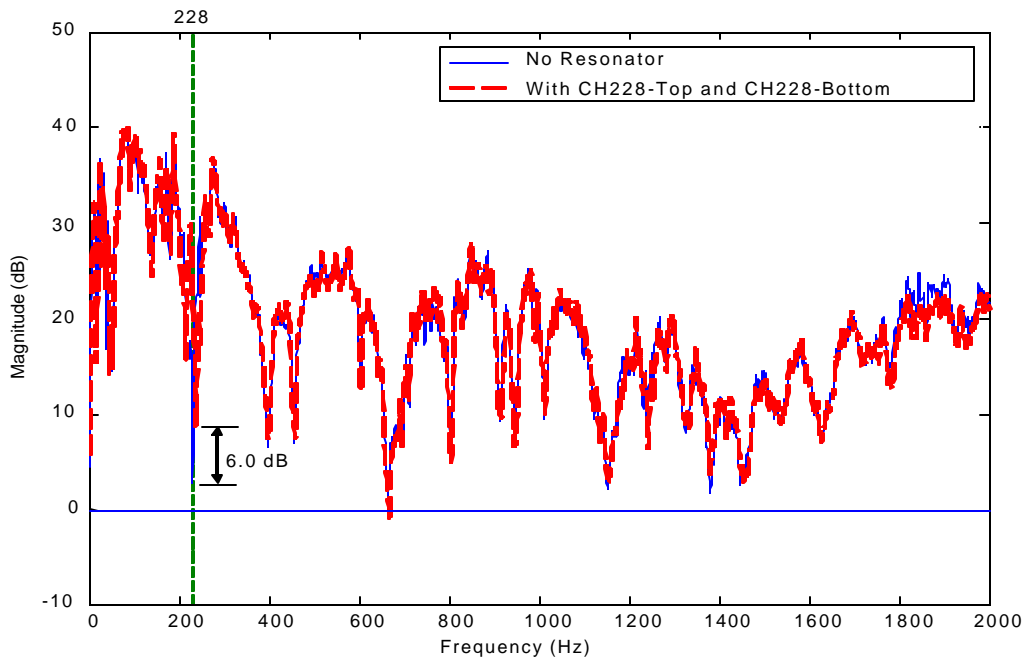
Figure 6.23 Noise Transmission Control Using CH228-Top and CH228-Bottom ARs (1)
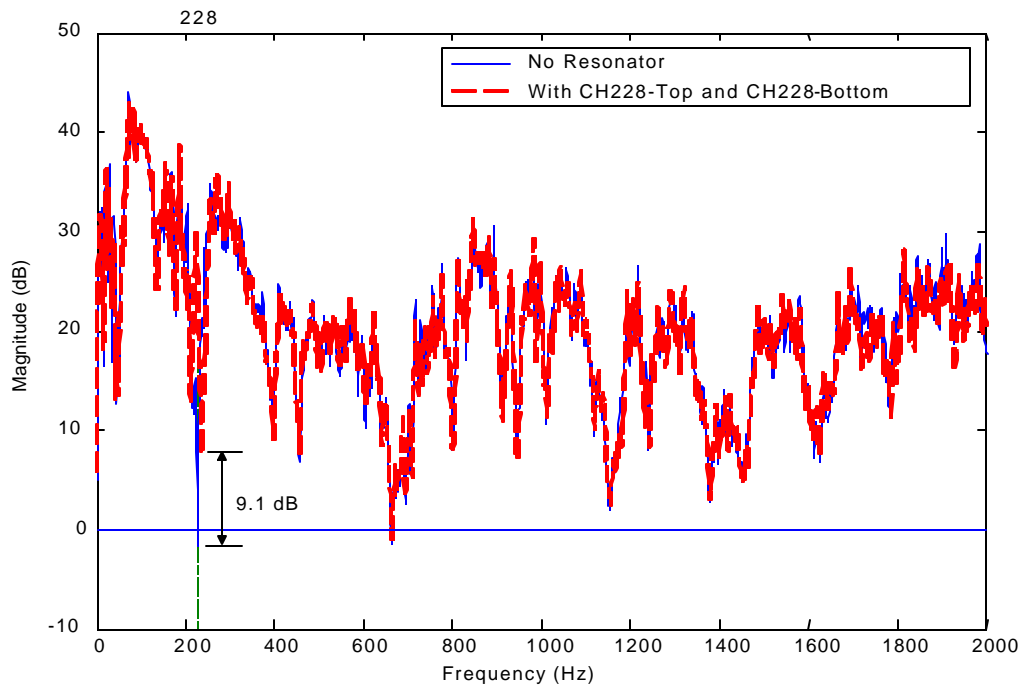
Figure 6.24 Noise Transmission Control Using CH228-Top and CH228-Bottom ARs (2)

In Figure 6.23 the NRS is reduced by 6.0 dB near 228 Hz. The measured maximum averaged NRS improvement around 228 Hz is 9.1 dB as shown in Figure 6.24.

The combination of CH398-Top and CH398-Bottom was used to control the cavity mode (010) at 398 Hz. The NRS curves are shown in Figure 6.25, and reflects a reduction of 4.3 dB around 398 Hz. It is also found that the noise around 228 Hz and 664 Hz is worsened by about 2 dB. The measured maximum averaged NRS increase around 398 Hz occurs at the plane of $z = 720$ mm, and the curve is shown Figure 6.26. The measured maximum averaged NRS increase is 8.1 dB at 398 Hz. Some worsening at high frequencies (>800 Hz) in z=720 mm plane (Figure 6.26), but as shown in Figure 6.25, the NRS cross the whole structure is unaffected at those frequencies.
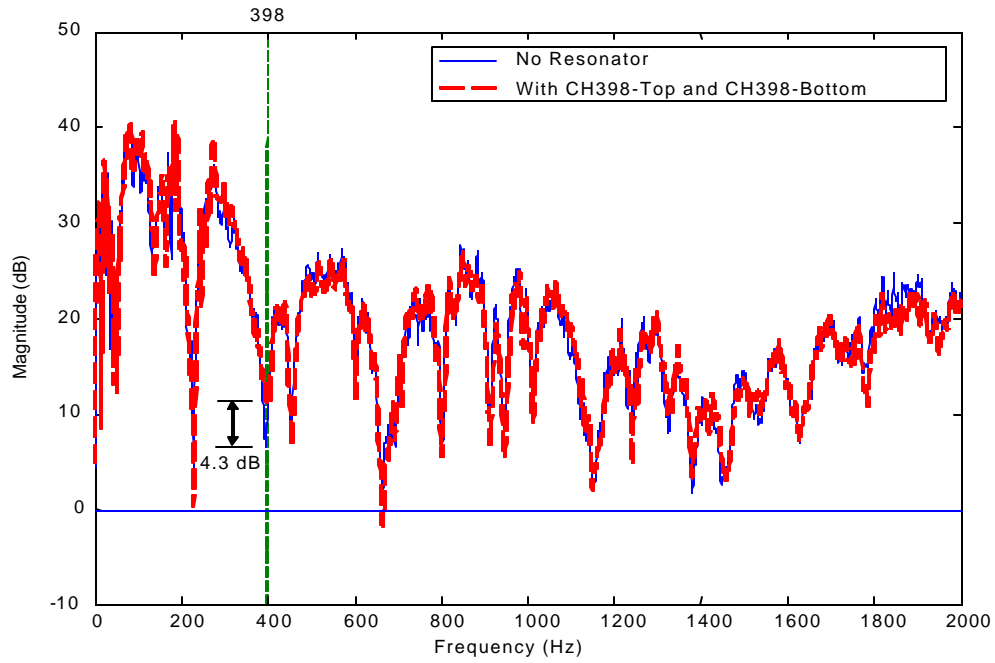
Figure 6.25 Noise Transmission Control Using CH398-Top and CH398-Bottom ARs (1)
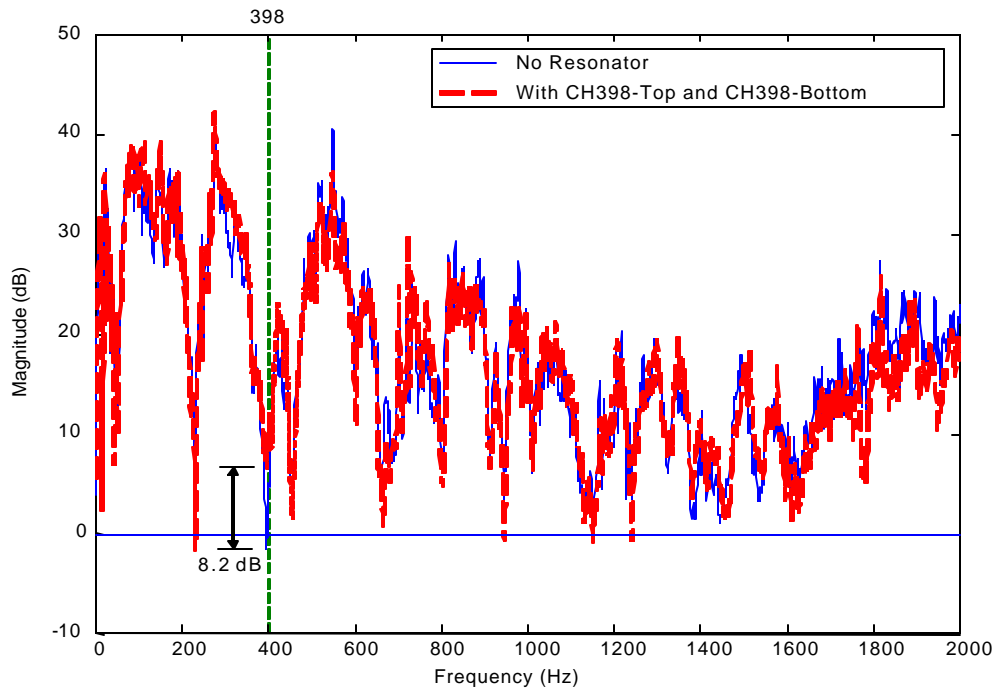
Figure 6.26 Noise Transmission Control Using CH398-Top and CH398-Bottom ARs (2)

138

In order to control the cavity mode (002) at 452 Hz and (010) at 458, the resonators CH452-Top and CH458-Bottom were used. The NRS curves are shown in Figure 6.27. The improvement of NRS is 2.8 dB around 452 and 458 Hz companied by 2.2 dB improvement around 398 Hz. Worsened NRS is observed around 228 Hz and 664 Hz, again.
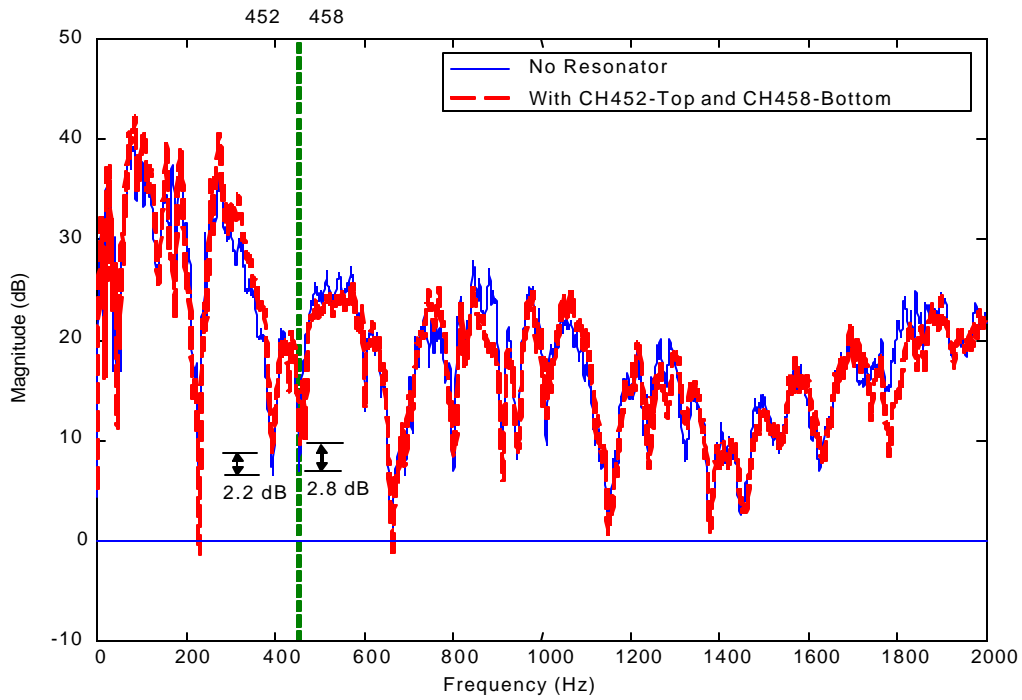
Figure 6.27 Noise Transmission Control Using CH452-Top and CH458-Bottom ARs (1)

The measured maximum averaged NRS improvement around 452 and 458 Hz occurs in the plane of $z = 720$ mm. The averaged NRS curve at this plane is shown in Figure 6.28, and the increase is 3.2 dB companied by 4.3 dB improvement around 398 Hz.
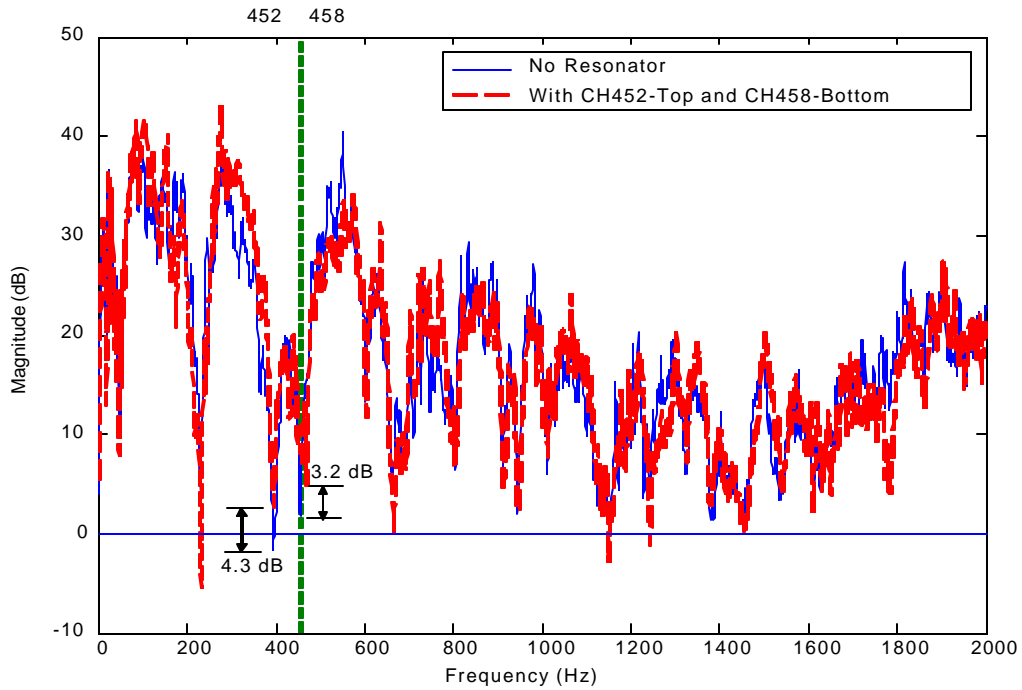
Figure 6.28 Noise Transmission Control Using CH452-Top and CH458-Bottom ARs (2)

The third test was designed to evaluate the noise transmission control at the four targeted cavity resonant frequencies using the combination of acoustic resonators CH228-Top, CH228-Bottom, CH398-Top, CH398-Bottom, CH452-Top, and CH458-Bottom. The position of the acoustic resonators in the cavity is given in Table 6.9. The measured NRS curves are shown in Figure 6.29, and the NRS curves averaged in specific planes are shown in Figure 6.30 and Figure 6.31.
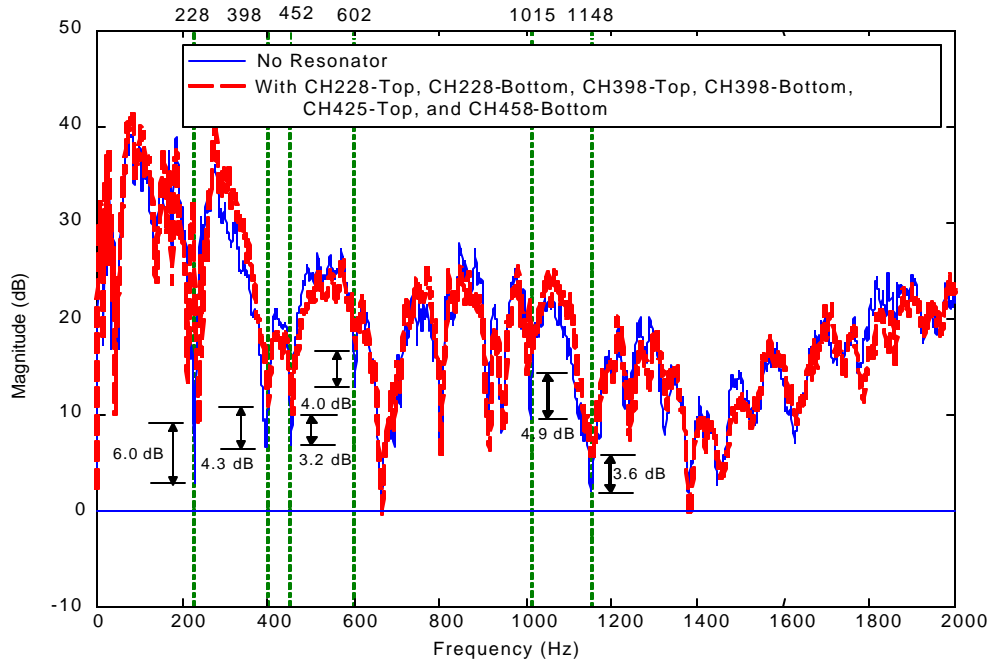
Figure 6.29 Noise Transmission Control Using Six Chamber-Based ARs (1)
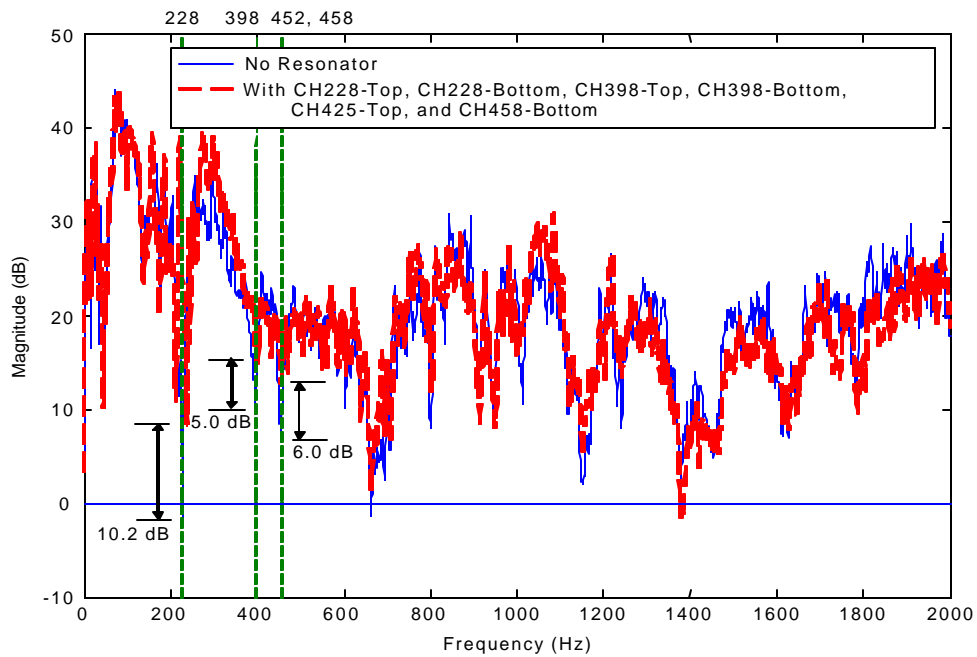
Figure 6.30 Noise Transmission Control Using Six Chamber-Based ARs (2)

141
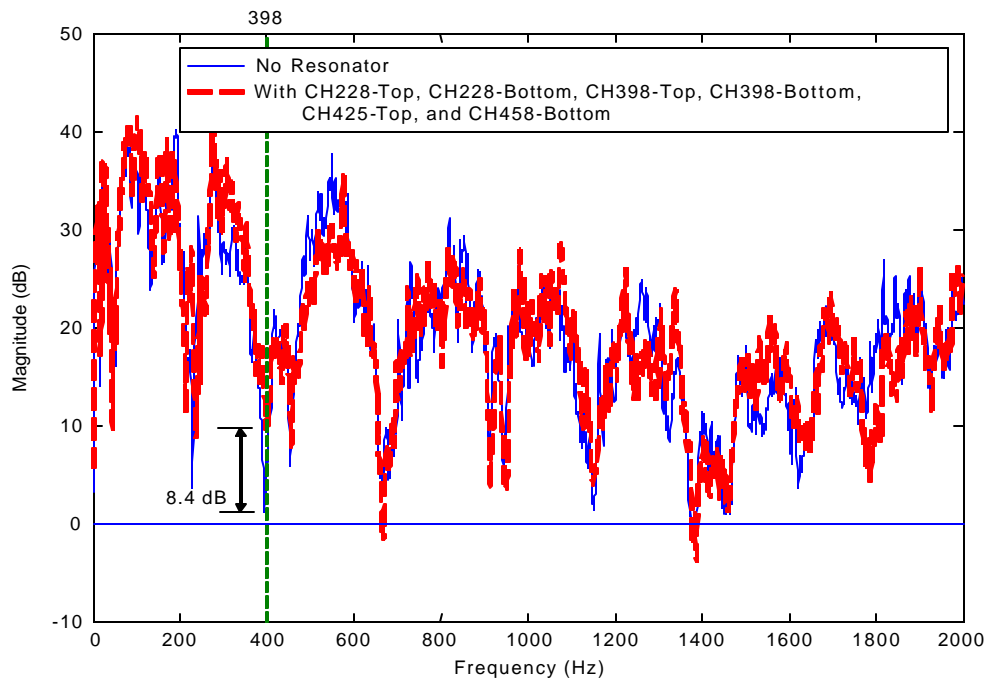
Figure 6.31 Noise Transmission Control Using Six Chamber-Based ARs (3)

Figure 6.29 is the NRS curves using six chamber-based acoustic resonators. From Figure 6.29 it can be observed that the four targeted cavity modes can be controlled very well with the combination of six chamber-based T-shaped acoustic resonators. The aim of obtaining 3 dB NRS improvement in each of the first four targeted frequencies is realized. The best improvement occurs around 228 Hz, and is 6.0 dB, and the minimum improvement occurs at 452 and 458 Hz, and is 3.2 dB. There is a 4.3 dB increase around 398 Hz. There is also significant improvement in the acoustic resonances 602 Hz, 1015 Hz, and 1148 Hz due to the coupling between structure and acoustics, and they are 4.0 dB, 4.9 dB, and 3.6 dB, respectively. There is a slight worsening of NRS at 1800 Hz, however, at 10 dB of NRS, this mode is not of large concern. The mode at 604 Hz provides significant noise transmission, however, only modes below 500 Hz where absorptive blankets are not effective, were considered here.

Figure 6.30 shows the measured maximum averaged NRS improvement for the targeted frequency 228 Hz, 452 Hz, and 458 Hz. It occurs at $z = 120$ mm with improvement of averaged NRS 10.2 dB around 228 Hz, and 6.0 dB around 452 and 458 Hz. The noise reduction is also

significant around 398 Hz in this plane, and is 5.0 dB. The maximum averaged NRS improvement for the frequency 398 Hz is 8.4 dB, and occurs in the plane of $z = 600$ mm, which can be found in Figure 6.31.

6.4   Conclusions

A more general and accurate model for cylindrical Helmholtz resonator design and natural frequency calculation has been developed. Cylindrical resonators were first designed and manufactured to control the first four acoustic cavity modes: (001) at 228 Hz, (010) at 398 Hz, (002) at 452 Hz and (011) at 458 Hz. A systematic test to investigate noise transmission control for the ChamberCore fairing using cylindrical Helmholtz resonators was demonstrated. The resonators were always placed at a pressure maximum for the particular modes being targeted. Results for implementing a combination of seven Helmholtz resonators (see Figure 6.9) show 5.8 dB and 7.7 db improvement at modes (001) and (010), respectively, and 2.0 dB of improvement at modes (002) and (011).

The effects on the noise reduction of the two closely spaced identical resonators have been investigated. The results show that control can be improved by about 1-3 dB around the target frequency (228 Hz) if the Helmholtz resonators are well-positioned. The optimal positioning of the two closed space resonators is 180 degrees apart. Also, the effects on the noise reduction of two closely spaced resonators at different- frequencies have been investigated by using HR228 and HR398. It is found that the control of the mode (010) at 398 Hz is not sensitive to the position change of the two different-frequency resonators except for the shift in modal frequency. For the control of mode (001) at 228 Hz, the same results have been observed as the same-frequency case above. The optimum relative spacing also was found to be 180 degrees apart.

A novel and general model for the calculation of resonant frequencies of the long T-shaped acoustic resonators has been developed. A new and general long T-shaped acoustic resonator design equation has been derived. Three new end correction models based on the

consideration of acoustics have been proposed and experimentally validated. End correction Model 3 gives excellent results for frequency prediction and resonator design. The new models proposed are no limitations for the cross-sectional shape of the three branches, and no limitations for the length of the three branches. Next, the noise transmission control for the ChamberCore fairing with well-positioned long T-shaped acoustic resonators was experimentally investigated. The results show that there is significant noise improvement over all frequency bands due to the contribution of the acoustic resonators with multi-modes. There are also significant resonance shifts found in the NRS curve mainly because of the volume change resulted from installing of the six long resonators.

Finally, six long T-shaped acoustic resonators were designed using the developed theories. The resonators were constructed from the chambers of the ChamberCore fairing, PVC tubes (to form Branch 1), and relatively stiff closed foam. The noise transmission control in the first four targeted cavity modes was experimentally investigated using the chamber-based, T-shaped acoustic resonators. The goal of 3 dB NRS increase is realized. The noise improvement is significant not only in the controlled modes but also in some non-targeted modes. Improvement ranging from 3.2 to 6.0 dB was observed in the noise reduction spectrum at the targeted inner cavity resonance frequencies.

7.0 CONCLUDING REMARKS

This work has focused on the goal of better characterization of the noise transmission into advanced composite cylindrical structures, which leads to better noise transmission controls. The task is by no means complete, but all the theoretical models and design schemes can be used for full size composite cylindrical structures for characterizing their noise transmission behavior and conducting noise transmission control.

7.1   Accomplishments

The pertinent accomplishments are summarized below.

- Developed a fully coupled mathematical model for analytically characterizing sound transmission into a finite elastic cylindrical structure with an application for the ChamberCore cylindrical composite fairing

- Developed a more general and accurate model for resonance frequency calculation and design of the cylindrical Helmholtz resonators

- Developed a novel and general model for resonance frequency prediction of the long, T-shaped, acoustic resonators

- Derived a novel equation for the long, T-shaped, multi-modal acoustic resonator design

- Developed an equivalent uniform shell model for the ChamberCore composite cylindrical structure

- Numerically/analytically calculated the structural and acoustic dynamic parameters for the AGS tapered fairing and the ChamberCore fairing

- Experimentally identified the structural and acoustic dynamic parameters for the AGS tapered fairing and the ChamberCore fairing

- Experimentally characterized the noise transmission behavior into the AGS tapered fairing

- Experimentally characterized the noise transmission behavior into the ChamberCore fairing

- Experimentally investigated the noise transmission control using passive fill materials for the ChamberCore fairing

- Experimentally investigated the noise transmission control using cylindrical Helmholtz resonators

- Experimentally investigated the noise transmission control using long T-shaped acoustic resonators

- Experimentally investigated the noise transmission control using long, chamber-based, T-shaped, acoustic resonators for the ChamberCore fairing.

7.2   Recommendations for Future Work

The analytical solution of the scattering and radiation pressure from a finite cylindrical shell should be studied. The radiation from two end caps should also be considered in the theoretical model of a real fairing system.

Improvements for obtaining more accurate structural and acoustic modal parameters should be investigated. The nonaxisymmetric source should be considered to excite the enclosed cavity to obtain better frequency responses over all modes. Improved experimental configuration should be considered when identifying the structural modal parameters, which will decrease the acoustic cavity effects on the structural modes

Smart acoustic resonators should be the next research topic. Our long T-shaped acoustic resonator does have a potential to be adaptive. The smart structure can be attached to one end of the resonator, and the smart acoustic resonator can be realized by means of adaptively changing

the acoustic radiation impedance of the smart structure. Multiple holes also can be opened along the resonator like a flute, and the smart acoustic resonator can also be realized through adaptively adjusting opening or closing status of the holes.

BIBLIOGRAPHY

1. Shen, F., and Pope, D., "Design and Development of Composite Fairing Structures for Space Launch Vehicles," McDonnell Douglas Space System Co., pp. 1447-1455.

2. Huybrechts, S. M., Hahn, S. E., and Meink, T. E., "Grid Stiffened Structures: A Survey of Fabrication, Analysis and Design Methods," Space Vehicles Directorate, Air Force Research Laboratory, and Boeing Space and Defense, The Boeing Company.

3. Huybrechts, S. M. and Tsai, S. W., "Analysis and Behavior of Grid Structures," Composite Science and Technology, Vol. 56, No. 9, January 1996, pp 1001-1015.

4. Huybrechts, S. M., and Meink, T. E., "Advanced Grid Stiffened Structures for the Next Generation of Launch Vehicles," Proceedings of Aerospace Conference, IEEE, Vol. 1, 1997, pp. 263 –270.

5. Meink, T. E., "Composite Grid vs. Composite Sandwich: A Comparison Based on Playload Shroud Requirements," Proceedings of Aerospace Conference, IEEE, Vol. 1, 1998, pp. 215 – 220.

6. Griffin, S. T., Denoyer, K. K., and Das, A., "Passive Vibration Isolation for Payload Containers," Journal of Intelligent Material Systems and Structures, Vol. 10, January 1999, pp. 83-87.

7. Hagood, N. W., and Crawley, E. F., "Experimental Investigation of Passive Enhancement of Damping for Space Structures," Journal of Guidance, Control, and Dynamics, Vol. 14, No. 6, Nov.-Dec. 1991, pp. 1100-1109.

8. Hughes, W. O., and McNelis, A. M., "Acoustic Testing of The CASSINI Spacecraft and TITAN IV Payload Fairing, Part 1- Introduction and Test Configuration," NASA TM-107474 (Lewis Research Center, Cleveland, Ohio, 1996).

9. Hughes, W. O., and McNelis, A. M., "Acoustic Testing of The CASSINI Spacecraft and TITAN IV Payload Fairing," Part 2- Results, NASA TM-107475 (Lewis Research Center, Cleveland, Ohio, 1996).

10. Bergen, T. F., and Kern, D. L., "Attenuation of the Cassini Spacecraft Acoustic Environment," Proceedings of the 1996 42nd Annual Technical Meeting of the Institute of Environmental Sciences, 1996, pp. 254-265.

11. Weissman, K., McNelis, M. E., and Pordan, W. D., "Implementation of Acoustic Blankets in Energy Analysis Methods with Application to the Atlas Payload Fairing," Journal of the IEST, July/August 1994, pp. 32-39.

12. Crane, R. M., and Santiago, A. L., "Modal Testing of Composite Cylinders," Dynamic Characterization of Advanced Materials, ASME 1993, NCA-Vol. 16/AMD-Vol. 172, pp. 41-49.

13. Olson, H. F., and May, E. G., "Electronic Sound Absorber," Journal of the Acoustic Society of America, Vol. 25, 1953, pp. 1130-1136.

14. Kido, K. "Reduction of Noise by use of Additional Sound Sources," Proceedings of Inter-Noise '75 (Sendai, Japan, 1975), pp. 647-650.

15. Chaplin G. B. B., and Smith, R. A., "Active Methods of Canceling Repetitive Vibrations," U.K. Patent No. 19717/76 (1976).

16. Houston, B., Marcus, M., Bucaro, J., and Wiliams, E. "Active Control of Payload Fairing Interior Noise Using Physics-Based Control Laws," 2nd AIAA/CEAS Aeroacoustics Conference, AIAA Paper 96-1723, May 6-8, 1996.

17. Widrow B. and Stears, S. D., Adaptive Signal Processing, Prentice Hall, 1985.

18. Fuller, C. R., Elliott, S. J., and Nelson, P. A., Active Control of Vibration, Academic Press, London, 1989.

19. Fuller, C. R., and von Flotow, A. H., "Active Control of Sound and Vibration", IEEE Control Systems Magazine, Vol. 15, Issue 6, Dec. 1995, pp. 9 –19.

20. Hansen, C. H. and Scott D. Snyder, S. D., Active Control of Noise and Vibration, E & FN Spon Press, 1997.

21. Hansen, C. H., Understanding Active Noise Cancellation, Spon Press, 2001.

22. Denenberg, J. N., "Anti-noise," IEEE Potentials, Vol. 11, Issue 2, April 1992 pp. 36 –40.

23. Leug, P., "Process of Silencing Sound Oscillations," U.S. Patent No. 2,043,416 (1936).

24. Griffin S. F., and Denoyer, K. K., "Experimental Sensor and Actuator Location Procedure for Control of Dynamically Complex Smart Structures," Proceedings of SPIE , Vol. 3329, pp. 717-723.

25. Denoyer, K. K., Griffin, S. F., and Sciulli, D., "Hybrid Structural/Acoustic Control of a Sub-Scale Payload Fairing," Proceedings of SPIE , Vol. 3329, pp. 237-243.

26. Griffin, S. F., Hansen, C. H., and Cazzolato, B., "Feasibility of Feedback Control of Transmitted Sound into a Launch Vehicle Fairing Using Structural Sensing and Proof Mass Actuator," AIAA-99-1529, pp. 2592-2600.

27. Griffin, S. F., Hansen, C. H., and Cazzolato, B., "Feedback Control of Structurally Radiated Sound into Enclosed Spaces Using Structural Sensing," Journal of the Acoustic Society of America, 106 (5), Nov. 1999, pp. 2621-2628.

28. Grosveld F. W., "Numerical Comparison Active Acoustic and Structural Noise Control in a Stiffened Double Wall Cylinder," AIAA/CEAS, Aeroacoustics Conference, AIAA Paper 96-1722 (AIAA Accession number 30835), 2nd, State College, PA, May 6-8, 1996.

29. Vipperman, J. S., Clark, R. L., "Multivariable Feedback Active Structural Acoustic Control Using Adaptive Piezoelectric Sensoriactuators," Journal of the Acoustic Society of America, 105 (1), Jan. 1999, pp. 219-225.

30. Elliott, S. J. and Gardonio, P. "Active Control of Sound Transmission", Internoise 2001, Aug. 2001.

31. Pelinescu, I., and Balachandran, B., "Analytical Study of Active Control of Wave Transmission through Cylindrical Struts," Smart Materials and Structures, Vol. 10, No. 1, Feb. 2001, pp. 121-136.

32. Herup, E., Huybrechts, S., Griffin, S., and Tsai, S., "Method of Making Composite ChamberCore Sandwich-Type Structure with Inherent Acoustic Attenuation," U.S. Patent No. 6,231,710 B1 (2001).

33. George, T. J., Herman Shen, M. -H., Huybrechts, S. M., Meink, T. E. "Optimal design of Composite ChamberCore Structures," Composite Structures, Vol. 52 No. 3-4, May/June 2001, pp. 277-286.

34. Vipperman, S. J., Li, D. Y., Avdeev, I., and Lane, S. A., "Characterization and Control of Sound Radiation in a Complex Fairing Structure," Internoise 2001, Hague, Netherlands, Aug. 2001, pp.2429-2435.

35. Vipperman, S. J., Li, D. Y., and Avdeev, I., "Investigation of The Transmission Loss Behavior of An Advanced Grid-Stiffened Structure," Proceedings of IMECE'01, ASME IMECE 2001, New York, Nov. 2001.

36. Koval, L. R., "On Sound Transmission into a Thin Cylindrical Shell under Flight Conditions," Journal of Sound and Vibration, Vol. 48, No. 2, 1976, pp. 265-275.

37. Manning, J. E., and Maidanik, G., "Radiation Properties of Cylindrical Shells," Journal of the Acoustical Society of America, Vol. 36, 1964, pp. 1691-1698.

38. White, P. H., "Sound Transmission through a Finite, Closed, Cylindrical Shell," Journal of the Acoustical Society of America, Vol. 40, No. 5, 1966, pp. 1124-1130.

39. Cheng, L. "Fluid-Structural Coupling of a Plate-Ended Cylindrical Shell: Vibration and Internal Sound Field," <u>Journal of Sound and Vibration</u>, Vol. 174, No. 5, 1994, pp. 641-654.

40. Tso, Y. K., and Hansen, C. H. "An Investigation of The Coupling Loss Factor for a Cylinder/Plate Structure," <u>Journal of Sound and Vibration</u>, Vol. 199, No. 4, 1997, pp. 629-643.

41. Koval, L. R., "Effects of Cavity Resonances on Sound Transmission into a Thin Cylindrical Shell," <u>Journal of Sound and Vibration</u>, Vol. 59, No. 1, 1978, pp. 23-33.

42. Tang, Y. Y., Robinson, J. H., and Silcox, R. J., "Sound Transmission through Two Concentric Cylindrical Sandwich Shells," <u>14th International Modal Analysis Conference</u>, Dearbon, Michigan, Feb. 1996.

43. Tang, Y. Y., Robinson, J. H., and Silcox, R. J., "Sound Transmission through a Cylindrical Sandwich Shell with Honeycomb Core."

44. Blake, W. K., <u>Mechanics of Flow-Induced Sound and Vibration, Volume 1, General Concepts and Elementary Sources</u> (Academic Press, London, 1986).

45. Fahy, F., <u>Sound and Structural Vibration: Radiation, Transmission and Response</u> (Academic Press, London, 1993).

46. Blackstock D. T., <u>Fundamentals of Physical Acoustics</u> (John Wiley & Sons, 2000).

47. Junger M. C., and Feit, D., <u>Sound, Structures, and Their Interaction</u> (2nd edition; MIT Press Cambridge, Massachusetts, London, 1986).

48. Blevins, R. D., <u>Formulations for Natural Frequency and Mode Shape</u> (Van Nostrand Reinhold company, 1979).

49. Beranek, L. L. <u>Acoustical Measurements</u> (Revised Edition; Published for the Acoustical Society of America by the America Institute of Physics, 1988, 1993).

50. Ho, B. L. and Kalman, R. E., "Effective Construction of Linear State-Variable Models from Input/Output Data," <u>Proceedings of the 3rd Annual Allerton Conference on Circuit and System Theory</u>, 1965, pp. 449-459.

51. Zeiger, H. P. and McEwen, A. J., "Approximate Linear Realization of Given Dimension Via Ho's Algorithm," <u>IEEE Transactions on Automatic Control</u>, Vol. AC-19, No. 2, April 1974, pp.153.

52. Kung S., "A New Identification and Model Reduction Algorithm via Singular Value Decomposition," <u>The 12th Asilomar Conference on Circuits, System and Computer</u>, Nov. 1978, pp. 705-714.

53. Juang, J. N., and Pappa, R. S., "An Eigensystem Realization Algorithm (ERA) for Model Parameter Identification and Model Reduction," <u>Journal of Guidance, Control, and Dynamics</u>, Vol. 8, No. 5, Sept.-Oct. 1985, pp. 620-627.

54. Juang, J. N., Cooper, J. E., and Wright, J. R., "An Eigensystem Realization Algorithm Using Data Correlations (ERA/DC) for Modal Parameter Identification," <u>Control Theory and Advanced Technology</u>, Vol. 4, No. 1, 1988, pp. 5-14.

55. Akaike, H., "Markovian Representation of Stochastic Processes by Canonical Variables," <u>SIAM Journal on Control</u>, Vol. 13, 1975, pp.162-173.

56. Baram, Y., "Realization and Reduction of Markovian Models from Non-stationary Data," <u>IEEE Transactions on Automatic Control</u>, Vol. 26, Issue: 6, 1981, pp. 1225-1231.

57. Larimore, W. E., "Canonical Variate Analysis for Identification, Filtering, and Adaptive Control," <u>Proceedings of the 29th IEEE Conference on Decision and Control</u>, Vol. 2, 1990, pp. 596-604.

58. Mullis, C. T., and Roberts, R. A., "The Use of Second-Order Information in the Approximation of Discrete-Time Linear System," <u>IEEE Transactions on Acoustics, Speech and Signal Processing</u>, Vol. 24, No. 3, 1976, pp. 226-238.

59. Inouye, Y., "Approximation of Multivariable Linear Systems with Impulse Response and Autocorrelation Sequences," <u>Automatica</u>, Vol. 19, No. 3, 1983, pp. 265-277.

60. King, A. M., Desai, U. B., and Skelton, R. E., "A Generalized Approach to q-Markov Covariance Equivalent Realization of Discrete Systems," <u>Automatica</u>, Vol. 24, No. 4, 1988, pp.507-515.

61. Liu, K., "Identification of Multi-Input and Multi-Output Systems by Observability Range Space Extraction," <u>Proceedings of the 31st IEEE Conference on Decision and Control</u>, Dec. 1992, pp. 915-919.

62. Liu, K., Jacques, R. N., and Miller, D. W., "Frequency Domain Structural System Identification by Observability Range Space Extraction," <u>Proceedings of America Control Conference</u>, June 1994, pp. 107-111.

63. Jacques, Robert. N., <u>On-line System Identification and Control Design for Flexible Structures</u> (unpublished Ph.D. Dissertation, School of Aeronautics an Astromautics, MIT, 1994).

64. Ibrahim, S. R., and Mikulcick, E. C., "A Method for the Direct Identification of Vibration Parameters from Free Response," <u>Shock and Vibration Bulletin</u>, No. 47, Sept. 1977, pp. 183-198.

65. Chen, C. T., "Evaluation of Modal Testing Methods," <u>AIAA</u> Paper 84-1071, May 1984.

66. Richardson, M. H., "Is It Mode Shape, or an Operating Deflection Shape?" <u>Sound & Vibration Magazine 30th Anniversary Issue</u>, March 1997, pp. 1-11.

67. Holmer, C. I., and Heymann, F. J., "Transmission of Sound through Pipe Walls in the Presence of Flow," <u>Journal of Sound and Vibration</u>, Vol. 70, No. 3, pp. 275-301.

68. J. P. Maillard and C. R. Fuller, C. R., "Advanced Time Domain Sensing for Structural Acoustic Systems," <u>Journal of the Acoustical Society of America</u>, Vol. 95, No. 6, 1994, pp. 3252-3272.

69. Clark, R. L., and Fuller, C. R., "Control of sound radiation with adaptive structures," <u>Journal of Intelligent Material Systems and Structures</u>, Vol. 2, No. 3, 1991, pp. 431-452.

70. Meirovitch L., and Thangjitham, S., "Active Control of Sound Radiation Pressure," <u>Journal of Vibration, Acoustics, Stress and Reliability in Design</u>, Vol. 112, No. 2, April 1990, pp. 237-244.

71. Banks, H. T., Silcox, R. J., and Smith, R. C., "Approximation Methods for Control of Structural Acoustics Models with Piezoceramic Actuators," <u>Journal of Intelligent Materials Systems and Structures</u>, Vol. 4, January 1993, pp. 98-116.

72. MacMartin, D. G., "Collocated Structural Control for Reduction of Aircraft Cabinnoise," <u>Journal of Sound and Vibration</u>, Vol. 190, No. 1, 1996, pp. 105-119.

73. Vipperman, Jeffrey Stuart, <u>Adaptive Piezoelectric Sensoriactuators for Active Structural Acoustic Control</u> (unpublished Ph.D. Dissertation, School of Mechanical Engineering, Duke University, 1997).

74. Zhang, S. Y., Liu, J. Q., Yu, X. X., Cai, L. W., <u>Mechanical Properties of Composite Structures</u> (Beijing Institute of Technology Press, 1992).

75. Huang, Y. M., Fuller, C. R., "The Effects of Dynamic Absorbers on The Forced Vibration of a Cylindrical Shell and Its Coupled Interior Sound Field," <u>Journal of Sound and Vibration</u>, Vol. 200, No. 4, 1997, pp. 401-418.

76. Thomas, D. R., Nelson, P. A., Elliot, S. J., "Active Control of the Transmission of Sound Through a Thin Cylindrical Shell, Part II: The Minimization of Acoustic Potential Energy," <u>Journal of Sound and Vibration</u>, Vol. 167, No. 1, 1993, pp. 113-128.

77. Li, D., and Vipperman, J. S., 2002, "Noise Transmission Control Studies on a Chamber Core Composite Cylinder," <u>ASME IMECE 2002</u>, Paper IMECE02-33069, New Orleans, LA, Nov. 2002.

78. Li, D., and Vipperman, J. S., 2002, "Investigation of the Sound Transmission Behavior of a Chamber Core Cylinder," <u>143rd Meeting of ASA</u>, Pittsburgh, PA, Jun. 2002.

79. Vipperman, J. S., Li, D., Avdeev, I., Lane, S. A., 2003, "Investigation of the Sound Transmission into an Advanced Grid-Stiffened Structure," Journal of Vibration and Acoustics, Vol. 125, pp. 257-266.

80. Bradford, L., Manning J. E., 1996 "Attenuation of the Cassini Spacecraft Acoustic Environment," Sound and Vibration, October 1996, pp. 30-35.

81. Kuntz, H. L., Prydz, R. A., Balena, F. J., Gatineau, R. J., 1991, "Development and Testing of Cabin Sidewall Acoustic Resonators for the Reduction of Cabin Tone Levels in Propfan-Powered Aircraft," Journal of Noise Control Engineering, Vol. 37, No. 3, pp. 129-142.

82. Giampaoli, E., Gerges, S. N. Y., 1989, "Low Frequency Sound Absorption by Cavity Resonator Masonry Blocks," Journal of Noise Control Engineering, Vol. 33, No. 3, pp. 131-138.

83. Bedout, J. M., Franchek, M. A., Bernhard, R. J., Mongeau, L., 1997, "Adaptive-Passive Noise Control with Self-Tunning Helmholtz Resonators," Journal of Sound and Vibration, Vol. 202, No. 1, pp. 109-123.

84. Horowitz, S., Nishida, T., Cattafesta, L., Sheplak, M., 2002, "Characterization of Compliant-Backplate Helmholtz Resonators for an Electromechanical Acoustic Liner," 40th Aerospace Sciences Meeting & Exhibit, Paper AIAA2002-0666.

85. Rayleigh, L. 1945, The Theory of Sound, New York, Dover.

86. Ingard, U., 1953, "On the Theory and Design of Acoustic Resonators," The Journal of the Acoustical Society of America, Vol. 25, No. 6, pp. 1037-1061.

87. Alster, M., 1972, "Improved Calculation of Resonant Frequencies of Helmholtz Resonators," Journal of Sound and Vibration, Vol. 24, No. 1, pp 63-85.

88. Panton, R. L., and Miller, J. M., 1975, "Resonant Frequencies of Cylindrical Helmholtz Resonators," The Journal of the Acoustical Society of America, Vol. 57, No. 6, pp. 1533-1535.

89. Merkli, P., 1978, "Acoustic Resonance Frequencies for a T-Tube," Journal of Applied Mathematics and Physics (ZAMP), Vol. 29, pp. 486-498.

90. Kinsler, L. E., and Frey, A. R., 1962, Fundamentals of Acoustics, John Wiley & Sons, New York.

91. Soh, Y. P., Yap, E. W. T., Gan, B. H. L., "Industrial Resonator Muffler Design," http://www.mecheng.adelaide.edu.au/Courses/Projects/level4papers2001/soh_yap_gan.pdf.

92. N. M. McLachlan, 1955, Bessel Function for Engineer, Oxford University Press, Second Edition.

93. Li, D. and Vipperman, J. S., "Helmohltz Resonator Design for Noise Transmission Attenuation into a Chamber Core Composite Cylinder," 144th Meeting of the Acoustical Society of America, 3rd Iberoamerican Congress of Acoustics, 9th Mexican Congress on Acoustics, Cancun, Mexico, Dec. 2002.

94. Li, D. and Vipperman, J. S., "Noise Control of A Chamber Core Cylinder Using Cylindrical Helmholtz Resonaotr," ASME IMECE 2003, Paper IMECE03-41978, Washington, D.C. Nov. 2003.

95. Li, D. and Vipperman, J. S., "Design and Resonant Frequency Prediction for Long T-Shaped Acoustic Resonators," 146th Meeting of ASA, Austin, Texas, Nov. 2003.

96. Li, D. and Vipperman, J. S., "Noise Control for a Chamber Core Composite Structure Using Long T-Shaped Acoustic Resonators," 146th Meeting of ASA, Austin, Texas, Nov. 2003.